

Determination of the beam asymmetry Σ in η - and η' -photoproduction using Bayesian statistics

JAKOB MICHAEL KRAUSE

Masterarbeit in Physik

angefertigt im Helmholtz-Institut für Strahlen- und
Kernphysik

vorgelegt der

Mathematisch-Naturwissenschaftlichen Fakultät
der
Rheinischen Friedrich-Wilhelms-Universität
Bonn

Sep 2022

DRAFT

I hereby declare that this thesis was formulated by myself and that no sources or tools other than those cited were used.

Bonn,
Date
Signature

1. Gutachterin: JUN. PROF. DR. ANNIKA THIEL
2. Gutachter: PROF. DR. JOCHEN DINGFELDER

Acknowledgements

First of all I would like to thank ANNIKA THIEL for giving me the opportunity of being part of her research group since the beginning of my bachelor thesis in 2020. Now, with the formulation of this thesis, I will be finishing my academic career in Bonn. I greatly appreciate the insight into research I could gain.

I express my thanks to JOCHEN DINGFELDER who agreed to be the second referee for this thesis.

This thesis could not have been written without the help of FARAH AFZAL. After all, it was you, who got me into the boat again after my bachelor thesis. Over the past year we have shared our office and many fruitful discussions regarding physics (or not) were had. I am thankful that you and your masters and PhD thesis provided such excellent foundation for me to rely my work on.

Being the pioneer of the working group BECK/THIEL in all things regarding BAYESIAN statistics, PHILIPP KRÖNERT contributed the idea of what shall fill about half of this thesis and furthermore his help and guidance whenever i got stuck on the way. I am grateful that we were able to turn the thesis into this direction with your help.

Also, I express my gratitude to everybody who was included in the process of data taking, i.e. the CBELSA/TAPS collaboration and crew. No analysis could have been performed without the data.

I thank FARAH AFZAL, PHILIPP KRÖNERT, DOMINIC SCHÜCHTER and NIKOLAS PÄSSLER for reading my thesis and providing me with useful comments and insights.

Finally, I thank my parents, for the support throughout my whole studies, which now then officially come to an end.

DRAFT

Contents

1	Introduction	1
1.1	Photoproduction of Pseudoscalar Mesons	4
1.2	Measurement of Polarization Observables	5
1.3	Introduction to BAYESIAN statistics	5
1.3.1	Frequentist Approach	5
1.3.2	Bayesian approach	5
1.3.3	Combining inferences	5
1.4	Motivation and Structure of this Thesis	5
2	Experimental Setup	7
2.1	Production of (polarized) high energy photon beam	7
2.1.1	Tagger	8
2.2	Beam Target	8
2.3	Calorimeters	8
2.4	Trigger	8
3	Event selection	11
3.1	Preselection and charge cut	11
3.2	Time of particles	12
3.3	Kinematic constraints	14
3.3.1	Derivation of cut conditions	14
3.3.2	Determination of cut ranges	15
3.3.3	Quality of event selection	21
3.4	Investigation of background and additional cuts	22
3.4.1	Inspecting plausibility of background reactions	22
3.4.2	Misidentification of background reactions	25
3.4.3	Examination of additional cuts	28
3.5	Summary of event selection	31
4	Extraction of the beam asymmetries Σ_η and $\Sigma_{\eta'}$	33
4.1	Methods	34
4.1.1	Event yield asymmetries	34
4.1.2	Event based fit	37
4.2	Determination of Σ_η using Bayesian statistics	39
4.2.1	Application of methods to toy Monte Carlo data	40
4.2.2	Application of methods to data	48

4.2.3	Discussion	51
4.3	Determination of $\Sigma_{\eta'}$	55
4.3.1	Application of event based fit to toy Monte Carlo data	55
4.3.2	Application of event based fit to data	60
5	Summary and outlook	63
A	Additional calculations	65
A.1	Statistical error for the asymmetry $A(\phi)$	65
B	Discussion of binned fits	67
C	Investigation of truncated posteriors	69
Bibliography		71
List of Figures		75
List of Tables		79

DRAFT

CHAPTER 1

Introduction

The *Standard Model of Particle Physics* (SM) is the most successful model aiming to describe the particles and forces of the universe. It distinguishes between *fermions* and *bosons*. While all matter consists of fermions, bosons are particles that mediate the fundamental interactions.

Matter consists of (anti-)quarks and (anti-)leptons with three generations of each. Table 1.1 shows all elementary fermions including some of their most important properties. Only the first and lightest generation consists of stable particles, i.e. the up and down quark as well as the electron and its neutrino. All other particles are heavier and not stable, they will thus decay fast via the strong, electromagnetic or weak interaction.

There are in fact four interactions described by the SM: strong, electromagnetic, weak and gravitational interaction¹, where gravitation is mentioned here for the sake of completeness; on the mass scale of elementary particles gravitation is negligible. Strong and weak interaction are restricted to a finite range of the order of the nucleon radius, whereas electromagnetic interaction and gravitation have infinite range. Each interaction has its own coupling (charge). The strong interaction is mediated by gluons and couples to the color charge.

	Generation			el. charge	color charge
	1	2	3		
Quarks	u	c	t	2/3	r,g,b
	d	s	b	1/3	r,g,b
Leptons	e	μ	τ	-1	-
	ν_e	ν_μ	ν_τ	0	-

Table 1.1: Summary of the particles of the SM

Gluons and quarks carry color charge and thus interact strongly. However, an isolated quark or gluon has not been observed. Only color neutral bound systems of quarks are seen, which are called hadrons. Hadrons with integer spin are called mesons and those with half-integer spin are called baryons. Color neutrality demands mesons consist of at least one quark and one anti-quark and baryons consist of at least three quarks.

¹ they are ordered here according to their relative strength

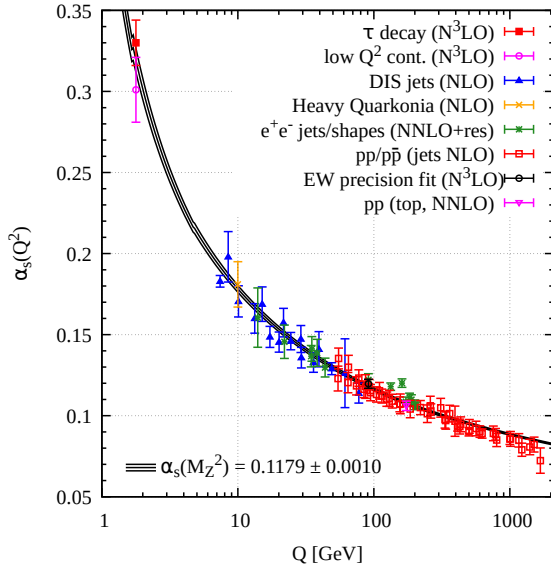


Figure 1.1: Running coupling of QCD. The colored data points represent different methods to obtain a value for α_s . For more details it may be referred to [Zyl+20].

As already mentioned, isolated quarks are not seen. This can be understood in terms of the strong coupling constant α_s . The coupling constant is a measure of the strength of the strong interaction. Because it is highly dependent on the momentum transfer in the observed strong reaction it is also called running coupling constant, which is depicted in figure 1.1.

For low (< 1 GeV) momentum transfers or large distances the coupling constant approaches infinity whereas it decreases for high ($\gg 1$ GeV) momentum transfers or short distances. These momentum ranges are referred to as *confinement* and *asymptotic freedom*, respectively; quarks are confined to remain in a bound state since if one tried to pull them apart the color field becomes so strong it will create a new quark anti-quark pair resulting in two new bound states. On the other hand, bound quarks behave quasi-free and can be described using perturbative quantum chromodynamics (pQCD) if probed at sufficiently large momentum transfers.

It is more difficult however to describe QCD at momentum scales of ≈ 1 GeV since the coupling is too strong to justify a perturbative approach. Thus explicit modeling of QCD bound states is inevitable. One possibility is to describe baryons consisting of constituent quarks which are bound in a potential. Constituent quark models assume baryons are made up of three constituent quarks with effective masses differing from the bare quark mass. The effective mass is made up mostly from a sea of quark anti-quark pairs and gluons which surround the bare (valence) quarks. The explicit form of the binding potential is determined for each model.

The Bonn model [LMP01], for example, is formulated as a relativistically covariant constituent quark model. A potential increasing linearly with the distance is employed to adequately describe confinement. The binding potential between the constituent quarks is described by an instanton-induced interaction. Baryon resonances are then states with an orbital or angular excitation of one of the quarks. Figure 1.2 shows computed nucleon, that is Isospin $I = 1/2$ resonances, of the Bonn model [LMP01] on the left side of each column. These are compared to measured resonances and their PDG rating [Zyl+20] in the middle. Uncertainties are indicated by the colored areas. The resonances are

identified by their total angular momentum and their parity $J\pi$. In addition also the total internal angular momentum along with isospin and again the total angular momentum L_{2T2J} is given. While

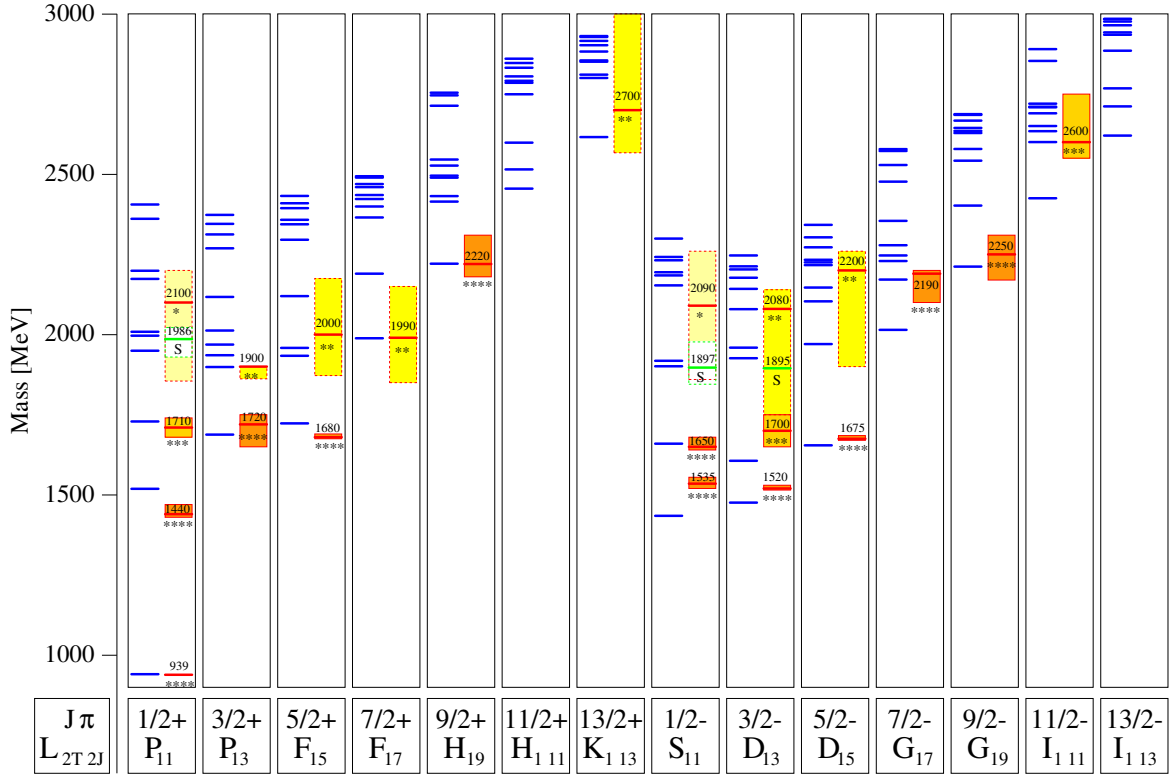


Figure 1.2: Calculated nucleon (isospin $I = 1/2$) resonances compared to measurements. Left in each column are the calculations [LMP01], the middle shows the measurements and PDG rating [Zyl+20]

generally good agreement exists for low lying resonances, especially for high masses there are much more resonances predicted than actually found. This is also known as the problem of the “missing resonances” indicating the poor understanding of QCD in the non-perturbative region. This can be due to several reasons: most of the knowledge about nucleon resonances and their properties was obtained investigating the πN channel, biasing the data for resonances coupling weakly to this channel. Furthermore, the number of excited states with definite quantum numbers is related directly to the effective number of degrees-of-freedom accessible to the underlying theory. As a consequence, the number of degrees-of-freedom should be obtainable by comparing the measured states to the predicted states. Since nucleon resonances decay dominantly hadronic, their resonances are broad and overlapping. Thus on one hand the determination of excitation spectra proves to be a challenge on its own, demanding sophisticated methods, such as partial wave analysis (PWA). On the other hand it is not yet clear how many effective degrees-of-freedom exist for the nucleon in a constituent quark model. They could for example be decreased if the nucleon were made up of a quark and a di-quark structure. In either case it should prove fruitful to investigate the photoproduction of mesons off the nucleon for different final states to access the resonances and transitions between them which are of interest. This should ultimately add to the understanding of QCD in the non-perturbative regime. [KS03]

1.1 Photoproduction of Pseudoscalar Mesons

From the scattering theory point of view, photoproduction of mesons is well understood [KS03]. Figure 1.3 shows schematically the process thereof off the proton:

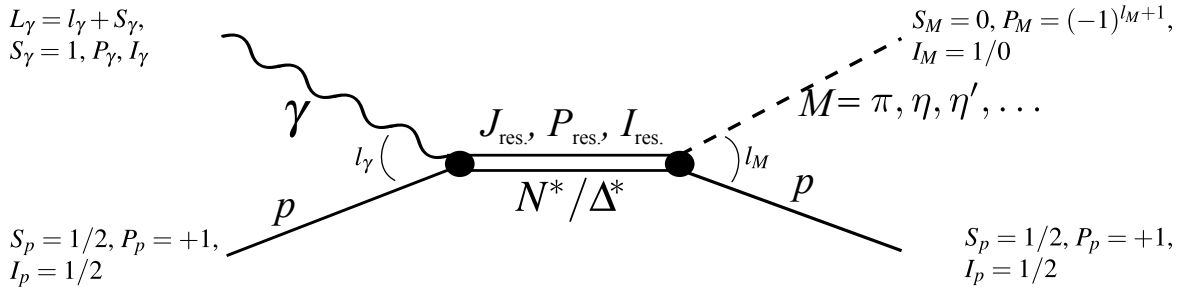


Figure 1.3: FEYNMAN diagram for the s-channel photoproduction of pseudoscalar mesons, adapted from [Afz19]

The analysis requires partial wave decomposition in both initial and final states [DT92] since the intermediate resonance has definite angular momentum, parity and isospin $J_{\text{res.}}, P_{\text{res.}}, I_{\text{res.}}$. The resonance is excited by a photon with (iso-) spin $I_\gamma, S_\gamma = 1$ and parity P_γ coupling electromagnetically to the target proton with (iso-) spin $I_p = 1/2, S_p = 1/2$ and parity P_p . The relative momentum is l_γ , such that the total momentum of the photon is $L_\gamma = l_\gamma + S_\gamma$. Subsequently the intermediate state will have the quantum numbers $J_{\text{res.}}, P_{\text{res.}}, I_{\text{res.}}$ and decay into a pseudoscalar ($S_M = 0$) meson with isospin I_M , relative orbital angular momentum l_M und Parity $P_M = (-1)^{l_M+1}$ and a proton. The following selection rules can be derived using parity and momentum conservation [KS03; Afz19]

$$J_{\text{res.}} = L_\gamma \oplus S_p = L_\gamma \oplus 1/2, \quad (1.1)$$

$$P_{\text{res.}} = P_p \cdot P_\gamma = P_\gamma, \quad (1.2)$$

$$J_{\text{res.}} = l_M \oplus S_p = l_M \oplus 1/2 \quad (1.3)$$

$$P_{\text{res.}} = P_p \cdot P_M = (-1)^{l_M+1}, \quad (1.4)$$

where the usual rules for the coupling of angular momenta [Bar+18] apply. Thus, knowledge of the photoproduction multipoles allows the identification of contributing resonances for particular mesonic final states. Table 1.2 shows relevant resonances for the lowest order of photon multipoles ($L_\gamma = 1$).

 E

Table 1.2: Allowed quantum numbers for the intermediate resonance state N^*/Δ^*

1.2 Measurement of Polarization Observables

1.3 Introduction to BAYESIAN statistics

1.3.1 Frequentist Approach

The traditional approach to this fitting problem is a χ^2 fit. Assume there are N precise predictors $\{x_i\}$ and corresponding measurements $\{y_i\}$ with measurement errors $\{\sigma_i\}$. Additionally, the data y is expected to follow a functional $y = f(x, \theta)$ with parameter(s) θ and predictors x . Then the test statistic

$$\chi^2 = \sum_{i=1}^N \left[\frac{y_i - f(x_i; \theta)}{\sigma_i^2} \right]^2 \quad (1.5)$$

can be minimized with respect to the parameters θ giving according estimates with error bars which are calculated using error propagation from the original data points $\{y_i\}$. The minimization can be solved analytically in the case of linear functions by solving the equation system

$$\frac{d}{d\theta} \chi^2 = 0$$

and otherwise numerically. The minimization of χ^2 to get best-fit estimates for the desired parameters can be motivated if one considers the likelihood \mathcal{L} that the data follow the function f . It is given by

$$\ln \mathcal{L} = -\frac{1}{2} \sum_{i=1}^N \left[\frac{y_i - f(x_i; \theta)}{\sigma_i} \right]^2 - \sum_{i=1}^N \ln \sigma_i \sqrt{2\pi}, \quad (1.6)$$

if one assumes GAUSSIAN errors at each data point. To maximize the (log-) likelihood with respect to all parameters is then equivalent to minimizing χ^2 . As a byproduct, the χ^2 fit also gives a goodness of fit estimate which is given by $\chi^2/\text{NDF} \approx 1$, where NDF are the number of degrees of freedom. Significantly smaller or larger values indicate too small error estimates or a bad fit, respectively. [Bar89]

1.3.2 Bayesian approach

As an alternative

1.3.3 Combining inferences

1.4 Motivation and Structure of this Thesis

bla

CHAPTER 2

Experimental Setup

As motivated in the previous chapter, it is promising to study the photoproduction of pseudoscalar mesons in order to determine a complete set of polarization observables. This requires a polarized photon beam and/or a polarized target. It is convenient to study photoproduction off a fixed target and investigate the resonances that occur in the process. Incidentally, these resonances can only be accessed via their decay products, such that suitable calorimeters are needed. The CBELSA/TAPS experiment is located in Bonn at the EElectron Stretcher Accelerator (ELSA), which can be used to generate a high energy photon beam using the *bremstrahlung* process, meets all above mentioned requirements. This chapter will elaborate on the already mentioned parts of the experiment that was used to collect the data needed for the determination of the target asymmetry in η' photoproduction.

2.1 Production of (polarized) high energy photon beam

First of all, a high energy photon beam has to be produced.

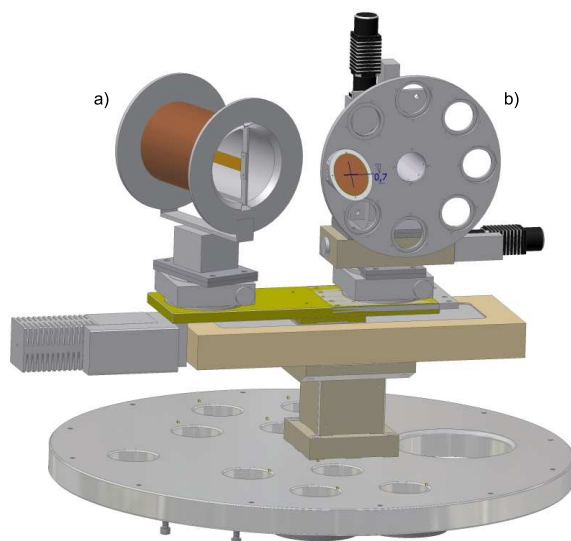


Figure 2.1: [Wal]

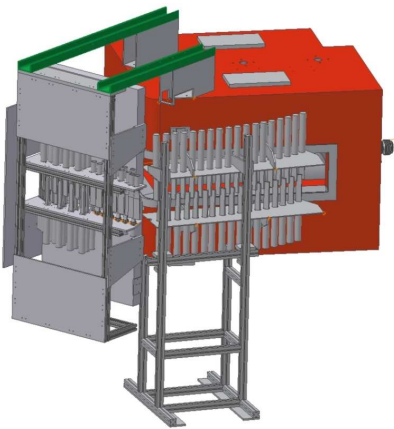


Figure 2.2: [Wal]

2.1.1 Tagger

2.2 Beam Target



Figure 2.3: [Wal]

2.3 Calorimeters

2.4 Trigger

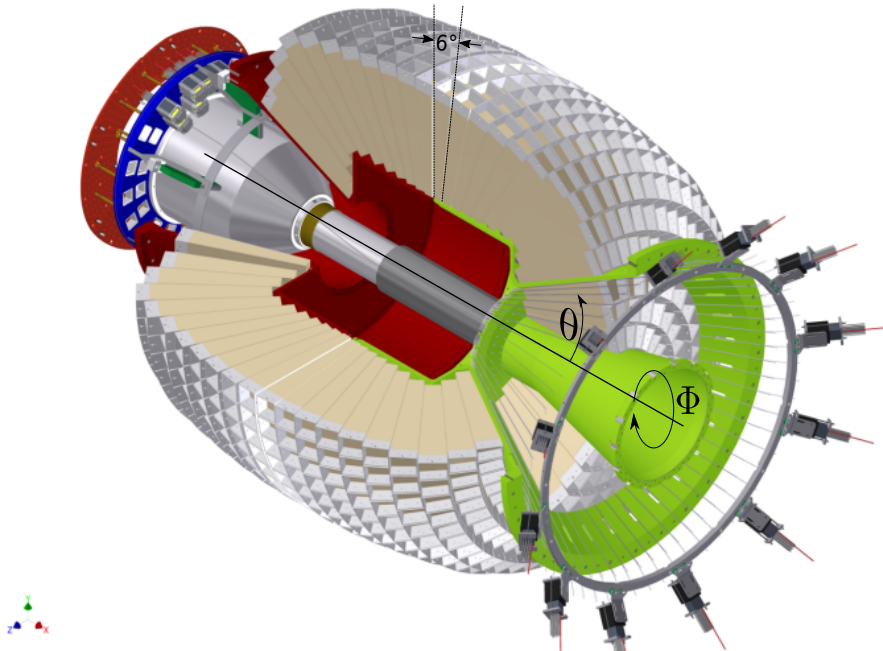


Figure 2.4: D. WALTHER in [Urb17]



Figure 2.5: [Wal]

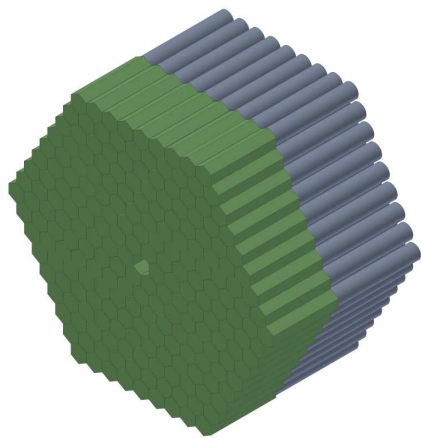


Figure 2.6: [Wal]

CHAPTER 3

Event selection

The determination of polarization observables needs to be completed for particular reactions (cf. chapter 1), such as the photoproduction of e.g. a single η' meson. However, the recorded events contain data from the decay products of all possible final states in addition to combinatorical background. Thus, event candidates for the desired reaction have to be extracted before they are considered for further analysis. Table 3.1 shows the five most probable decay modes of the η' meson. Three of these result in final states which only contain photons and are thus reliably measurable with the CBELSA/TAPS experiment. Only the $\eta' \rightarrow \gamma\gamma$ decay channel was considered for further analysis; the $\omega\gamma$ channel provides negligible statistics and considering the acceptance of detecting six photons in the final state, the expected yield of the $\eta' \rightarrow \gamma\gamma$ decays should be roughly equal to the $\eta' \rightarrow \pi^0\pi^0\eta \rightarrow 6\gamma$ final state [Afz22]. Offering a cleaner, three-particle final state, the $\eta' \rightarrow \gamma\gamma$ channel was then favored in the course of this thesis.

Decay mode		Branching ratio
$\pi^+\pi^-\eta$		42.6%
$\rho^0\gamma$	$\rightarrow \pi^+\pi^-\gamma$	28.9% (28.9%)
$\pi^0\pi^0\eta$	$\rightarrow 6\gamma$	22.8% (8.8%)
$\omega\gamma$	$\rightarrow \pi^+\pi^-\pi^0\gamma/\pi^0\gamma\gamma$	2.52% (2.2%/0.21%)
$\gamma\gamma$		2.3%

Table 3.1: The five most probable decay modes of the η' meson. The most probable further decay with according branching ratio is shown in brackets.[Zyl+20]

The process of *event selection* for the reaction $\gamma p \rightarrow p\eta' \rightarrow p\gamma\gamma$ is outlined in the following chapter. Note that in this thesis the analysis of data from η -photoproduction starts with this process already completed, which is described in detail in reference [Afz19].

3.1 Preselection and charge cut

Since the polarization degree can only be evaluated reliably up to 1 800 MeV and the production threshold for η' mesons is $E_\gamma = 1\,447$ MeV [Zyl+20], the beam photon energy range was restricted to 1 400 to 1 800 MeV from the very beginning. The measured events are then generally classified

depending on the number of particle energy deposits (PED). If the complete four-momenta of three final state particles are measured, they are referred to as 3PED events. Low energy protons however may either be only detected in the scintillators of the inner, forward or MiniTAPS detector – giving only directional information (2.5 PED) – or lost entirely (2 PED). Only 2.5PED and 3PED events were analyzed since the additional background contributions from 2PED events exceeded the additional signal contributions. It is worth noting that 3PED events are significantly dominant for $\eta' \rightarrow \gamma\gamma$ reactions; the production threshold for η' mesons is so high energetic that the recoil proton will likely be detected. Figure 3.1 shows the distribution of the different event classes for $\eta' \rightarrow \gamma\gamma$ production in MONTE CARLO data, with a clear preference towards 3PED events.

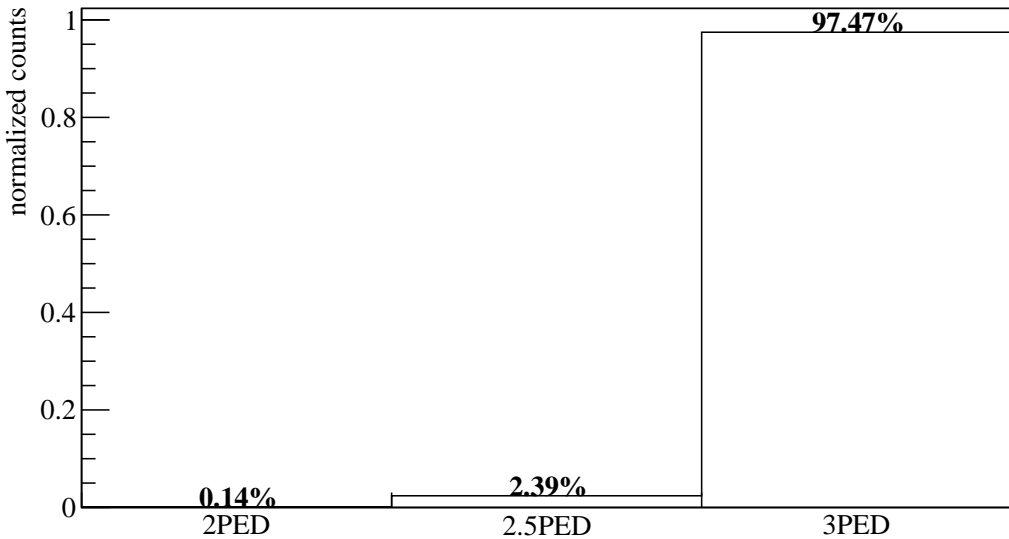


Figure 3.1: Distribution of event classes in $\eta' \rightarrow \gamma\gamma$ production

To further improve the signal to background ratio, the charge information of the final state particles was utilized in the next step. In particular, to select $\eta' \rightarrow \gamma\gamma$ reactions, one charged and two uncharged particles in the final state were demanded.

3.2 Time of particles

Due to its high count rate the tagging system (see section 2.1.1) will not only record beam photons which produce the detectable final state particles, but also several uncorrelated ones. To select only beam photons which will induce a photoproduction process the time information of the detected particles is used. It is shown in figure 3.2 for all particles involved in 2.5PED and 3PED events of η' photoproduction. In all cases prompt peaks centered around 0 ns (the trigger time) are visible. Since the final state photons move with velocity c their timing information does not underlie fluctuations, as is the case for the final state proton on the contrary. The tagged, uncorrelated beam photons are visible as flat background underneath the prompt peak in the time of the beam photon. Naturally, only coincident events may be referred to as η' candidates for the further analysis and thus only events

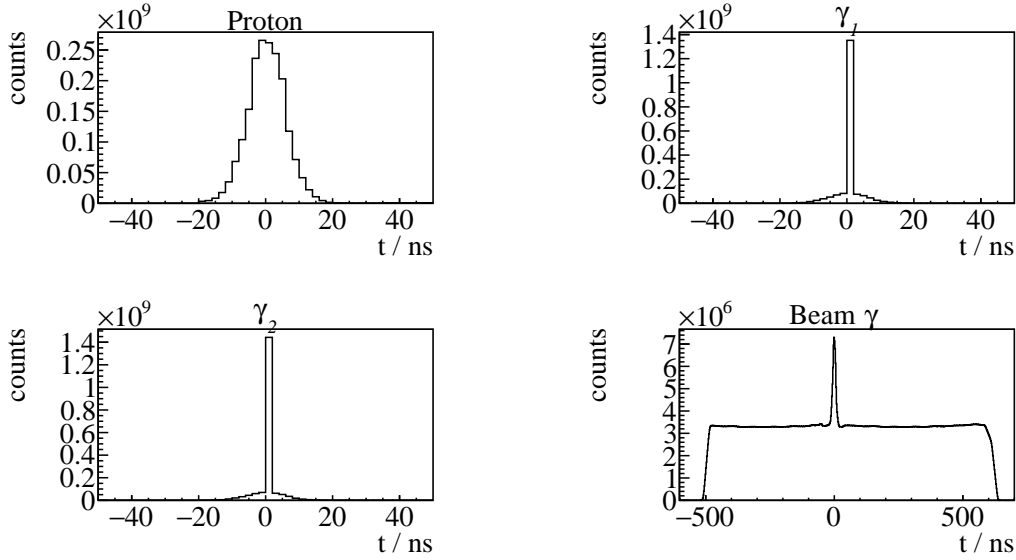


Figure 3.2: Time information of all final state particles and the beam photon for 3PED η' production

with time information of at least one final state particle are kept. Photons need to be detected in the MiniTAPS or forward detector to acquire time information. To determine coincidence it is convenient to define the *reaction time*

$$t_{\text{reaction}} = \begin{cases} t_{\text{beam}} - t_{\text{meson}} & \text{meson time exists} \\ t_{\text{beam}} - t_{\text{recoil}} & \text{meson time does not exist,} \end{cases} \quad (3.1)$$

where the meson time t_{meson} is appointed either the averaged time of both decay photons or the time of a single photon if only one photon has time information. t_{beam} and t_{recoil} are the time of the beam photon and recoil proton, respectively. Figure 3.3 shows the reaction time for 2.5PED and 3PED events; a clear prompt peak centred at 0 is visible, the colored area indicates the chosen range of $t_{\text{reaction}} \in [-8, 5]\text{ns}$. However, this cut still contains random time background underneath the prompt peak. This may be accounted for by *sideband subtraction*, assuming the background is flat. All events residing in the prompt peak with $t_r \in [-8, 5]\text{ns}$ will be assigned a weight of $w_p = +1$ while sideband events with $t_r \in [-200, -100]\text{ns} \vee t_r \in [100, 200]\text{ns}$ will be assigned a weight of $w_s = -\frac{13}{200}$. Events with t_r neither in the sideband nor in the prompt peak get assigned a weight of $w = 0$. Any histogram N that is filled in the following will then consist of prompt peak events N_{prompt} and sideband events N_{sideband}

$$N = N_{\text{prompt}} + w_s \cdot N_{\text{sideband}},$$

such that the random time background underneath the prompt peak is substracted. In addition, the time difference between meson and proton and between the two photons is demanded to be within $[-10, 10]\text{ns}$. All described cuts to the data, including the sideband subtraction are referred to as the *time cut* in the following.

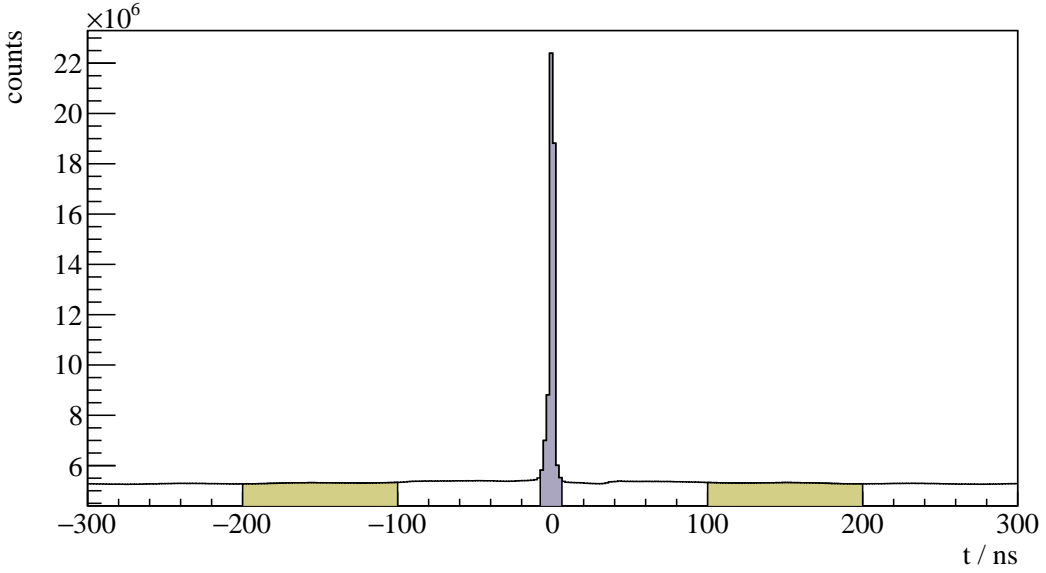


Figure 3.3: Reaction time t_r for 3PED η' production

3.3 Kinematic constraints

Up until now mainly combinatorical background was discussed. However one can derive kinematical constraints from energy and momentum conservation to exclusively select the desired reaction. The derivation is discussed first, followed by the determination of the derived cut conditions.

3.3.1 Derivation of cut conditions

Let p_{beam} and p_p be the four momenta of the initial state beam photon and proton, respectively. Then

$$p_{\text{beam}} + p_p = p_{\text{recoil}} + p_{\text{meson}} \quad (3.2)$$

holds, with p_{recoil} being the momentum of the recoiling proton and p_{meson} the meson momentum.

Coplanarity

In the initial state there is vanishing transversal momentum p_{xy} since the target protons are at rest and the beam photon impinges in z -direction. Naturally, this transversal momentum has to vanish in the final state as well, such that

$$\mathcal{P}_{xy} [p_{\text{recoil}} + p_{\text{meson}}] = 0, \quad (3.3)$$

where \mathcal{P}_{xy} is the projection operator to the transversal plane. Equation (3.3) is valid if and only if meson and proton lie back to back (coplanar) in the x - y plane, which is quantified by the difference of their azimuthal angles ϕ_{meson} and ϕ_{recoil} being 180° in the laboratory-frame

$$\Delta\phi := \phi_{\text{meson}}^{\text{LAB}} - \phi_{\text{recoil}}^{\text{LAB}} \stackrel{!}{=} 180^\circ. \quad (3.4)$$

Polar angle difference

If all initial and final state momenta are measured, the reaction described by equation (3.2) is *overdetermined*, such that one final state particle can be treated as a "missing particle" X with momentum p_X :

$$p_X = p_{\text{beam}} + p_p - p_{\text{meson}}. \quad (3.5)$$

One can then use

$$\Delta\theta := \theta_{p_X}^{\text{LAB}} - \theta_{p_{\text{recoil}}}^{\text{LAB}} \stackrel{!}{=} 0 \quad (3.6)$$

as a further constraint to the data.

Missing mass

The previously described angular cuts are only applicable if all final state particles have been detected. Independently of the detection of the recoil proton the mass of the missing particle $m_X^2 = p_X^2$ can be determined and compared with the proton mass of $m_p = 938.27 \text{ MeV}$ [Zyl+20]. From equation (3.5) it follows that

$$m_X = \sqrt{(E_\gamma + m_p - E_{\text{meson}})^2 - p_{x,\text{meson}}^2 - p_{y,\text{meson}}^2 - (E_\gamma - p_{z,\text{meson}})^2}. \quad (3.7)$$

Invariant mass

The measurement of the invariant mass of the two final state photons does also not require the measurement of the recoil proton. The knowledge of both four-momenta suffices, since

$$m_{\text{meson}} = \sqrt{p_{\text{meson}}^2} = \sqrt{(p_{\gamma_1} + p_{\gamma_2})^2} = \sqrt{2E_{\gamma_1}E_{\gamma_2}(1 - \cos\alpha_{\gamma_1\gamma_2})}, \quad (3.8)$$

where E_{γ_i} are the measured photon energies and $\alpha_{\gamma_1\gamma_2}$ is the angle spanned by the two photon momenta. To select only η' candidates $m_{\text{meson}} = m_{\eta'} = 957.78 \text{ MeV}$ is demanded. Remarkably, the cut on the invariant mass of the final state photons is the only one to uniquely select η' production candidates so far. All other cuts apply similarly to arbitrary meson photoproduction.

3.3.2 Determination of cut ranges

The constraints described in the previous section must not be understood as strict equalities, cf. equations (3.3), (3.6), (3.7) and (3.8). The quantities of interest will rather describe distributions around the desired value, such that confidence intervals may be extracted by fitting to said distributions. This is done iteratively:

Let C_I^χ be the cut operator that restrains the data \mathcal{D} such that the (generic) cut variable

$$\chi \in \{\Delta\theta, \Delta\phi, m_X, m_{\text{meson}}\}$$

lies in the interval $I \subseteq \mathbb{R}$, such that

$$C_I^\chi : \mathcal{D} \mapsto \mathcal{D}_{\chi \in I}. \quad (3.9)$$

After a first inspection of the data, initial guesses for the intervals I, J, K, L corresponding to the quantities $\Delta\theta, \Delta\phi, m_X, m_{\text{meson}}$, respectively, are made. Having established estimates for the cut ranges,

new ones are estimated by investigating the distribution of one cut variable obtained from the data while all other cut variables are constrained to the previously determined intervals. For example

$$\Delta\theta \left(C_{\mathcal{J}}^{\Delta\phi} C_{\mathcal{K}}^{m_X} C_{\mathcal{L}}^{m_{\text{meson}}} \mathcal{D} \right) \sim \text{normal}(\mu, \sigma),$$

where $\mu \approx 0$. This is done (with some adjustments to the fit function) for each cut variable. The parameters of the gaussian are determined from a χ^2 fit and used to assign new cut ranges. Simultaneously, Monte-Carlo (MC) data of relevant final states are fitted to match the measured values bin-wise. This is done on the one hand to check consistency between measured and MC data and on the other hand used to determine contributing background reactions. First, all mesonic final states that decay into two photons are considered, i.e. $p\pi^0, p\eta, p\eta'$, since the according peaks in the invariant mass spectrum will be visible. Also, a peak at the mass of the ω (vector)-meson m_ω will be visible; this stems from photoproduction reactions $p\omega \rightarrow p\pi^0\gamma \rightarrow p3\gamma$ where one low energetic final state photon is lost, such that the reconstructed invariant mass still estimates the ω mass. Further, one should investigate the impact of neutral final states, where some of the final state photons may get lost during reconstruction, as can be observed for $p2\pi^0, p\pi^0\eta, p3\pi^0, p2\pi^0\eta$ ¹ production. Lastly, possible misidentification of charged particles which then mimic a $p\gamma\gamma$ final state are examined, such as $p\pi^+\pi^-$ and $n\pi^+$. Table 3.2 lists all employed MC reactions and their respective final state particles, as well as a short explanation why the particular reaction was included in the fit.

Photoproduction reaction	Final state particles	Explanation
$p\pi^0$	$p\gamma\gamma$	prominent peak in the invariant mass spectrum
$p\eta$	$p\gamma\gamma$	
$p\omega$	$p\pi^0\gamma \rightarrow p3\gamma$	
$p\eta'$	$p\gamma\gamma$	
$p2\pi^0$	$p4\gamma$	lost photons cause a "3-particle" final state
$p\pi^0\eta$	$p4\gamma$	
$p3\pi^0$	$p6\gamma$	
$p2\pi^0\eta$	$p6\gamma$	
$p\pi^+\pi^-$		misidentification of charged particles
$n\pi^+$		

Table 3.2: Examined MC reactions that were used in sum for the fit

Since the invariant mass spectrum features rich contributions from many final states, it is difficult to describe by a (sum of) gaussian function(s), especially considering the background contributions. Thus, for the invariant mass the cut ranges are obtained from gaussian fits to the scaled MC data of the η' final state. Table 3.3 shows which fit function and cut range was used for each cut variable. In addition, it shows if the cut ranges were determined from MC or measured data. The newly obtained intervals $\mathcal{I}', \mathcal{J}', \mathcal{K}', \mathcal{L}'$ serve again as input for the previous step. This is repeated until a certain convergence is reached, which is usually the case after a two or three iterations. Since the cut ranges may vary depending on beam energy and meson direction, they are determined in bins of the beam

¹ all mesons m decaying into two photons is implied: $m \rightarrow \gamma\gamma \forall m$

cut variable	fit function	interval range	obtained from
$\Delta\theta$	GAUSS	$\mathcal{I}' = [\mu - 3\sigma, \mu + 3\sigma]$	data points
$\Delta\phi$	GAUSS	$\mathcal{J}' = [\mu - 3\sigma, \mu + 3\sigma]$	data points
m_X	NOVOSIBIRSK [Ike+00]	$\mathcal{K}' = [\mu - 2\sigma, \mu + 2\sigma]$	data points
m_{meson}	GAUSS	$\mathcal{L}' = [\mu - 2\sigma, \mu + 2\sigma]$	MC data

Table 3.3: Fit functions and cut ranges for each variable

energy and the polar angle of the meson in the center of mass system (CMS)

$$(E_\gamma, \cos \theta_{\eta'}^{\text{CMS}})^2.$$

Respecting the η' final state statistics, a binning of $\Delta E_\gamma = 100$ MeV and $\Delta \cos \theta = 1/3$ was chosen, spanning the energy range of 1 500 to 1 800 MeV. The theoretically accessible lower limit in the beam energy is provided by the production threshold of η' mesons at 1 447 MeV [Zyl+20]. Yet, the binning has to comply with the upper beam energy limit which is bounded from above³ by the position of the coherent edge of the beamtime. It is given by 1 700 MeV and 1 800 MeV for the July/August and September/October beam times, respectively. If one were to include the production threshold into the analyzed range using the same binning, more background than η' events are collected from 1 400 to 1 500 MeV (see subsection 3.4.3), hence the chosen binning starts at 1 500 MeV.

Coplanarity

Figure 3.4 shows the coplanarity spectra for the energy bin $1 500 \text{ MeV} \leq E_\gamma < 1 600 \text{ MeV}$ and all angular bins. The data points are visualized by the open circles with error bars, while the black solid histogram is a fit of $\eta' \rightarrow \gamma\gamma$ MC. As expected, a clear peak is visible at $\Delta\phi = 180^\circ$, which shows only slight dependence on beam energy and meson direction. A 3σ interval obtained from a gaussian fit is indicated by the dashed red lines. Note that only MC spectra of the η' final state were fitted to the data since the coplanarity gives little reference points for a correct estimation of other final states that may contribute.

Polar angle difference

Since the meson direction correlates with the detector(s) the final state photons hit, the polar angle difference depicts a clear directional dependence as can be seen in figure 3.5 for the energy bin $1 500 \text{ MeV} \leq E_\gamma < 1 600 \text{ MeV}$ and all angular bins. In the CMS frame, meson and proton are emitted back to back. Thus, if the meson is emitted in backward direction ($\cos \theta \sim -1$), the proton will be detected either in the forward or MiniTAPS detector, which have a better angular resolution than the Crystal Barrel calorimeter, leading to narrower distributions of $\Delta\theta$. The determined cut ranges are 3σ intervals obtained from a gaussian fit to the data and are indicated by the red dashed lines. As before, no other than η' MC are fitted to the spectra.

² If not otherwise specified, from now on $\cos \theta = \cos \theta_{\eta'}^{\text{CMS}}$

³ Significantly beyond the coherent edge, the systematic error for the beam polarization degree gets too large (> 10%)

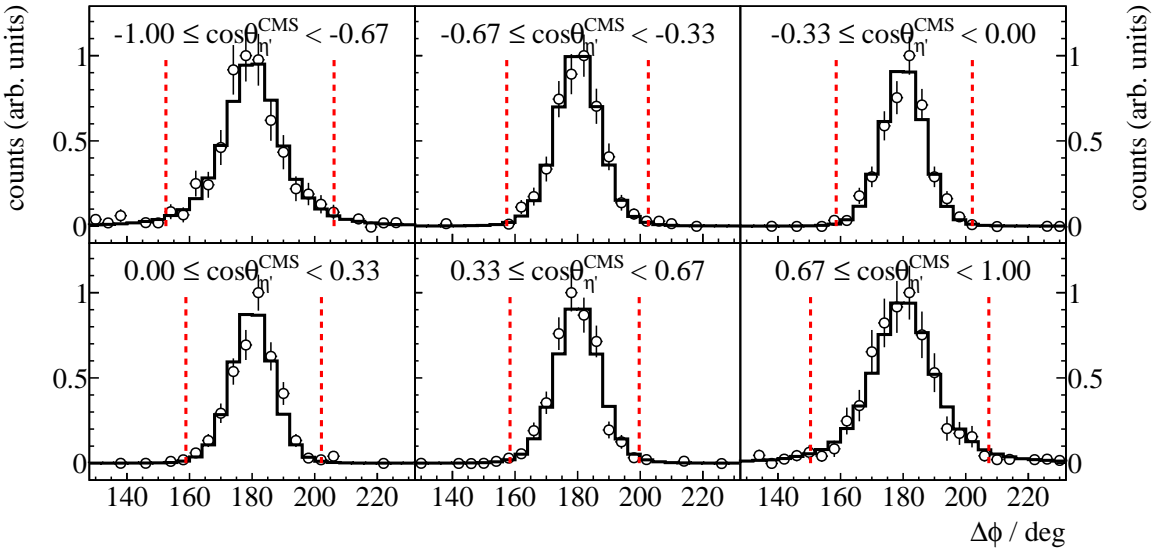


Figure 3.4: Coplanarity of the $p\eta'$ final state with all other cuts applied for the energy bin $1500 \text{ MeV} \leq E_\gamma < 1600 \text{ MeV}$. The vertical dashed lines show the cut ranges obtained from a gaussian fit to the data (open circles). The solid black histograms represent fitted MC data of $\eta' \rightarrow \gamma\gamma$

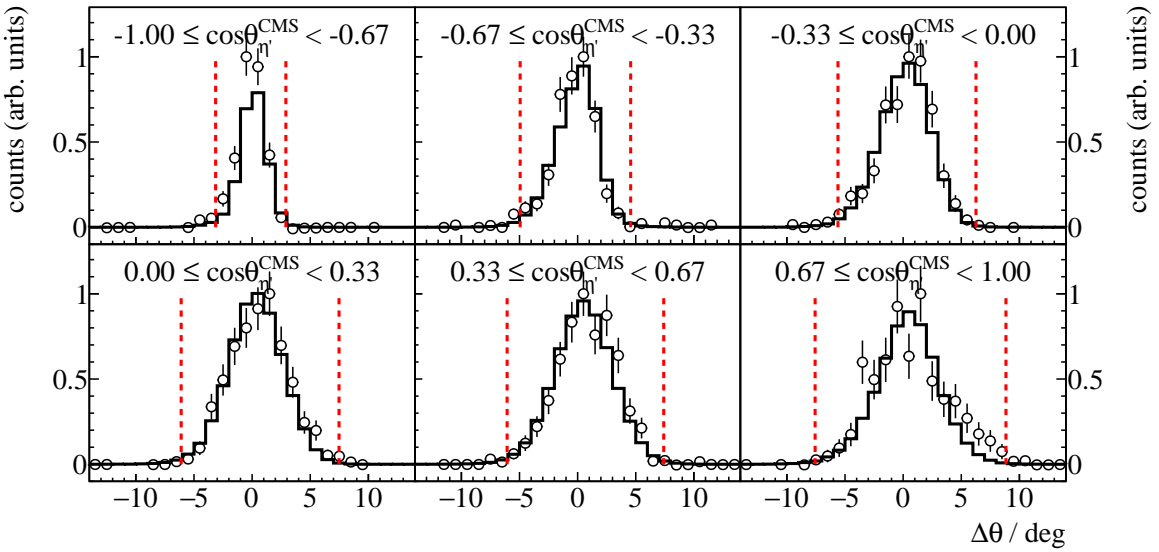


Figure 3.5: Polar angle difference of the $p\eta'$ final state with all other cuts applied for the energy bin $1500 \text{ MeV} \leq E_\gamma < 1600 \text{ MeV}$. The vertical dashed lines show the cut ranges obtained from a gaussian fit to the data (open circles). The solid black histograms represent fitted MC data of $\eta' \rightarrow \gamma\gamma$

Missing mass

The missing mass spectra allow a first investigation of possible background reactions that pass event selection. For all angular bins of the first energy bin the missing mass is shown in figure 3.6; again, the open circles are the data points with corresponding statistical error bars. The solid colored histograms are fitted MC spectra of different possible background contributions while the black histogram is the signal contribution of $\eta' \rightarrow \gamma\gamma$ photoproduction. The turquoise histogram is the sum of all MC histograms. Generally, most of the data can be described by the η' MC alone, but especially towards higher masses (and higher beam energies) background contributions extend the missing mass peak as flat background. These are reactions where the reconstructed meson mass $m_{\text{meson}}^2 = E_{\text{meson}}^2 - \vec{p}_{\text{meson}}^2$ is smaller than the η' mass, resulting in larger values for the missing mass. Judging from the fit to the missing mass, $2\pi^0$ and/or $\pi^0\eta$ photoproduction may describe the background as both show similar shapes. All other previously mentioned reactions (table 3.2) do not contribute significantly. Better conclusions can be drawn from the invariant mass spectra as is discussed in the following section 3.4. The cut ranges for the missing mass are obtained from a Novosibirsk [Ike+00] fit to the data since the missing mass distribution is slightly asymmetric. However, since the tail parameter is small, still a symmetric cut of $\pm 2\sigma$ was chosen. It was chosen narrower than the angular cuts to collect less background reactions.

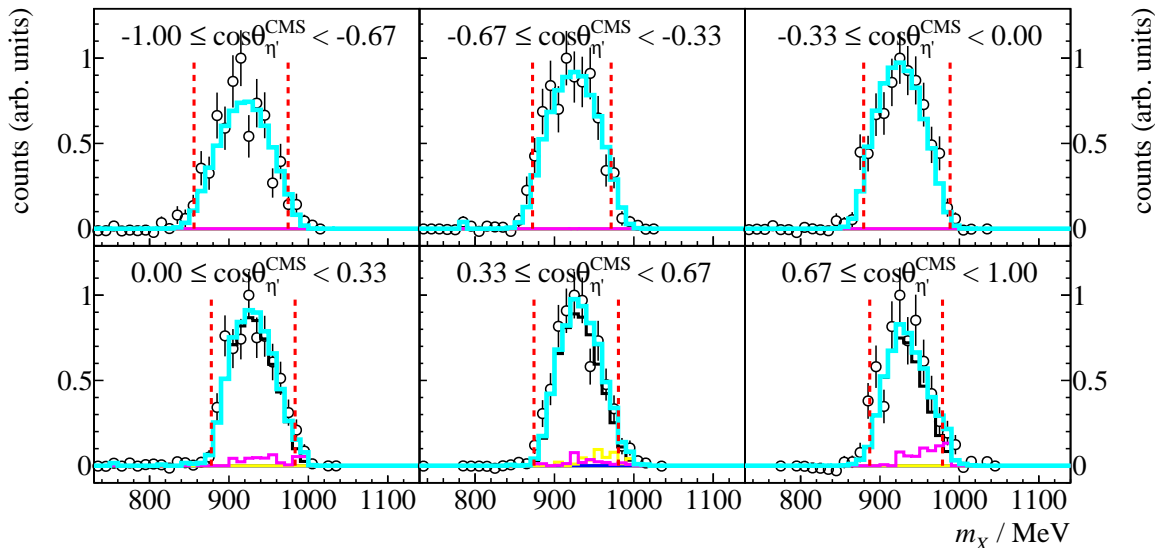


Figure 3.6: Missing mass of the $p\eta'$ final state with all other cuts applied for the energy bin $1500 \text{ MeV} \leq E_\gamma < 1600 \text{ MeV}$. The vertical dashed lines show the cut ranges obtained from a fit to data (open circles) employing a Novosibirsk function. The solid colored histograms represent fitted MC data from relevant photoproduction reactions: in black η' , in green π^0 , in red η , in blue ω , in yellow $2\pi^0$, magenta $\pi^0\eta$. The turquoise histogram is the sum of all MC histograms.

Invariant mass

Investigating the invariant mass spectrum of the final state photons allows to illustrate the impact of the event selection so far. As has been mentioned all cuts considered up to this point apply to arbitrary meson photoproduction. This means that the invariant mass spectrum will depict peaks belonging to mesons produced in the considered beam energy range. This is shown in figure 3.7 giving an overview over all energy and angular bins. All other cuts have been applied. The open circles represent data points and the different colored histograms MC data from relevant competing final states while the black histogram shows the signal contribution of η' MC. The turquoise histogram is the sum of all MC contributions and describes the data very well. It has again been found that no other than the shown final states contribute significantly or improve the description of data by MC spectra. As expected one can observe peaks belonging to π^0 , η , ω and η' photoproduction. A flat background underneath the complete spectrum is realized by $2\pi^0$ and $\pi^0\eta$ final state photons that have been wrongfully combined to two photons. Remarkably, the π^0 , η and ω invariant mass distributions also depict long tails towards lower and higher masses, although they contribute only marginally to the sum of all MC spectra (note the logarithmic y-Scale). They can be explained by the fact that one low energetic photon is lost during reconstruction while the (high energetic) proton wrongfully creates two tracks of which one is then combined with the other photon as meson candidate [Afz19]. To finally select only η'

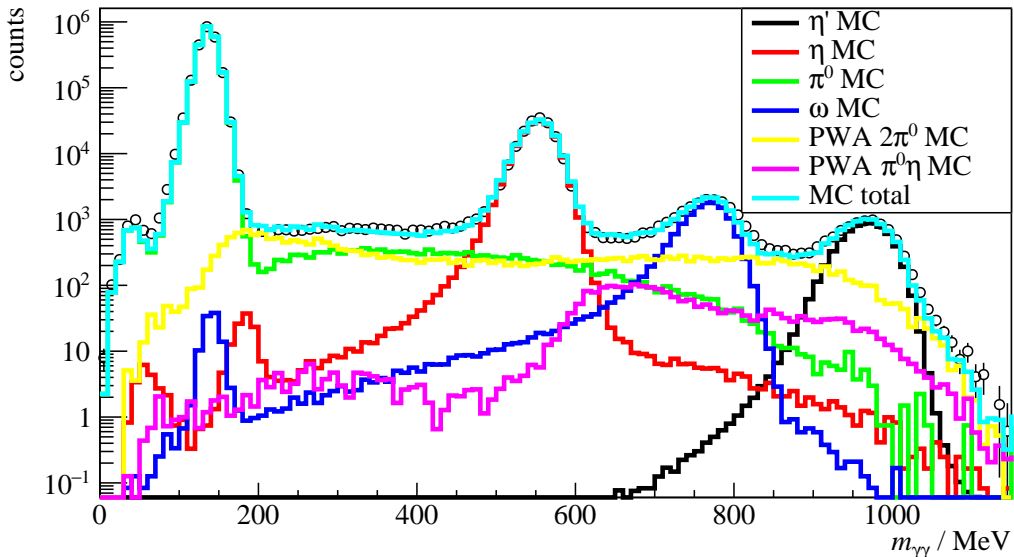


Figure 3.7: Invariant mass of the $p\eta'$ final state with all other cuts applied for all energy and angular bins. The open circles represent the measured data, the solid colored histograms fitted MC data from relevant photoproduction reactions: in black η' , in green π^0 , in red η , in blue ω , in yellow $2\pi^0$ and in magenta $\pi^0\eta$. The turquoise histogram is the sum of all MC histograms.

photoproduction event candidates the invariant mass cut is determined again in bins of beam energy and meson polar angle. This is shown in figure 3.8 for the first energy bin with all angular bins. Here, the same color coding as before applies, but the range of the invariant mass has been reduced to only cover the η' peak for visibility's sake. Additionally the cut ranges, representing a 2σ interval obtained

from a gaussian fit to the η' MC, are shown as dashed, red lines. Considering the statistics the MC spectra still describe the data well. It is found again that the significant background contributions in the invariant mass range of interest are given by $2\pi^0$ and $\pi^0\eta$ photoproduction.

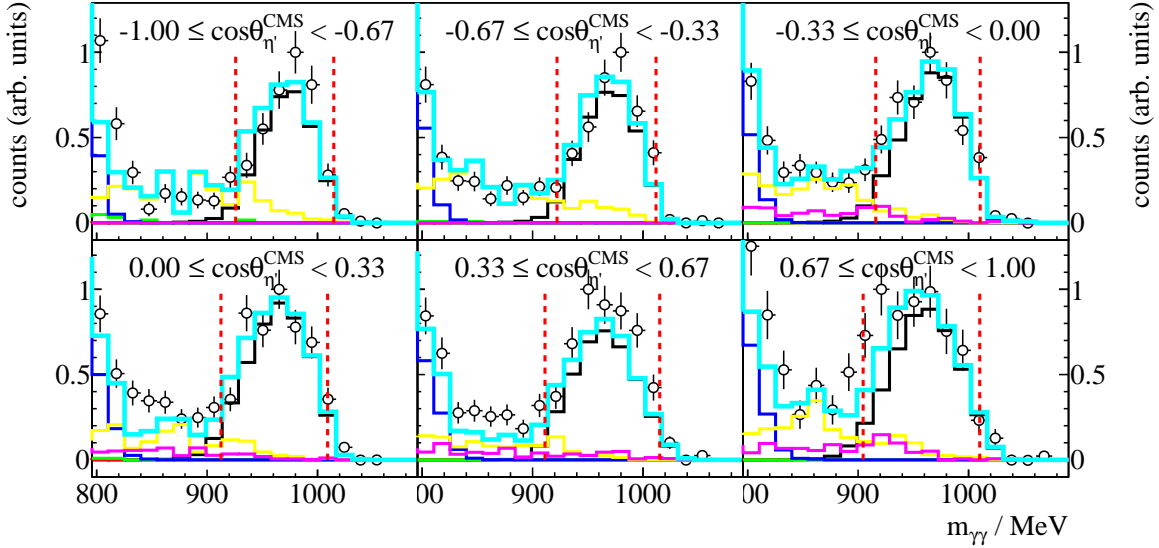


Figure 3.8: Invariant mass of the $p\eta'$ final state with all other cuts applied for the energy bin $1500 \text{ MeV} \leq E_\gamma < 1600 \text{ MeV}$. The vertical dashed lines show the cut ranges obtained from a gaussian fit to the η' MC data (solid black histogram). The open circles represent the measured data, the solid colored histograms fitted MC data from relevant photoproduction reactions: in black η' , in green π^0 , in red η , in blue ω , in yellow $2\pi^0$ and in magenta $\pi^0\eta$. The turquoise histogram is the sum of all MC histograms.

3.3.3 Quality of event selection

In order to investigate the impact of applied cuts the detector and analysis acceptance $A(E_\gamma, \cos \theta)$ can be investigated. It is defined as the ratio of reconstructed events $N^{\text{rec}}(E_\gamma, \cos \theta)$ to generated events $N^{\text{gen}}(E_\gamma, \cos \theta)$

$$A := \frac{N^{\text{rec}}(E_\gamma, \cos \theta)}{N^{\text{gen}}(E_\gamma, \cos \theta)} \quad (3.10)$$

and is shown in figure 3.9. Acceptance holes are visible in very forward and in backward direction which can be contributed to events where the proton escapes the calorimeters or is absorbed in insensitive material. Also, events close to threshold are unlikely to be reconstructed which can also be explained by low energy protons and/or low energy photons. A maximum acceptance of $\tilde{A} \approx 0.61$ is reached which can be understood considering the cuts that have been made; each 3σ cuts retains 99% of events and each 2σ cut 95%. Assuming detection efficiencies of 90% for the two uncharged photons and 85% for the charged proton ([Afz19; Har17]) it is evident that $0.99^2 \cdot 0.95^2 \cdot 0.9^2 \cdot 0.85 \approx 0.61$. In total, $8 \cdot 10^3 \eta'$ events were extracted which nonetheless still contain background contaminations. In order to take this into account in the later analysis the fraction of background is determined for each

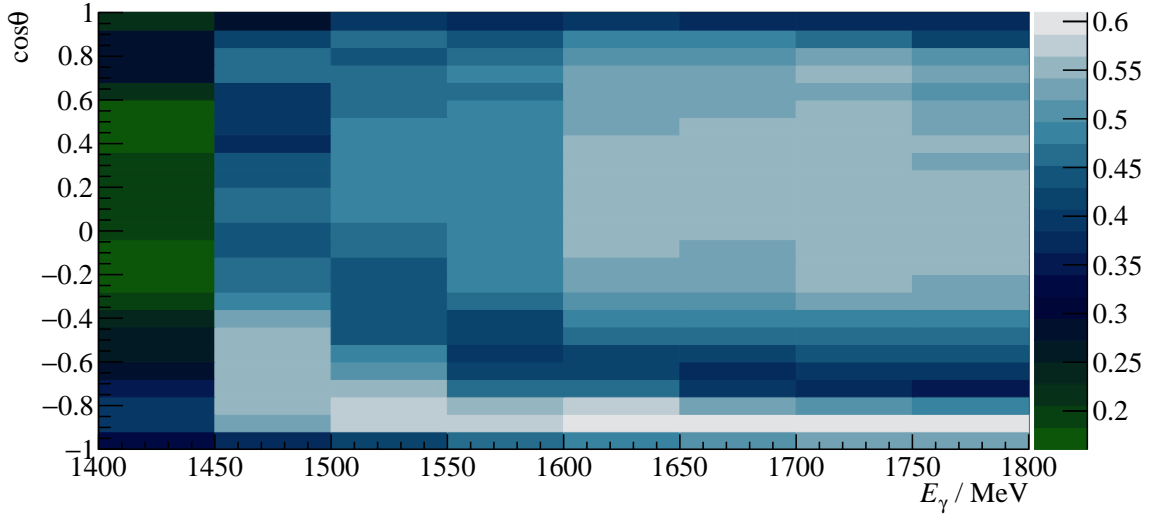


Figure 3.9: Acceptance for the reaction $\gamma p \rightarrow p\eta'$ after all cuts that have been discussed so far for 2.5PED and 3PED events

bin in beam energy and meson polar angle. It is estimated as the fraction of background MC events to total MC events and shown in figure 3.10. For most bins around 15% of all events are misidentified as η' events. Especially at very forward $\cos \theta \rightarrow 1$ and backward $\cos \theta \rightarrow -1$ angles the background contributions are significantly higher, reaching up to 45%.

3.4 Investigation of background and additional cuts

So far the background reactions in the η' cut ranges have been discussed only phenomenologically as they describe the measured invariant mass spectra best. In the following the plausibility and causality of these background contributions shall be discussed. Furthermore it is investigated if the found background contributions may be reduced or eliminated by additional cut conditions.

3.4.1 Inspecting plausibility of background reactions

To evaluate the likelihood that the background contributions are made up of $2\pi^0$ or $\pi^0\eta$ production events the respective production cross sections in the inspected beam energy region and branching ratios (BR) to purely photonic final states are examined, see table 3.4. Also displayed is the maximum acceptance \tilde{A} which is additionally shown in figure 3.11. Both possible background reactions exceed η' photoproduction in cross section and also in relative frequency of purely photonic final states. At the same time the acceptance is almost vanishing, proving that the kinematic cuts are generally very effective.

Since the total number of events is proportional to the cross section σ , branching ratio BR and

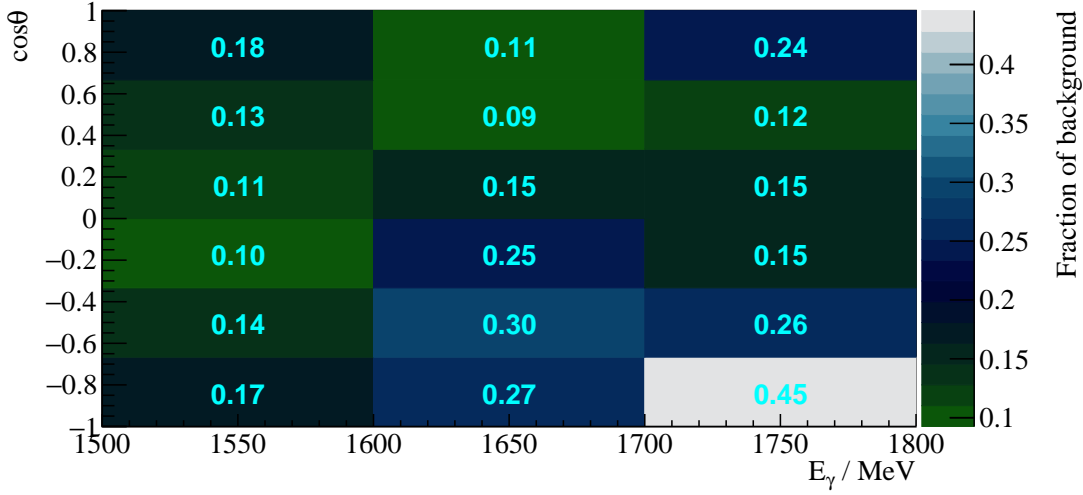


Figure 3.10: Fraction of background events in the analyzed beam energy and angular bins.

reaction	$\sigma / \mu\text{b}$	BR to $n\gamma$	\tilde{A}
$\gamma p \rightarrow p\eta'$	≈ 1 [Cre+09]	0.02	0.61
$\gamma p \rightarrow p2\pi^0$	$\lesssim 5$ [Die+20]	$0.98^2 = 0.96$	$7 \cdot 10^{-4}$
$\gamma p \rightarrow p\pi^0\eta$	≈ 3 [Käs+18]	$0.98 \cdot 0.38 = 0.37$	$2 \cdot 10^{-4}$

Table 3.4: Total cross sections σ in the energy range 1 500 to 1 800 MeV, branching ratios (BR) to $n\gamma$ final states and maximum acceptance \tilde{A} for signal and possible background contributions

acceptance \tilde{A} , the ratio of reconstructed background to signal events is then given by

$$R = \frac{\sigma \cdot \text{BR} \cdot \tilde{A}}{\sigma_{\eta'} \cdot \text{BR}_{\eta' \rightarrow \gamma\gamma} \cdot \tilde{A}_{\eta'}} = \frac{\sigma \cdot \text{BR} \cdot \tilde{A}}{1 \mu\text{b} \cdot 0.02 \cdot 0.61}.$$

One finds $R \lesssim 0.3$ and $R \lesssim 0.05$ for $2\pi^0$ and $\pi^0\eta$ photoproduction, respectively. Although less than 0.1% of two meson production reactions are misidentified as η' events they make up a significant portion of background in η' data, as considering the according branching ratios and cross sections showed. Furthermore, the previous empirical assumption to only include $2\pi^0$ and $\pi^0\eta$ MC in the fit to describe the data is now justified since the found background percentages agree well with the now motivated upper boundaries.

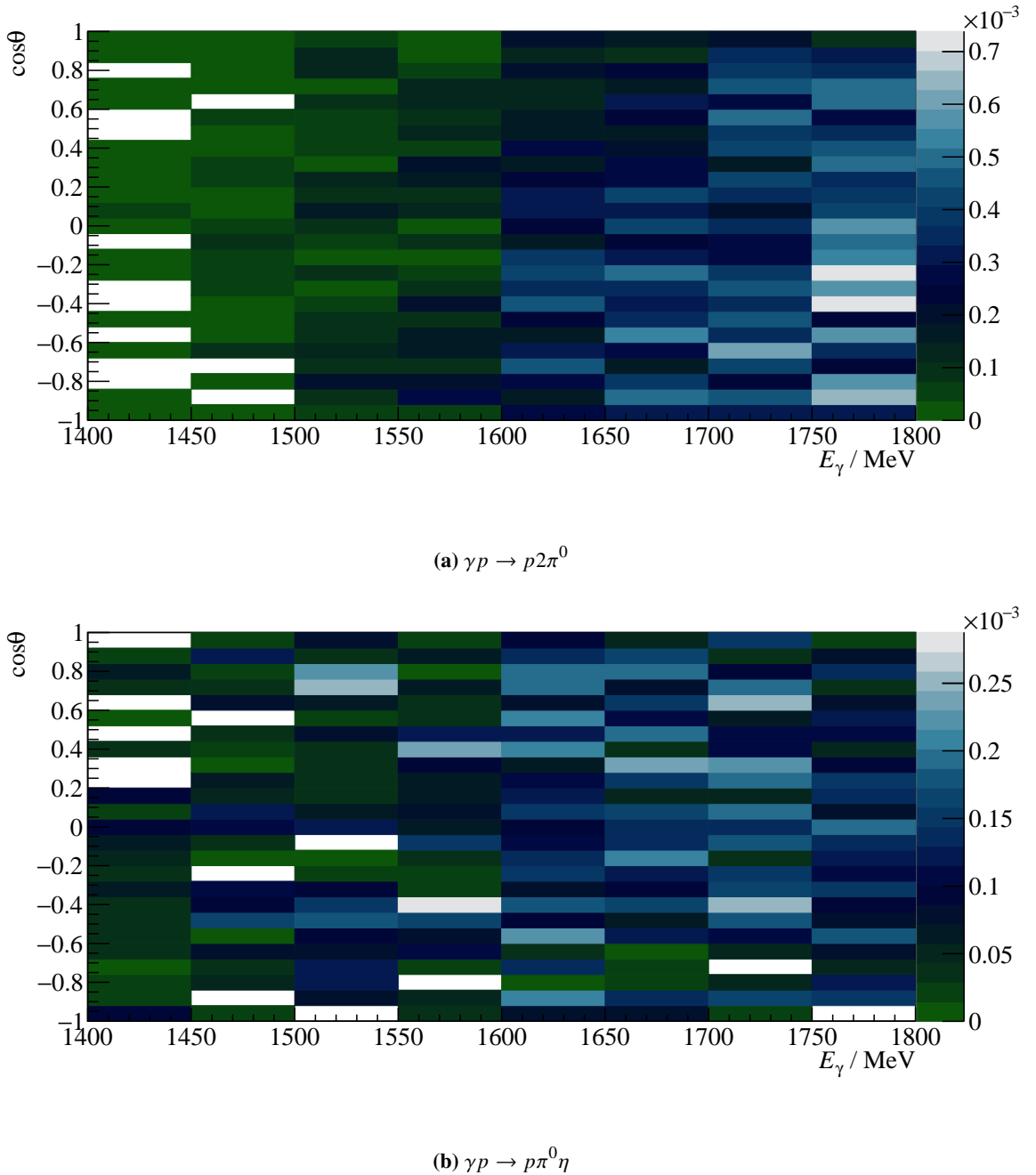


Figure 3.11: Acceptance for possible background contributions

3.4.2 Misidentification of background reactions

It has been reasonably established that the main background reactions that escape the η' event selection cuts are realized by $2\pi^0$ and $\pi^0\eta$ production. However, it remains to explain why a four-photon final state is misidentified as η' event. In order to do so the MC simulations of the respective final states were investigated. One observes that for those events that passed the η' cuts the generated photon energies for two photons often were of order $E_{\gamma,i} \sim \mathcal{O}(10 \text{ MeV})$ and the other two of order $E_{\gamma,i} \sim \mathcal{O}(100 \text{ MeV})$. The reconstructed energies however only displayed energies of order $E_{\gamma,i} \sim \mathcal{O}(100 \text{ MeV})$. During the reconstruction of final state four momenta, a minimum energy of 20 MeV per cluster is demanded in order to suppress electromagnetic background. This threshold is not passed or only closely passed by both lowest energy final state photons of $2\pi^0$ production for $\sim 60\%$ of all events, see figure 3.12. Similarly, $\sim 70\%$ of $\pi^0\eta$ events have a final state photon which does not or only closely pass

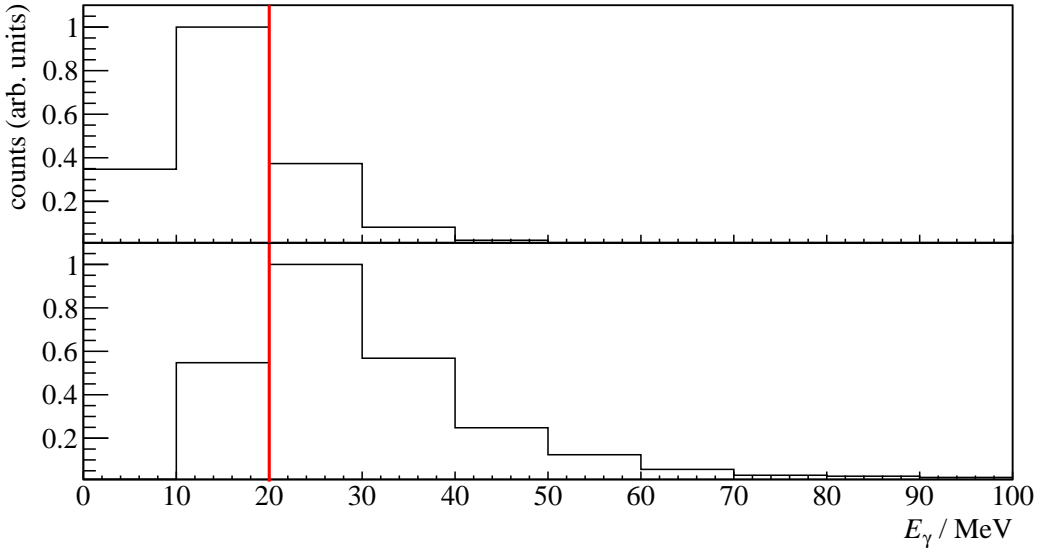


Figure 3.12: Generated energies of the two lowest energy photons in $2\pi^0$ photoproduction MC data. The threshold of 20 MeV is marked by a vertical red line. Lowest energy photon is shown on the top, second lowest energy photon is shown on the bottom.

the threshold of 20 MeV. Other than in $2\pi^0$ reactions, this does only apply for one of the lowest energy photons while the other significantly exceeds the threshold of 20 MeV, see figure 3.13. Those photons with an energy above threshold may still be lost during reconstruction because they are falsely combined to one cluster with one of the two highest energy photons as a investigation of photon directions revealed; figure 3.14 shows the polar angle difference between the second lowest energy photon and the second highest energy photon of the MC $\pi^0\eta$ final state which clearly peaks centered at 0. Similar results are found with $2\pi^0$ production events. It is evident that neither the two lost photons, nor the two reconstructed photons are correlated, i.e. decay products of the same meson.

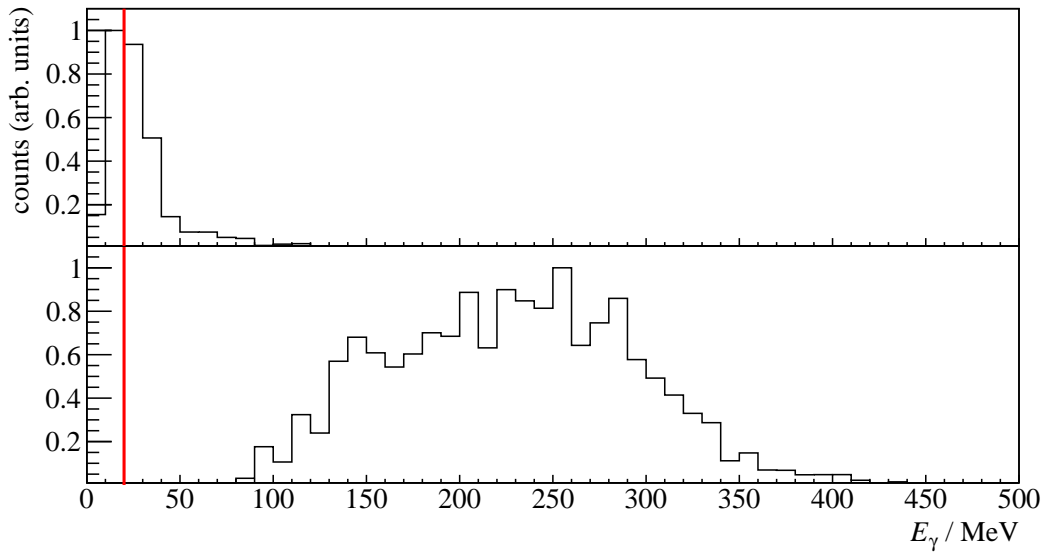


Figure 3.13: Generated energies of the two lowest energy photons in $2\pi^0$ and $\pi^0\eta$ photoproduction MC data. The threshold of 20 MeV is marked by a vertical red line. Lowest energy photon is shown on the top, second lowest energy photon is shown on the bottom.

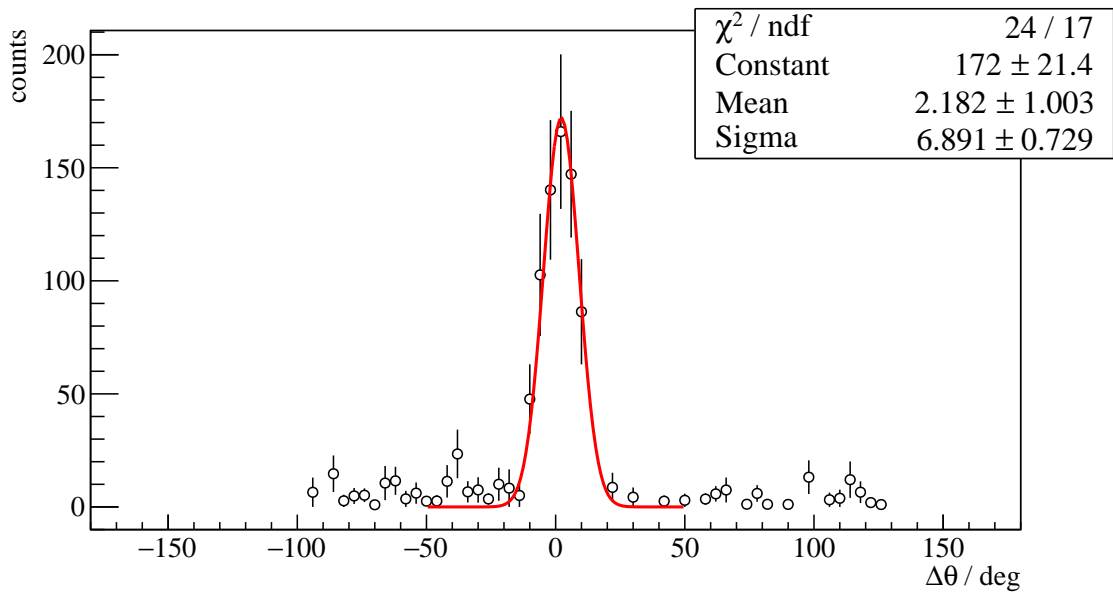
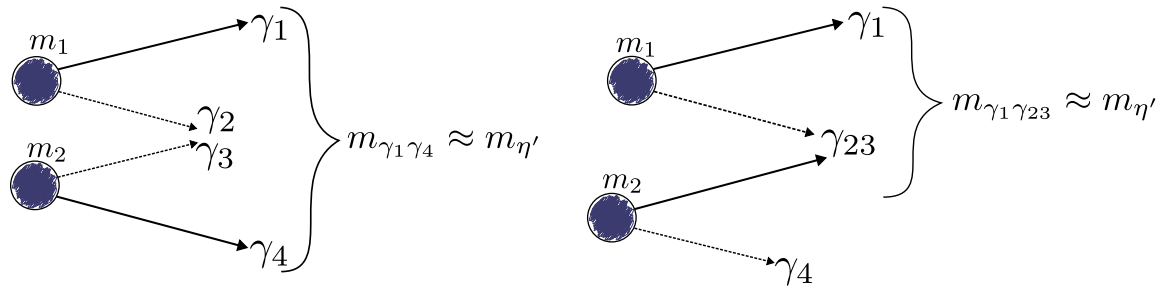


Figure 3.14: Polar angle difference $\Delta\theta$ between the photon with second highest energy and second lowest energy of the $\pi^0\eta$ final state.

Considering the above one can now say that $2\pi^0$ and $\pi^0\eta$ events pass the η' event selection because

1. two uncorrelated low energy photons are lost during reconstruction and the remaining two pass the kinematic cuts by chance, since they too are uncorrelated (see figure 3.15a),
2. one low energy photon is lost. Two of the remaining three photons are combined to one in favor of the higher energetic photon since they were emitted in the same direction. The two reconstructed photons are uncorrelated and pass the event selection randomly, as shown in figure 3.15b.



(a) Two photons get lost while the remaining two get falsely combined to form a η' meson
 (b) One photon gets lost, in addition two photons are grouped as one. The remaining two get falsely combined to form a η' meson

Figure 3.15: Illustration of the misidentification process during reconstruction

These claims are indeed further validated if one examines the polar angle that is reconstructed from the falsely assigned η' candidates using the surviving two photon momenta. This can be compared to the generated polar angle that is built using all four final state photon momenta in the CMS \mathbf{p}_{γ_i} . They add up to the artificial two-meson momentum \mathbf{p}_m which in the CMS has the same magnitude but opposite direction as the recoil proton with momentum $\mathbf{p}_{\text{recoil}}$

$$\mathbf{p}_m = \sum_{i=1}^4 \mathbf{p}_{\gamma_i} = -\mathbf{p}_{\text{recoil}}.$$

If the lost photons have very low energies and/or are emitted in the same direction as other photons one would expect the polar angle that is spanned by the four final state photons approximately agrees with the polar angle that is built using the two photons that survived event selection, such that $\cos \theta(4\gamma) \approx \cos \theta(2\gamma)$. This is exactly what is observed, as figure 3.16 shows for both background reactions: the generated CMS angle $\cos \theta_{\text{gen.}}$ is plotted against the reconstructed CMS angle $\cos \theta_{\text{rec.}}$. The events are clearly distributed around the slope $\cos \theta_{\text{gen.}} = \cos \theta_{\text{rec.}}$ which is indicated by the solid line. This is an important result for the later analysis: if the background contributions are taken into account quantitatively then the extracted beam asymmetry has to be corrected by the asymmetry stemming from background reactions. This is only possible if the background reactions from e.g. $2\pi^0$ events realize the same bins in beam energy and CMS angle as in a dedicated measurement of the beam asymmetry in the respective photoproduction reaction.

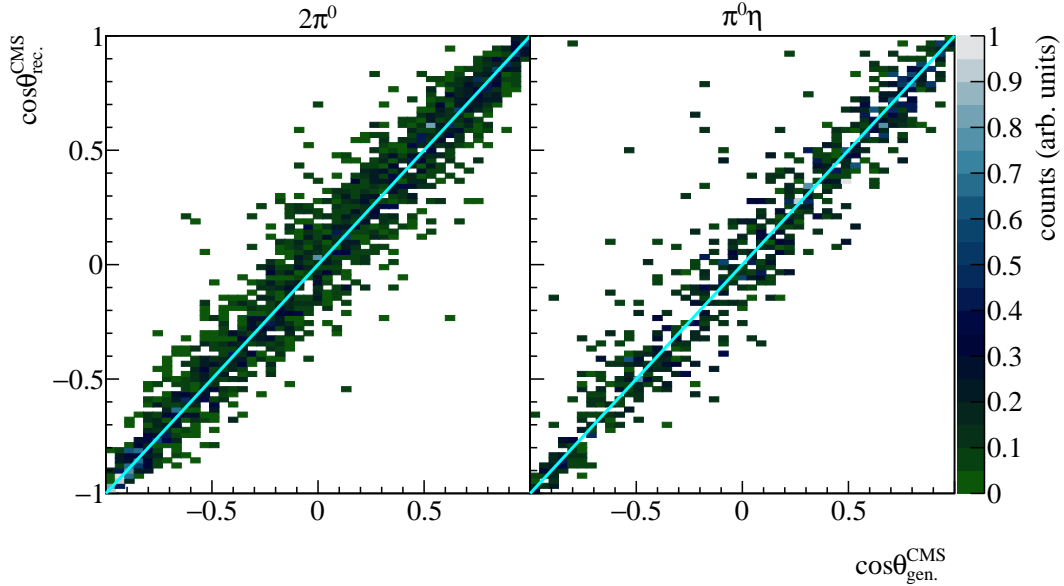


Figure 3.16: Generated CMS angle $\cos\theta_{\text{gen.}}$ vs. reconstructed CMS angle $\cos\theta_{\text{rec.}}$ for both background reactions. The slope $\cos\theta_{\text{gen.}} = \cos\theta_{\text{rec.}}$ is indicated by the solid line.

3.4.3 Examination of additional cuts

Since the background contributions are significantly beyond a negligible amount it would be desirable to remove them through additional cuts that at the same time do not remove too many signal events. However, this proved to be a complicated task because the background reactions are reconstructed from real photons which happen to be in the η' invariant mass range. Therefore they are not distinguishable from $\eta' \rightarrow \gamma\gamma$ photons in terms of energy, momentum (direction) or created clustersize in the calorimeter crystals. The combination of two photons into one also is not observable as such since the impact of one photon with energy E may create a cluster with clustersize C which at the same time can be created by two photons in the same direction with energies $E_1 + E_2 = E$ and clustersizes $C_1 + C_2 = C$. Thus, to find any characteristics that separate background from signal events, one has to analyze properties of either the recoil proton or the reaction kinematics as a whole.

Proton cut

Very close to the η' production threshold, the meson system is not boosted very much in forward direction as long as real η' mesons are produced. As a consequence the recoil proton may escape to very forward angles in the lab system which corresponds to the proton being detected in the MiniTAPS calorimeter. Falsely reconstructed $2\pi^0$ or $\pi^0\eta$ events have lower production thresholds such that the mesons will be boosted forward and the recoil proton is detected rather in the foward detector or the Crystal Barrel calorimeter. Figure 3.17 shows for the first two energy bins (starting at 1 400 MeV) the detector that was hit by the recoil proton for η' , $2\pi^0$ and $\pi^0\eta$ MC data. At threshold nearly all protons of η' events are detected in the MiniTAPS calorimeter while this is only the case for 57% of $2\pi^0$ events and 20% of $\pi^0\eta$ events. Towards higher energies this distribution along detectors smears out

and is approximately equal for all reactions. Yet, not enough statistics are collected in the energy bin close to threshold for a cut based on the proton detector hit to have significance, as this bin contains less than 7% of total η' candidates. The poor statistics in this bin also make determining background from MC fits difficult. Thus, as has been mentioned before, the energy bin from 1 400 to 1 500 MeV was not included in the analysis. Consequently no cut based on proton detector hits could be applied to the remaining data. Apart from directional information near threshold protons from signal and background events could not be distinguished.

Reaction kinematics

As has been mentioned before, the measured photoproduction reactions are in fact overdetermined, meaning that one reaction particle can be treated as missing. This can be used to calculate the beam photon energy

$$E_\gamma^{\text{calc}} = \frac{-0.5 \cdot m_{\eta'}^2 + m_p E_{\eta'}}{m_p - E'_{\eta'} + |p_z|_{\eta'}}, \quad (3.11)$$

where m_p is the proton $m_{\eta'}$ the η' mass, $E_{\eta'}$ is the meson energy and $|p_z|_{\eta'}$ is the meson momentum in z -direction. Comparing this with the measured beam energy one may tell η' events apart from background events where mesons with smaller masses have been produced. If equation (3.11) is used to calculate the beam energy, i.e. inserting the η' mass, background events from reactions with smaller masses will cause smaller calculated beam energies. The difference of measured and calculated beam energy $\Delta E = E_\gamma^{\text{meas}} - E_\gamma^{\text{calc}}$ is shown in figure 3.18. The data points are shown as open circles and solid histograms represent fitted MC data where the turquoise histogram is the sum of all MC histograms. A broad peak centred slightly off 0 towards lower energy differences is visible. It also exhibits a broad shoulder towards higher energy differences. The MC describe the data very well, consisting mainly of η' and $2\pi^0$ MC, as expected. Yet, the $\pi^0\eta$ MC describe a shape very similar to the $2\pi^0$ MC. The background MC show a trend towards energy differences > 0 , as predicted by equation (3.11). In principle the distribution of background and η' MC now allow to introduce an upper bound on the beam energy difference rejecting any desired amount of background. However, simultaneously a significant amount of η' events have to be discarded if this cut should have remarkable influence on the background events, as is shown in table 3.5.

upper limit of ΔE / MeV	rel. loss of signal events / %	relative loss of bkg. events / %	
		$2\pi^0$	$\pi^0\eta$
0	36	71	59
50	21	53	36
100	10	33	18
150	4	15	6

Table 3.5: Relative loss in signal and background events if a cut on ΔE is applied.

Considering that only 8000 η' candidates could be extracted, any cut removing sizable fractions of signal events will have grave impact regarding the statistical error for the later analysis of the beam asymmetry. It was decided not to imply any further cuts on the data and proceed with the selected events as described previously. Because results for the beam asymmetry in $2\pi^0$ and $\pi^0\eta$ production are

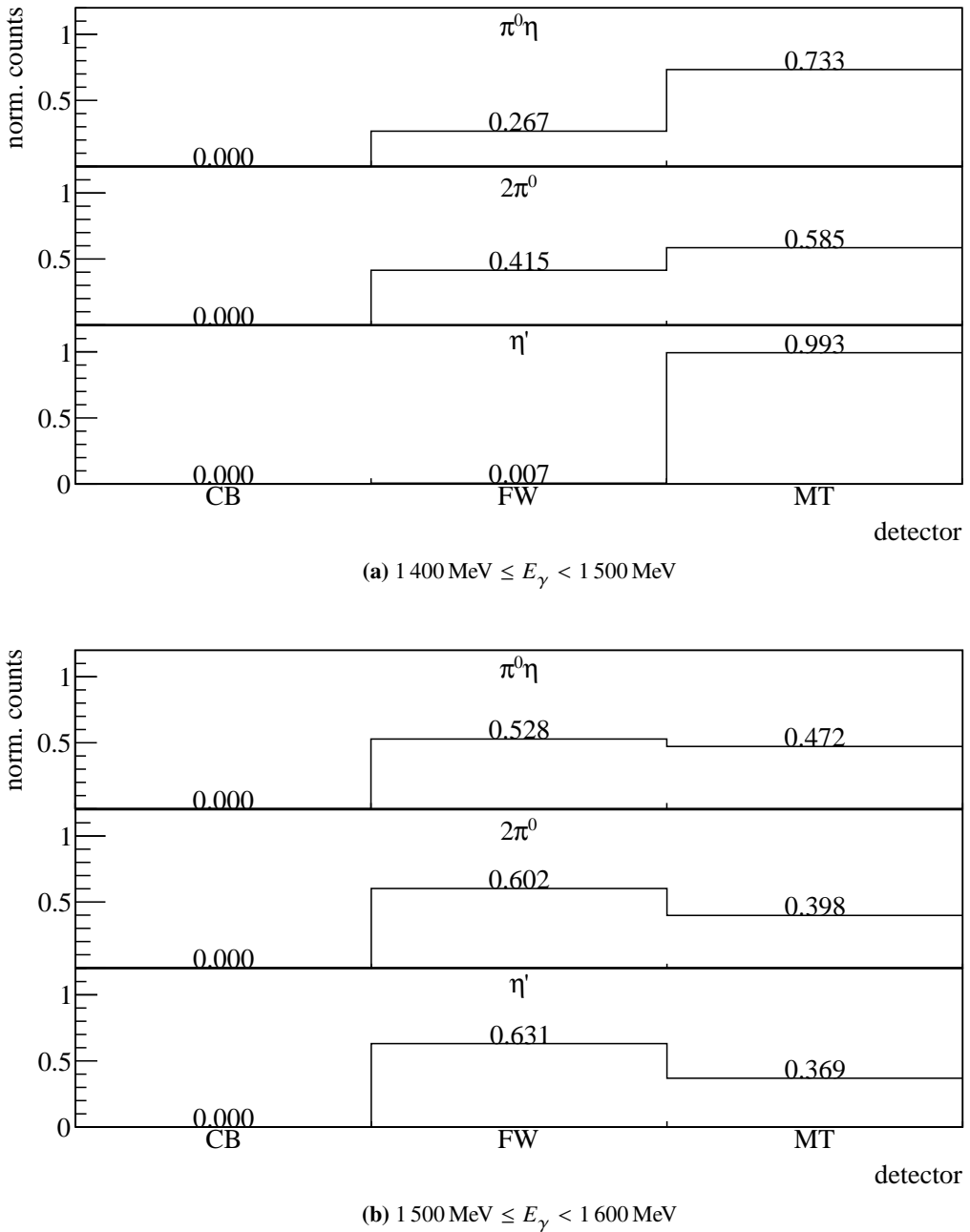


Figure 3.17: Detector hits of the recoil proton, as obtained from MC data for the production of η' , $2\pi^0$ and $\pi^0\eta$.
 CB: Crystal Barrel, FW: forward detector, MT: MiniTAPS

available CITE(P. Mahlberg, Georg Urff?) it is not crucial to remove all remaining background events since the extracted beam asymmetry can be corrected proportionately, depending on the amount and type of background in a particular bin.

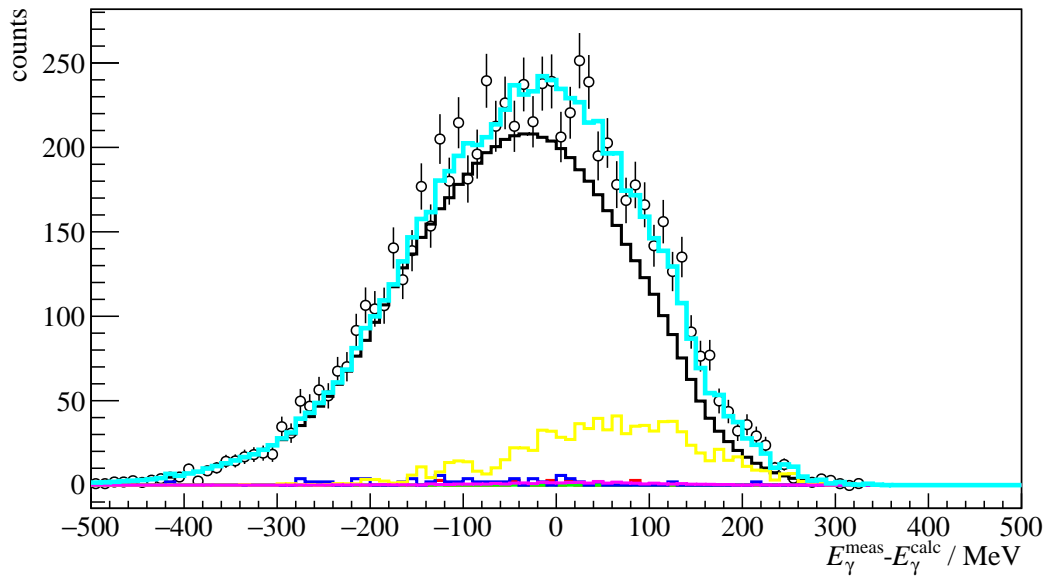


Figure 3.18: Difference in measured and calculated beam energy. Data points are shown as open circles, MC data as solid histograms: in black η' , in green π^0 , in red η , in blue ω , in yellow $2\pi^0$ and in magenta $\pi^0\eta$. The turquoise histogram is the sum of all MC histograms.

3.5 Summary of event selection

The reaction $\gamma p \rightarrow p\eta'$ could be selected successfully. Combinatorial background was removed using the time information of initial and final state particles. Furthermore, the measured energies and momenta of all final state particles were utilized when applying constraints, that were derived from energy and momentum conservation, to $\gamma p \rightarrow \eta' \rightarrow \gamma\gamma$ event candidates. A significant amount of background still passes the event selection process which could be traced back to $2\pi^0$ and $\pi^0\eta$ production using Monte Carlo simulations. Very restricted possibilities to exclusively select signal from background events were found but in the end not used as they still remove sizable fractions of signal events in order to get rid of background events.

To illustrate again the impact of all applied cuts, the invariant mass summed over all angular and energy bins of the final state photons is shown again in figure 3.19 where the spectrum can be seen after each individual cut successively. While at first only slight structures in the invariant mass spectrum can be observed, in the end a clear, peak-like structure is visible, indicating the general success of the event selection that has been described in this chapter. The signal to background ratio is improved by each applied cut where the time cut clearly removes the most (combinatorial) background. Note that there are differences of three and two orders of magnitude in statistics for π^0 or η meson production compared to η' production in the neutral decay channel.

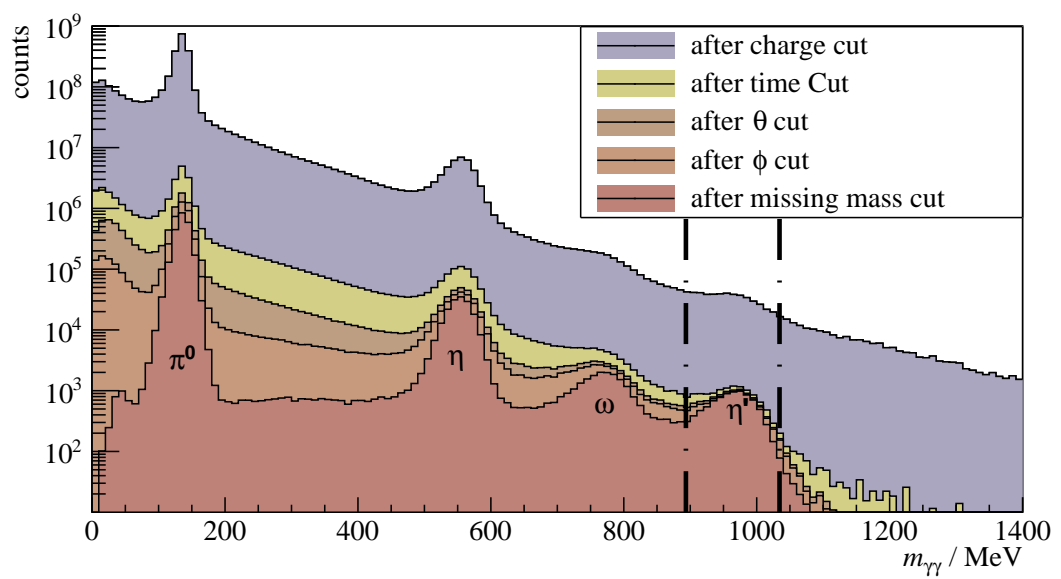


Figure 3.19: Invariant mass spectrum passing different stages in the event selection process. In the end clear peaks for all possibly produced mesons are visible. The vertical lines indicate the mean cut ranges over all energy and angle bins.

CHAPTER 4

Extraction of the beam asymmetries Σ_η and $\Sigma_{\eta'}$

The beam asymmetry Σ is observable when a linearly polarized photon beam and unpolarized liquid hydrogen target are employed. The polarized cross section $\frac{d\sigma}{d\Omega_{\text{pol}}}$ is not symmetric in the azimuthal angle ϕ anymore as opposed to the unpolarized cross section $\frac{d\sigma}{d\Omega_0}$. It is rather modulated by a cosine dependence which scales with the polarization observable Σ and the (linear) beam polarization p_γ , see equation (4.1) [San+11].

$$\frac{d\sigma}{d\Omega_{\text{pol}}} (E_\gamma, \cos \theta, \phi) = \frac{d\sigma}{d\Omega_0} (E_\gamma, \cos \theta) \cdot \left[1 - p_\gamma \Sigma (E_\gamma, \cos \theta) \cos (2\varphi) \right] \quad (4.1)$$

Since the incident photon beam is polarized, photon momentum \vec{k} and polarization $\vec{\epsilon}$ span a plane which is referred to as the beam polarization plane. This plane is tilted by the angle φ with respect to the reaction plane which is defined by the final state momenta. Naturally, this plane builds the angle ϕ in the laboratory system. At the same time the angle of the beam polarization plane in the same reference frame is defined as α . It holds

$$\varphi = \alpha - \phi. \quad (4.2)$$

Figure 4.1 illustrates definitions of all angles and planes. Theoretically the beam asymmetry can be

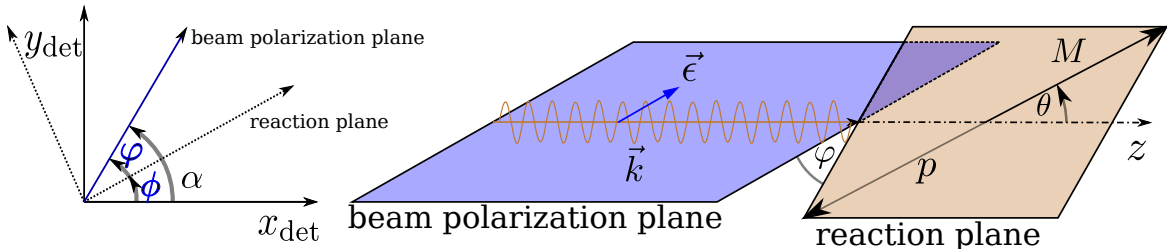


Figure 4.1: Left: Definition of angles α, ϕ, φ . Right: Photon momentum \vec{k} and polarization $\vec{\epsilon}$ define the beam polarization plane while the reaction plane is defined by the recoil proton p and produced meson M .

determined by a measurement of the cross section and a fit using equation (4.1). However, when calculating polarized cross sections, it is important to have good control over flux normalization and detector acceptance in three dimensions ($E_\gamma, \cos \theta, \phi$). To avoid this, the measurement of asymmetries

can be used to access the polarization observable Σ instead. Particularly, data is taken for two distinct orthogonal polarization settings corresponding to $\alpha = \pm 45^\circ$.

This chapter will illustrate the process of determining the beam asymmetry for η and η' photoproduction. The published results of Σ_η [Afz19; Afz+20] are used to check the accuracy and functionality of employed bayesian methods. Bayesian methods, as well as traditional frequentist approaches are used afterwards to extract new results for $\Sigma_{\eta'}$. First, the used methods will be presented and subsequently their application for each final state, respectively.

4.1 Methods

The beam asymmetry has to be determined via fits to ϕ distributions obtained from data. These are performed as either binned or unbinned fits. Both methods allow the application of Bayesian methods as will be discussed in the following. Additionally the advantages and disadvantages off all methods are compared.

4.1.1 Event yield asymmetries

Measurements were made in two distinct polarization settings $\alpha = \pm 45^\circ = \alpha^{\perp/\parallel}$. Thus, the polarized cross sections for both settings are given by¹

$$\frac{d\sigma^{\parallel}}{d\Omega_{\text{pol}}} = \frac{d\sigma}{d\Omega_0} \cdot \left[1 - p_\gamma^{\parallel} \Sigma \cos(2(\alpha^{\parallel} - \phi)) \right] \quad (4.3)$$

and

$$\frac{d\sigma^{\perp}}{d\Omega_{\text{pol}}} = \frac{d\sigma}{d\Omega_0} \cdot \left[1 - p_\gamma^{\perp} \Sigma \cos(2(\alpha^{\perp} - \phi)) \right] \quad (4.4)$$

$$= \frac{d\sigma}{d\Omega_0} \cdot \left[1 + p_\gamma^{\perp} \Sigma \cos(2(\alpha^{\parallel} - \phi)) \right]. \quad (4.5)$$

Note that equation (4.5) holds, because

$$\alpha^{\perp} = \alpha^{\parallel} + \pi/2 \quad \text{and} \quad \cos x = -1 \cdot \cos(x + \pi).$$

Consider now taking the difference of equations (4.3) and (4.5)

$$\frac{d\sigma^{\perp}}{d\Omega_{\text{pol}}} - \frac{d\sigma^{\parallel}}{d\Omega_{\text{pol}}} = \frac{d\sigma}{d\Omega_0} \cdot \left(p_\gamma^{\perp} + p_\gamma^{\parallel} \right) \Sigma \cos(2(\alpha^{\parallel} - \phi)). \quad (4.6)$$

One can further eliminate the unpolarized cross section from this equation by dividing by the polarization weighted sum of equations (4.3) and (4.5)

$$\alpha \cdot \frac{d\sigma^{\perp}}{d\Omega_{\text{pol}}} + \beta \cdot \frac{d\sigma^{\parallel}}{d\Omega_{\text{pol}}} = \frac{d\sigma}{d\Omega_0} \cdot \left[\alpha + \beta - \left(\alpha p_\gamma^{\perp} - \beta p_\gamma^{\parallel} \right) \Sigma \cos(2(\alpha^{\parallel} - \phi)) \right] \stackrel{!}{=} 2 \frac{d\sigma}{d\Omega_0}. \quad (4.7)$$

¹ The dependencies of polarized and unpolarized cross sections as well as the beam asymmetry like in equation (4.1) are implied

Since

$$\frac{d}{d\phi} \frac{d\sigma}{d\Omega_0} \stackrel{!}{=} 0 \forall \phi,$$

it holds

$$\alpha p_\gamma^{\parallel} - \beta p_\gamma^{\perp} \stackrel{!}{=} 0 \quad \alpha + \beta \stackrel{!}{=} 2, \quad (4.8)$$

such that

$$\alpha = \frac{2p_\gamma^{\parallel}}{p_\gamma^{\perp} + p_\gamma^{\parallel}} \quad \beta = \frac{2p_\gamma^{\perp}}{p_\gamma^{\perp} + p_\gamma^{\parallel}}. \quad (4.9)$$

The beam asymmetry Σ is thus accessible via the asymmetry

$$A(\phi) = \frac{\frac{d\sigma^{\perp}}{d\Omega \text{ pol}} - \frac{d\sigma^{\parallel}}{d\Omega \text{ pol}}}{p_\gamma^{\parallel} \frac{d\sigma^{\perp}}{d\Omega \text{ pol}} + p_\gamma^{\perp} \frac{d\sigma^{\parallel}}{d\Omega \text{ pol}}} = \Sigma \cos(2(\alpha^{\parallel} - \phi)). \quad (4.10)$$

At this point one can now make use of the fact that in any scattering reaction the number of events N is given by the product of luminosity L and total cross section σ

$$N = L \cdot \sigma = \Phi \cdot N_t \cdot \frac{d\sigma}{d\Omega} \cdot \Delta\Omega,$$

where Φ is the beam flux, N_t the number of target particles and $\Delta\Omega$ is the solid angle covered by the detector. Substituting this in equation (4.10) one can build the asymmetry $A(\phi)$ using only the (flux-)normalized event yields $\tilde{N}^{\parallel/\perp}(E_\gamma, \cos\theta, \phi)^2$

$$A(\phi) = \frac{\tilde{N}^{\perp} - \tilde{N}^{\parallel}}{p_\gamma^{\parallel} \tilde{N}^{\perp} + p_\gamma^{\perp} \tilde{N}^{\parallel}} = \Sigma \cos(2(\alpha^{\parallel} - \phi)). \quad (4.11)$$

Alternatively, the event yields N can also be normalized by integrating over the total azimuthal angle range in each bin of $(E_\gamma, \cos\theta)$. This normalization technique has been used in reference [Afz19] and will also be used in this work. Using appropriate binning in ϕ in addition to beam energy and meson polar angle the asymmetry can be build for all kinematic bins and the beam asymmetry then be extracted via a one-Parameter fit. The statistical errors for $A(\phi)$ are given by GAUSSIAN error propagation (see appendix A.1).

Frequentist

The beam asymmetry can now be determined via a frequentist fit, where Σ is determined such that the χ^2 value resulting from the data points and equation 4.11 is minimized. The results are point estimates with statistical error bars that are also obtained from the fit: $\hat{\Sigma} \pm \sigma_{\hat{\Sigma}}$. In addition $\chi^2/\text{NDF} \approx 1$ may be verified in order to diagnose the fit itself. Multiple automated minimization and calculation algorithms

² again, arguments $(E_\gamma, \cos\theta, \phi)$ are implied.

for χ^2 fitting are available as open source. The *Python* [RP22] module `scipy` [Vir+20] and *ROOT* [BR97] offer e.g. the methods `scipy.optimize.curve_fit` [sci] and `TH1::Fit()` [ROOa] for discrete/binned data, which were used in the analysis.

BAYESIAN

Following section 1.3, where the basics of BAYESIAN inference were discussed, the goal of a BAYESIAN approach is to sample marginal posterior distributions for each fitted parameter from the joint posterior $p(\theta|y)$ which depends on the observed data y . The joint posterior itself is proportional to the product of priors $\pi(\theta)$ and likelihood $\mathcal{L}(y|\theta)$ (BAYES’ theorem). This collapses to a one parameter problem in the case of fitting the event yield asymmetries (Eq. (4.11))

$$p(\Sigma|y) \propto \pi(\Sigma) \cdot \mathcal{L}(y|\Sigma). \quad (4.12)$$

However, to be able to sample from a joint posterior, prior and likelihood need to be specified. In order not to bias the fit towards any particular values, the prior is chosen non-informative, realized by a broad GAUSSIAN centered at 0 which is truncated to the physically allowed parameter space of $\Sigma \in [-1, 1]$. Furthermore, the likelihood is formulated assuming GAUSSIAN errors ϵ_n at each data point y_n , which should be described by the asymmetry (Eq (4.11)) at bin n $A(\phi_n; \Sigma)$, i. e.³

$$\Sigma \sim \mathcal{N}(0, 1)_{[-1, 1]} \quad y_n = A(\phi_n; \Sigma) + \epsilon_n \quad \epsilon_n \sim \mathcal{N}(0, \sigma_n), \quad (4.13)$$

which is equivalent to

$$\Sigma \sim \mathcal{N}(0, 1) \quad y_n \sim \mathcal{N}(A(\phi_n; \Sigma), \sigma_n). \quad (4.14)$$

The likelihood of all data points now evaluates to the product of the likelihood at each data point y_n and the posterior results in

$$p(\Sigma|y) \propto \pi(\Sigma) \cdot \mathcal{L}(y|\Sigma) = \mathcal{N}(\Sigma|0, 1)_{[-1, 1]} \cdot \prod_n \mathcal{N}(y_n|A(\phi_n; \Sigma), \sigma_n) \quad (4.15)$$

$$\Leftrightarrow -\ln p(\Sigma|y) = \frac{1}{2}\Sigma^2 + \frac{1}{2} \sum_n \left(\frac{y_n - A(\phi_n; \Sigma)}{\sigma_n} \right)^2 + \text{constant terms}, \quad (4.16)$$

such that all ingredients are present to form a fully BAYESIAN probabilistic model⁴. This model was implemented in Stan [Sta22], directly giving access to samples from the posterior obtained with the No-U-Turn-Sampler (NUTS) [Sta22; HG14]. Hereby, the sampling is restricted to the allowed parameter region $\Sigma \in [-1, 1]$. As a measure of goodness of fit, the p -values obtained from the posterior predictive distributions, as introduced in section 1.3, are reviewed. To diagnose the convergence of the MCMC fit, sensible values for \hat{R} and the Monte-Carlo standard error σ_{MCSE} are verified.

³ Remember the notation introduced in section 1.3: $x \sim \mathcal{N}(\mu, \sigma) = \mathcal{N}(x|\mu, \sigma) = \frac{1}{\sqrt{2\pi\sigma^2}} e^{-\frac{(x-\mu)^2}{2\sigma^2}}$

⁴ Note that the sampling aims only to reflect the right proportionality of the (marginal) posterior. Thus, constant terms can be dropped and are of no further interest [Sta22].

4.1.2 Event based fit

Although intuitive and easily implementable the binned fit –BAYESIAN or not– has one critical disadvantage: it is inevitable that information is lost because the asymmetry $A(\phi)$ is a binned quantity and hence, the choice of binning influences the fit results. This is discussed in more detail in appendix B. Especially kinematic bins with low statistics show this behavior. To circumvent this problem, an *unbinned fit*, based on the likelihood function for each event, can be performed. Also, no assumptions on the distribution of statistical errors have to be made since each event is taken into account individually. Yet, the event based fit does not provide any measure of goodness of fit, so that the study of toy Monte Carlo data is essential when checking the working principle of the method.

In a polarized experiment the azimuthal angle distribution of events is not isotropic, but modulated by a cosine term coupling to beam asymmetry Σ and beam polarization $p_\gamma^{\parallel/\perp}$ for each setting $\alpha^{\parallel/\perp}$, as is expressed through the respective differential cross sections in Equations 4.3 and 4.4. Since the number of events is proportional to the cross section, the probability $p(\phi, p_\gamma^{\parallel/\perp} | \Sigma)$ to find an event under the azimuthal angle ϕ for a given bin of $(E_\gamma, \cos \theta)$ and setting $\alpha^{\parallel/\perp}$ is⁵

$$p(\phi, p_\gamma^{\parallel/\perp} | \Sigma) = \frac{[1 \mp p_\gamma^{\parallel/\perp} \Sigma \cos(2(\alpha^\parallel - \phi))]}{\frac{1}{2\pi} \int_0^{2\pi} d\phi [1 \mp p_\gamma^{\parallel/\perp} \Sigma \cos(2(\alpha^\parallel - \phi))]} \quad (4.17)$$

This is only true for an idealized experiment with acceptance $\epsilon = \text{const} \forall \phi$, so that the acceptance $\epsilon(\phi)$ has to be included in the probability for each event. As demonstrated in reference [Har17] a FOURIER series truncated after the fourth order is sufficient to model any occurring function

$$\epsilon(\phi) = \sum_{k=0}^4 a_k \sin(k\phi) + b_k \cos(k\phi),$$

where the eight detector coefficients a_k and b_k are determined from the fit. With this the measurable probability $\tilde{p}(\phi, p_\gamma^{\parallel/\perp} | \Sigma, a, b)$ is

$$\tilde{p}(\phi, p_\gamma^{\parallel/\perp} | \Sigma, a, b) \propto [1 \mp p_\gamma^{\parallel/\perp} \Sigma \cos(2(\alpha^\parallel - \phi))] \cdot \epsilon(\phi) \quad (4.18)$$

$$= [1 \mp p_\gamma^{\parallel/\perp} \Sigma \cos(2(\alpha^\parallel - \phi))] \cdot \left(\sum_{k=0}^4 a_k \sin(k\phi) + b_k \cos(k\phi) \right), \quad (4.19)$$

where $a := \{a_k\}_{k=0}^4$, $b := \{b_k\}_{k=0}^4$. Finally, normalizing $\frac{1}{2\pi} \int_0^{2\pi} d\phi \tilde{p}(\phi, p_\gamma^{\parallel/\perp} | \Sigma, a, b) \stackrel{!}{=} 1$,

$$\tilde{p}(\phi, p_\gamma^{\parallel/\perp} | \Sigma, a, b) = \frac{[1 \mp p_\gamma^{\parallel/\perp} \Sigma \cos(2(\alpha^\parallel - \phi))] \cdot \left(\sum_{k=0}^4 a_k \sin(k\phi) + b_k \cos(k\phi) \right)}{1 \pm \frac{1}{2} a_2 p_\gamma^{\parallel/\perp} \Sigma}. \quad (4.20)$$

⁵ Note: Normalizing $p(\phi, p_\gamma^{\parallel/\perp} | \Sigma)$ to 2π (or any other arbitrary constant) is sufficient for the fit as long as the integral does not depend on the fit parameters. The normalization to 2π is chosen for better readability. However, to calculate actual probabilities, one must multiply Eq. (4.17) by 2π .

The respective polarization setting $\alpha^{\parallel/\perp}$ determines the sign in the normalizing constant which allows an uncorrelated estimation of the detector coefficient a_2 and the beam asymmetry Σ . To simplify notation and implementation, Equation (4.21) can be written as *one* probability for all events – regardless of polarization setting – if the polarization values p_γ^\parallel are multiplied by (-1) and summarized as p_γ :

$$\tilde{p}(\phi, p_\gamma | \Sigma, a, b) = \frac{[1 + p_\gamma \Sigma \cos(2(\alpha - \phi))] \cdot (\sum_{k=0}^4 a_k \sin(k\phi) + b_k \cos(k\phi))}{1 - \frac{1}{2}a_2 p_\gamma \Sigma}, \quad (4.21)$$

with $\alpha = -45^\circ$ fixed.

In section 3.2 the subtraction of uncorrelated time background was discussed via a sideband subtraction. Naturally, without binning the data, this strategy is invalid and prompt peak and sideband events have to be fitted simultaneously. Hereby it is important to consider that the random time background is realized as flat distribution underneath the complete reaction time spectrum (cf. Figure 3.3), *including* the range of the prompt peak. The fraction of true coincident events to random coincidences is given as

$$f = \frac{N_{\text{prompt}} - w \cdot N_{\text{sideband}}}{N_{\text{prompt}}}, \quad (4.22)$$

where N_{prompt} and N_{sideband} are the number of events where the reaction time lies within the prompt peak or sideband, respectively. w is the ratio of the widths of the chosen prompt peak and sideband ranges, see section 3.2. It is now assumed that the random coincidences will exhibit an asymmetry Σ^{bkg} of their own and are not necessarily described by the detector coefficients a and b but rather by a^{bkg} and b^{bkg} . The probability to detect a prompt peak event p_{prompt} and the probability to measure a sideband event p_{sideband} are then given by

$$p_{\text{prompt}}(\phi, p_\gamma, |\Sigma, a, b, \Sigma^{\text{bkg}}, a^{\text{bkg}}, b^{\text{bkg}}) = f \cdot \tilde{p}(\phi, p_\gamma | \Sigma, a, b) + (1 - f) \cdot \tilde{p}(\phi, p_\gamma | \Sigma^{\text{bkg}}, a^{\text{bkg}}, b^{\text{bkg}}) \quad (4.23)$$

$$p_{\text{sideband}}(\phi, p_\gamma | \Sigma^{\text{bkg}}, a^{\text{bkg}}, b^{\text{bkg}}) = \tilde{p}(\phi, p_\gamma | \Sigma^{\text{bkg}}, a^{\text{bkg}}, b^{\text{bkg}}). \quad (4.24)$$

If there are n prompt peak and m sideband events, the joint likelihood of all events \mathcal{L} is thus given by

$$\mathcal{L} = \prod_{i=1}^n p_{\text{prompt}}(\phi_i, p_{\gamma,i} | \Sigma, a, b, \Sigma^{\text{bkg}}, a^{\text{bkg}}, b^{\text{bkg}}) \prod_{j=1}^m p_{\text{sideband}}(\phi_j, p_{\gamma,j} | \Sigma^{\text{bkg}}, a^{\text{bkg}}, b^{\text{bkg}}), \quad (4.25)$$

or, equivalently

$$\begin{aligned} \ln \mathcal{L} &= \sum_{i=1}^n \ln p_{\text{prompt}}(\phi_i, p_{\gamma,i} | \Sigma, a, b, \Sigma^{\text{bkg}}, a^{\text{bkg}}, b^{\text{bkg}}) \\ &\quad + \sum_{j=1}^m \ln p_{\text{sideband}}(\phi_j, p_{\gamma,j} | \Sigma^{\text{bkg}}, a^{\text{bkg}}, b^{\text{bkg}}). \end{aligned} \quad (4.26)$$

Eighteen⁶ parameters have to be determined in total, either via a conventional frequentist approach or

⁶ The FOURIER series is constructed such that $a_0 = 0, b_0 = 1$

a BAYESIAN approach to this non-linear fitting problem.

Frequentist

Best fit estimates can be derived by maximizing the likelihood \mathcal{L} , or, for computational convenience, by minimizing $-\ln \mathcal{L}$. The *ROOT* library [BR97] offers the method *TTree::UnbinnedFit* to perform an unbinned maximum likelihood fit on data filled in a *TTree* [ROOb], which was used to perform the fit. Minimization and statistical error calculation are performed by *MINUIT* [JR75]. Errors are hereby estimated either symmetrical from the paraboloid shape of $(-\ln \mathcal{L})$ using the *HESSE* algorithm or asymmetric from the half-maximum values of $(-\ln \mathcal{L})$ using the *MINOS* algorithm without making assumptions on the shape of the likelihood, if necessary [JR75].

Bayesian

The joint posterior of all fit parameters given the data ϕ, p_γ is

$$p(\Sigma, a, b, \Sigma^{\text{bkg}}, a^{\text{bkg}}, b^{\text{bkg}} | \phi, p_\gamma) \propto \mathcal{L}(\phi, p_\gamma | \Sigma, a, b, \Sigma^{\text{bkg}}, a^{\text{bkg}}, b^{\text{bkg}}) \cdot \pi(\Sigma, a, b, \Sigma^{\text{bkg}}, a^{\text{bkg}}, b^{\text{bkg}}), \quad (4.27)$$

where $\pi(\theta)$ denotes the combined prior of all fit parameters which factors into each individual prior since all parameters are independent:

$$\pi(\Sigma, a, b, \Sigma^{\text{bkg}}, a^{\text{bkg}}, b^{\text{bkg}}) = \pi(\Sigma) \cdot \pi(a) \cdot \pi(b) \cdot \pi(\Sigma^{\text{bkg}}) \cdot \pi(a^{\text{bkg}}) \cdot \pi(b^{\text{bkg}}). \quad (4.28)$$

The priors for $\Xi \in \{\Sigma, \Sigma^{\text{bkg}}\}$ and $\xi \in \{a, b, a^{\text{bkg}}, b^{\text{bkg}}\}$ are again chosen non-informative, broadly centered around 0

$$\Xi \sim \mathcal{N}(0, 1)_{[-1, 1]} \quad \xi_k \sim \mathcal{N}(0, 0.1). \quad (4.29)$$

From references [Afz19; Har17] it is expected that $\xi_k \ll 1$, therefore the chosen widths of the priors resemble a, relatively speaking, broad distribution.

This model, consisting of the likelihood in Eq. (4.26) and the priors in Eq. (4.29), is implemented in Stan [Sta22], so that samples from the posterior in the physically allowed region ($\Xi \in [-1, 1]$) are again obtained via NUTS [HG14].

4.2 Determination of Σ_η using Bayesian statistics

This section will now demonstrate the application of the discussed methods to obtain the beam asymmetry Σ for η photoproduction with selected data provided from reference [Afz19]. For each method only the respective BAYESIAN approach will be used and compared to the results from [Afz19] to confirm that it is a valid method. As an additional sanity check toy Monte Carlo samples are generated and analyzed.

4.2.1 Application of methods to toy Monte Carlo data

Although results can be compared to the already accomplished ones in reference [Afz19], verifying the correct functioning of the fitting methods is still useful. This is done by generating events that follow the expected distributions of $N^{\parallel/\perp}$ with fixed and known parameters. With the simulated event yields the binned and unbinned fit are performed as described previously. Repeating this for a large number of times should reproduce the input parameters if the methods work as intended.

Event yield asymmetries

The asymmetry $A(\phi)$ is built from the event yields $N^{\parallel/\perp}$, which are distributed according to

$$N^{\parallel} = N_0 \left[1 - p_{\gamma}^{\parallel} \Sigma \cos(2(\alpha^{\parallel} - \phi)) \right], \quad (4.30)$$

$$N^{\perp} = N_0 \left[1 - p_{\gamma}^{\perp} \Sigma \cos(2(\alpha^{\perp} - \phi)) \right], \quad (4.31)$$

where the parameters are chosen as $\Sigma = 0.3$, $p_{\gamma}^{\parallel} = 0.25$, $p_{\gamma}^{\perp} = 0.3$. In each toy Monte Carlo bin the number of generated samples per setting $N_{\text{total}}^{\parallel/\perp}$ is given by a Poisson distribution

$$N_{\text{total}}^{\parallel} \sim \mathcal{P}(800) \quad N_{\text{total}}^{\perp} \sim \mathcal{P}(1000), \quad (4.32)$$

to simulate the statistics of the $\gamma p \rightarrow p\eta$ final state as accurately as possible [Afz19]. The samples from the distributions (4.30),(4.31) are drawn using the *TH1::GetRandom* [ROOc] function provided by *ROOT* [BR97]. The function from which samples should be drawn is integrated point wise and then normalized. The normalized integral is approximated by a parabola for each bin. A random number between 0 and 1 is generated and assigned to the according bin, where the respective parabola is evaluated to give the desired random value. [ROOc]. In total, 10000 toy Monte Carlo bins were simulated and the asymmetry built for 12 bins in ϕ , to conform with the binning chosen in reference [Afz19]. The resulting asymmetry $A(\phi)$ is shown in Figure 4.2 for several bins as the orange data points with statistical errors according to GAUSSIAN error propagation. Additionally shown is a χ^2 fit (orange line) to the asymmetry together with posterior predictive checks as obtained from a fully BAYESIAN fit according to the introduced model (blue distributions). This BAYESIAN fit was performed employing $n_{\text{chain}} = 4$ MARKOV chains with $n_{\text{samples}} = 1000$ samples each. The warm-up period for each chain has the same length of $n_{\text{warm up}} = 1000$

$$n_{\text{chain}} = 4 \quad n_{\text{samples}} = 1000 \quad n_{\text{warm up}} = 1000. \quad (4.33)$$

The goodness of fit is checked via the introduced p -values $p = T(A_{\text{rep}} > A)$, and are shown as black points with propagated error bars on the bottom. The optimal value of $p = 0.5$ is marked by the dashed line and realizes the mean of the distribution of all p -values, so that one can assume good description of the data by the fits, see Figure 4.3. This replaces the investigation of the χ^2/NDF distribution in the case of a frequentist fit, which should have a mean of 1.

4.2 Determination of Σ_η using Bayesian statistics

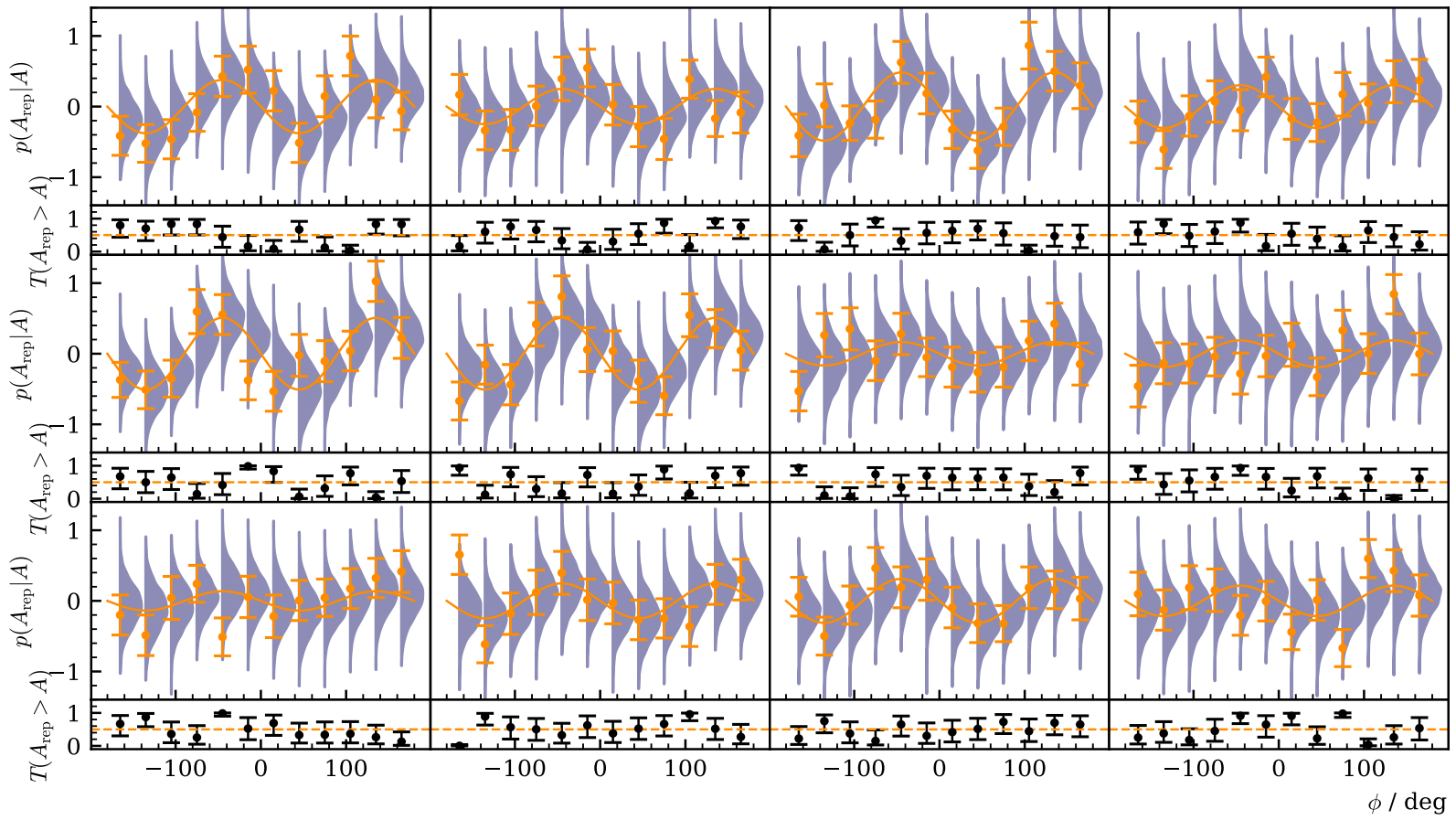


Figure 4.2: Posterior predictive checks $p(A_{\text{rep}}|A)$ from a BAYESIAN fit to the event yield asymmetries for six toy Monte Carlo bins are shown as distributions. The data points in the upper plot are the asymmetry $A(\phi)$, which was additionally fitted using a χ^2 fit (solid line). The goodness of fit is shown using p -values, which give the fraction $T(A_{\text{rep}} > A)$ of replicated samples greater than the original measured value, with propagated statistical error bars on the bottom of each plot. The expected mean value of $T(A_{\text{rep}} > A) = 0.5$ is indicated by the dashed line.

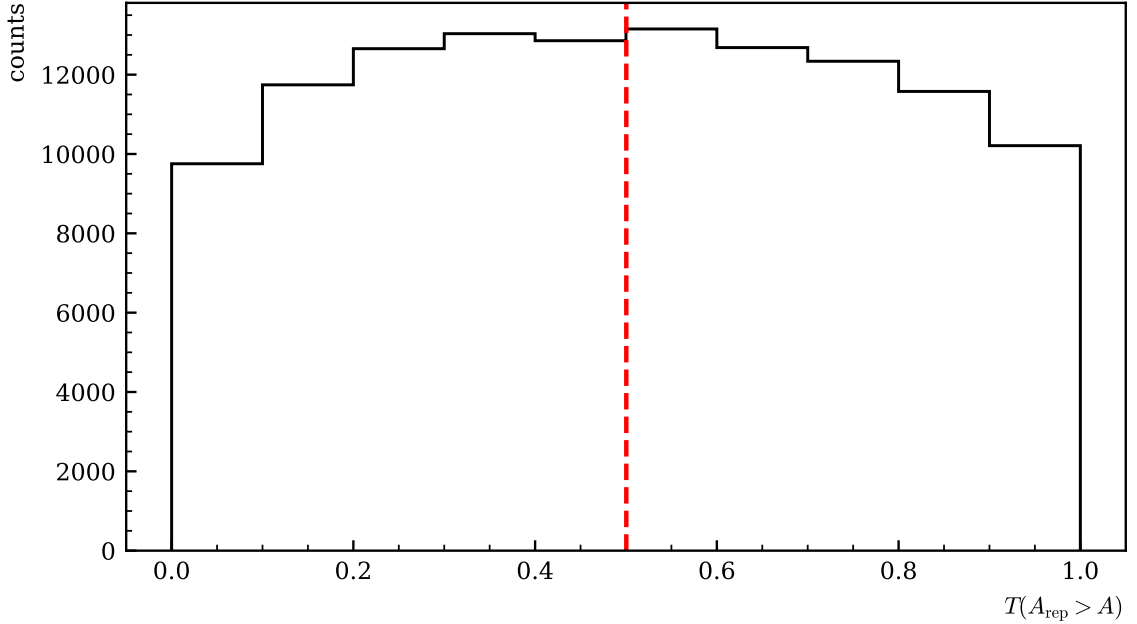


Figure 4.3: p values of all toy Monte Carlo bins. They are centered around their mean at 0.5, which is indicated by the dashed line, and show no bias towards higher or lower values, thus confirming an adequate fit.

To check whether the fit is unbiased and provides correct error estimation one can investigate the normalized residuals

$$\xi = \frac{\Sigma^{\text{fit}} - \Sigma^{\text{true}}}{\Delta\Sigma^{\text{fit}}} \quad (4.34)$$

in the case of a least-squares fit. Here Σ^{fit} and $\Delta\Sigma^{\text{fit}}$ are the value and corresponding statistical error for the beam asymmetry as obtained from the fit and Σ^{true} is the true value that was used to throw the toy MC experiments. An unbiased fit with right estimation of errors yields [Bar89]

$$\xi \sim \mathcal{N}(0, 1). \quad (4.35)$$

This criterion obviously cannot be applied in the same way to a BAYESIAN fit. The fit results are distributions and therefore lack point estimates Σ^{fit} and errors $\Delta\Sigma^{\text{fit}}$. However, one can modify Equation (4.34) to the needs of a BAYESIAN fit to assess its performance:

$$\Xi = \frac{\text{median}(\{\Sigma^{\text{fit}}\}) - \Sigma^{\text{true}}}{\text{std}(\{\Sigma^{\text{fit}}\})} \sim \mathcal{N}(0, 1). \quad (4.36)$$

Instead of the point estimates Σ^{fit} the median of the set of all draws from the marginal posteriors $\{\Sigma^{\text{fit}}\}$ is shifted by the true value Σ^{true} and normalized by the standard deviation as an error estimate for each fit. Although this is not a rigorously derived quantity it allows to identify possible bias if $\text{mean}(\Xi) \neq 0$. Furthermore, checking that $\sigma \approx 1$ will affirm whether the width of the marginal

posterior distributions is sensible. Figure 4.4 shows the combined Ξ -distributions of all fits and the unaltered combined posteriors shifted by the true value. As expected, both distributions are normal as a GAUSSIAN fit proves. The width of the marginal posterior distributions can be regarded as sensible

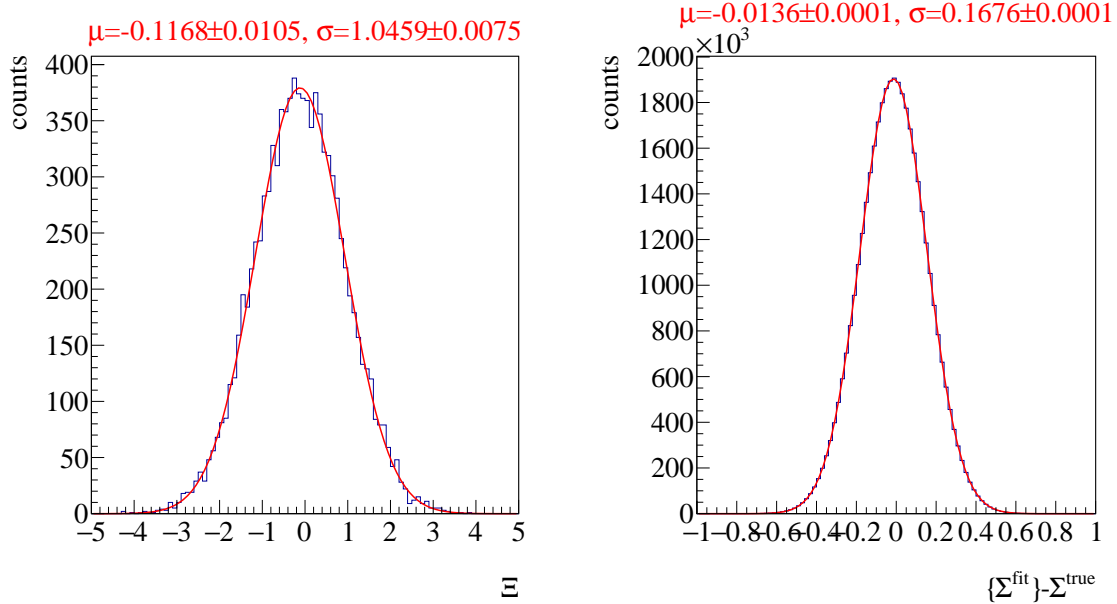


Figure 4.4: Left: Combined posterior distributions of all 10000 fits normalized by their respective standard deviation. Right: Unaltered combined posterior distributions of all 10000 fits. A GAUSSIAN fit was performed to determine mean μ and standard deviation σ of the distributions with results given on top.

since the standard deviation of the Ξ distribution $\sigma_\Xi \approx 1^7$. This is furthermore confirmed by the fact that $\{\Sigma^{\text{fit}}\} - \Sigma^{\text{true}} = 0$ within one standard deviation. Yet, the fit results tend to underestimate the beam asymmetry, because both distributions are centered out of their statistical error at $\mu \pm \Delta\mu < 0$. This indicates bias towards smaller values of the beam asymmetry. Remarkably, this bias is *not* introduced by the BAYESIAN fit, but by the choice of binning and available statistics as an extensive investigation of binned fits (least squares and BAYESIAN) to toy Monte Carlo data showed. A detailed discussion thereof is given in appendix B. For now it suffices to note the origin of this bias lies in the choice of binning and is thus inevitable. And, most importantly, the introduced bias is negligible compared to the width of the posterior distributions, so that a binned fit will produce valid fit results in any case. Nevertheless this emphasizes the advantage of unbinned fitting, which is discussed in the next paragraph.

It has been established that the fit produces valid results with sensible statistical errors, i.e. widths of posterior distributions, and the description of the data is in agreement with the expectations. It remains to diagnose the convergence of the MARKOV chains to finally deem the binned fit method appropriate. For this the \hat{R} value and the relative Monte Carlo standard error (MCSE) $\frac{\sigma_{\text{MCSE}}}{\text{median}[\rho(\Sigma|y)]}$ that were introduced in section 1.3 are investigated. If $\hat{R} < 1.05$ one can assume that the different chains have converged and explored the same parameter space [Veh+19]. Furthermore the accuracy

⁷ One cannot expect to fulfill Eq. (4.35) exactly, since the errors are after all only estimates that aim to create comparability to the least squares fit.

supplied by the number of draws from the posteriors can be evaluated with the relative MCSE. It is demanded that $\frac{\sigma_{\text{MCSE}}}{\text{median}[P(\Sigma|y)]} \lesssim 5\%$. This is the case for 97% of all fits, see Figure 4.5 on the left. When the fit result for the beam asymmetry is close to 0 larger values for the relative MCSE are observed. The \hat{R} values (Figure 4.5 on the right) clearly indicate good within and between chain convergence. This means that the hyper parameters n_{chain} , n_{samples} and $n_{\text{warm up}}$ as chosen are well tuned, although one may increase the number of sample draws from the posterior for the fit from measured data to further suppress the relative MCSE. Then, only $11 \cdot 12$ as opposed to 10000 fits have to be performed keeping the computational cost reasonable.

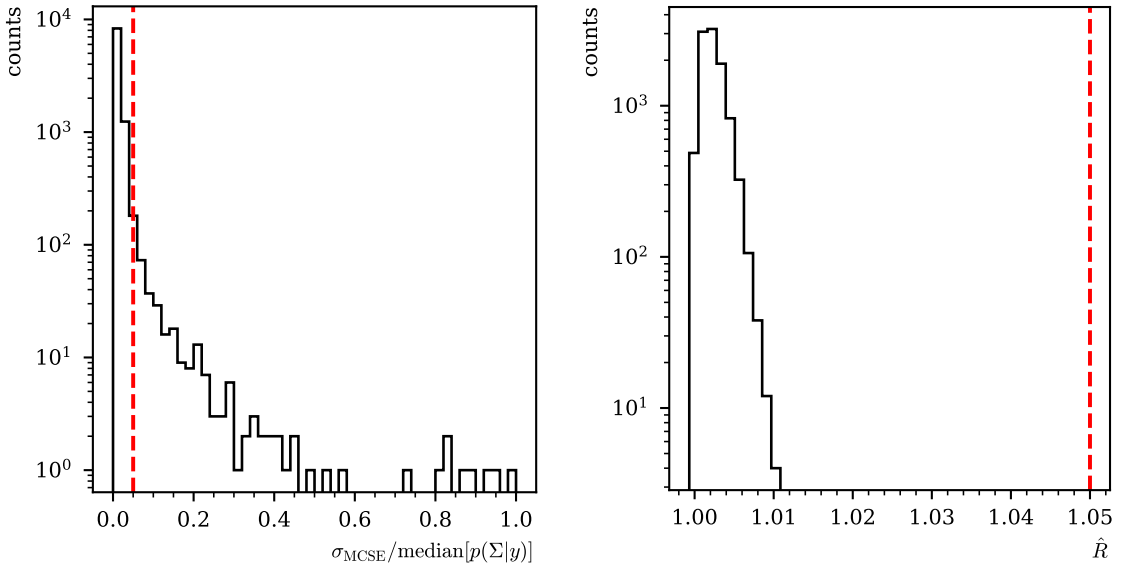


Figure 4.5: Left: relative error $\frac{\sigma_{\text{MCSE}}}{\text{median}[P(\Sigma|y)]}$ Right: \hat{R} associated with the fit parameter Σ . Both are shown for all 10000 fits. The critical values that should not be exceeded are marked by dashed lines.

Event based fit

Not only signal events but also contributions from random time background as well as the imperfect detector efficiency $\epsilon(\phi)$ have to be simulated in order to test the method of event based fitting. For each polarization setting prompt peak and sideband events are drawn from the theoretical ϕ -distributions p_{prompt} and p_{sideband} which are given in Equations (4.23) and (4.24). The total number of draws per setting and bin is again given by Poisson distributions and the ratio of prompt peak to sideband events is given by the time cut weights $\{w_i\}_{i=1}^7$ employed for the actual analysis of the $p\eta$ final state data [Afz19]. This means that seven times prompt peak and sideband events need to be simulated. The fraction of background events within the prompt peak f was set to $f = 0.95$. Further, the values $p_\gamma^\parallel = 0.25$, $p_\gamma^\perp = 0.3$, $\Sigma = 0.5$, $\Sigma^{\text{bkg}} = -0.5$ and lastly, a random efficiency function as already chosen in reference [Afz19] were appointed. Finally the hyperparameters n_{chain} , n_{samples} , $n_{\text{warm up}}$ are chosen the same as previously. Table 4.1 shows a summary of all toy Monte Carlo properties. In total, 1000 toy Monte Carlo experiments are thrown. To evaluate the fit results only the posterior distributions are available. As before, the residuals Ξ are built from all fits, now for Σ as well as Σ^{bkg} . They are

chosen parameters	$p_\gamma^{\parallel} = 0.25, p_\gamma^{\perp} = 0.3, \Sigma = 0.5, \Sigma^{\text{bkg}} = -0.5, f = 0.95,$ $w_1 = \frac{15}{210}, w_2 = \frac{8}{210}, w_3 = \frac{4}{210}, w_4 = \frac{10}{210}, w_5 = \frac{14}{210}, w_6 = \frac{6}{210}, w_7 = \frac{11}{210}$
simulation draws	$7 \cdot N_{\text{total},i}^{\parallel} \sim \mathcal{P}(800), 7 \cdot N_{\text{total},i}^{\perp} \sim \mathcal{P}(1000) \quad _{i=1}^7$
	signal in prompt background in prompt sideband $N_{\text{total}}^{\parallel/\perp} \cdot f \quad N_{\text{total}}^{\parallel/\perp} \cdot (1-f) \quad N_{\text{total}}^{\parallel/\perp} \cdot (1-f) \cdot 1/w_i$
efficiency function	$\epsilon(\phi) = 1/10.5 \cdot (9.3 + 0.28 \cdot \cos \phi + 0.24 \cdot \sin 3\phi)$
hyperparameters	$n_{\text{samples}} = 1000, n_{\text{chain}} = 4, n_{\text{warm up}} = 1000$

Table 4.1: Summary of the complete setting of all toy Monte Carlo experiments for the event based fit. Values and table layout adapted from [Afz19].

shown in Figure 4.6 together with the unnormalized posterior distributions. Note that the distributions are truncated towards the tails at $\Sigma \rightarrow 1$ and $\Sigma^{\text{bkg}} \rightarrow -1$ as implemented in the BAYESIAN fit in Stan. Also the event based fit is able to reproduce the true values within one standard deviation of the posterior distribution $\sigma_{\text{posterior}}$. Only slight bias towards smaller values of the signal beam asymmetry is seen, but again with negligible effect on the results in comparison to the widths of the distributions. Additionally, the mean of the distributions are 0 within 3σ of their statistical error and the errors are estimated correctly, since $\sigma_{\text{posterior}} = 1$ within the statistical error. Note that the background beam asymmetry is estimated closer to its true value than the signal beam asymmetry because there are more random background events than signal events.

If the total amount of posterior distributions is not too large one might also combine them in a *pooled likelihood* approach (see subsection 1.3.3). This is shown in Figure 4.7 for both determined asymmetries. Because the true asymmetries are within 1σ of the resulting distribution one can finally conclude that the event based fit estimates positions and widths of the posterior distributions correctly.

A check of the relative MCSE and \widehat{R} values as shown in Figure 4.8 reveals also that the hyperparameters $n_{\text{chain}}, n_{\text{samples}}, n_{\text{warm up}}$ are correctly tuned. It is noteworthy that the event based fit creates more precise results although less Monte Carlo experiments in total were performed than for the binned fit.

Next to signal and background beam asymmetry the fit also estimates an efficiency function $\epsilon(\phi)$ that is described by a FOURIER series. The polarization weighted sum of event yields allows to confirm whether a good description of the efficiency is achieved because it is given by the efficiency function modulated only by a constant, see previous section 4.1 $\alpha \tilde{N}^{\parallel} + \beta \tilde{N}^{\perp} = c \cdot \epsilon(\phi)$. Figure 4.9 shows the weighted sum of event yields with the same binning as used in the binned fit together with a posterior predictive check using the draws of all parameters distributions a, b . As opposed to the binned fit it is not only performed at each data point but for significantly more points. This mimics a continuous function as is appropriate for an unbinned fit. However, for better visibility the posterior predictive distributions are not built at every point but the efficiency function is plotted for each set of draws $a^{(s)}, b^{(s)}, s = 1 \dots 4000$. No p values are estimated since they would not be representative of the whole fit. The mean of the posterior predictive distributions is given by the dashed line and agrees within statistical error bars with the simulated data.

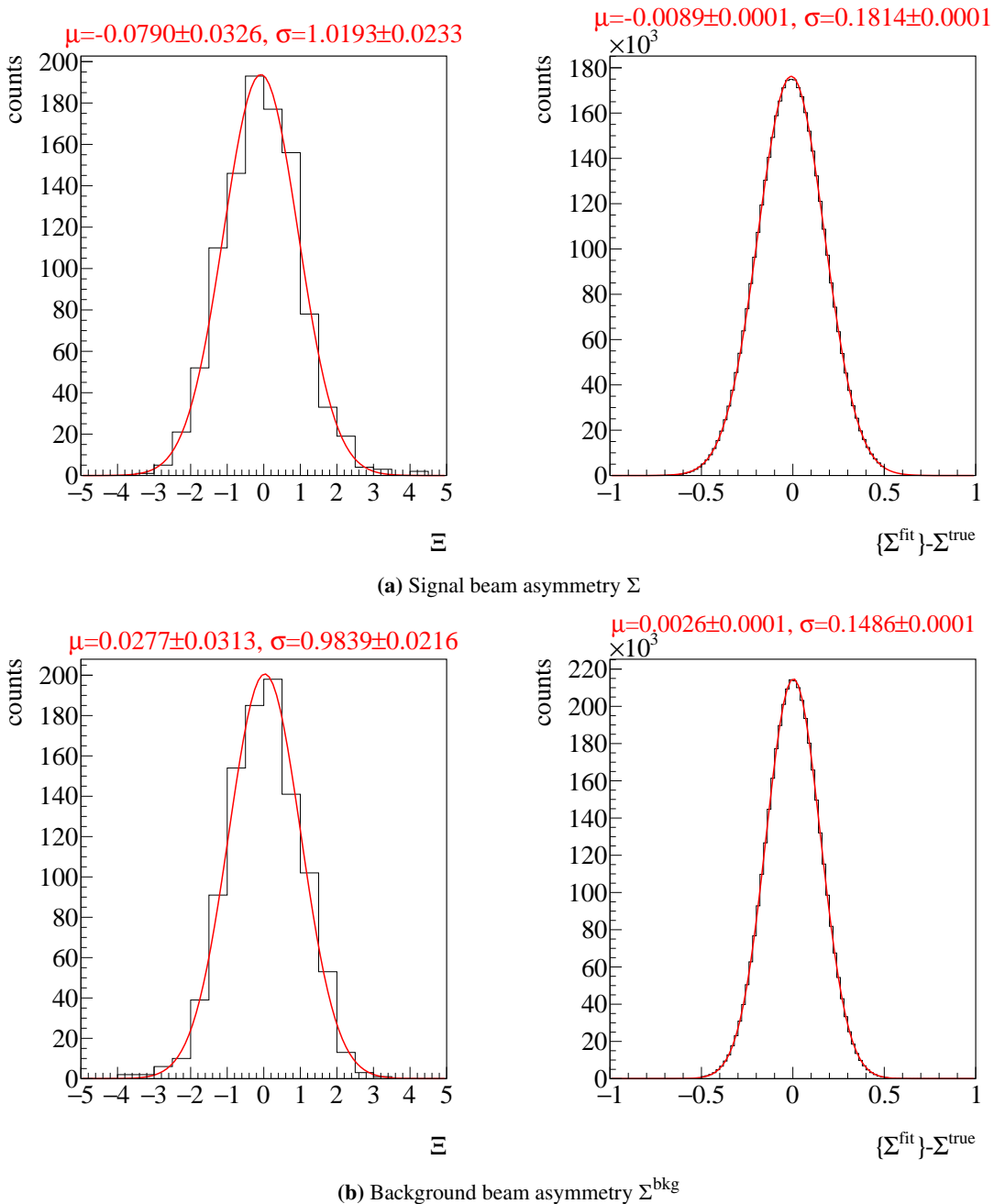


Figure 4.6: Combined posteriors for the beam asymmetries Σ and Σ^{bkg} from all 1000 event based fits. Left: Residuals Ξ Right: Unnormalized posterior distributions. A GAUSSIAN fit is performed on the distributions with results for mean μ and standard deviation σ on top.

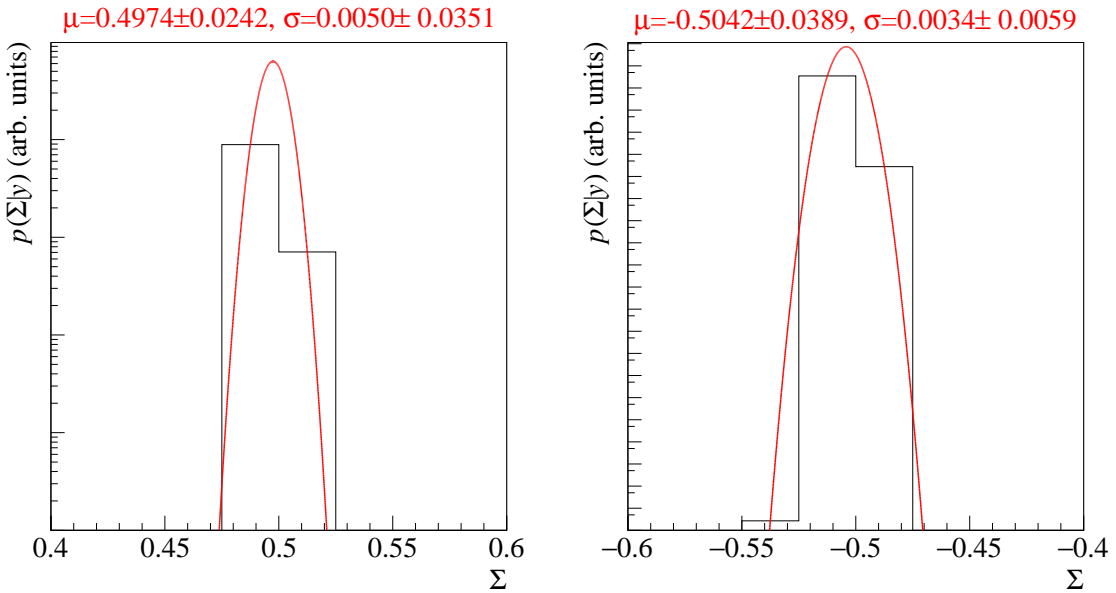


Figure 4.7: Combined posterior probabilities using the *pooled likelihood* approach. Left: Signal beam asymmetry, Right: background beam asymmetry. Mean and standard deviation as obtained from a Gaussian fit are shown on top

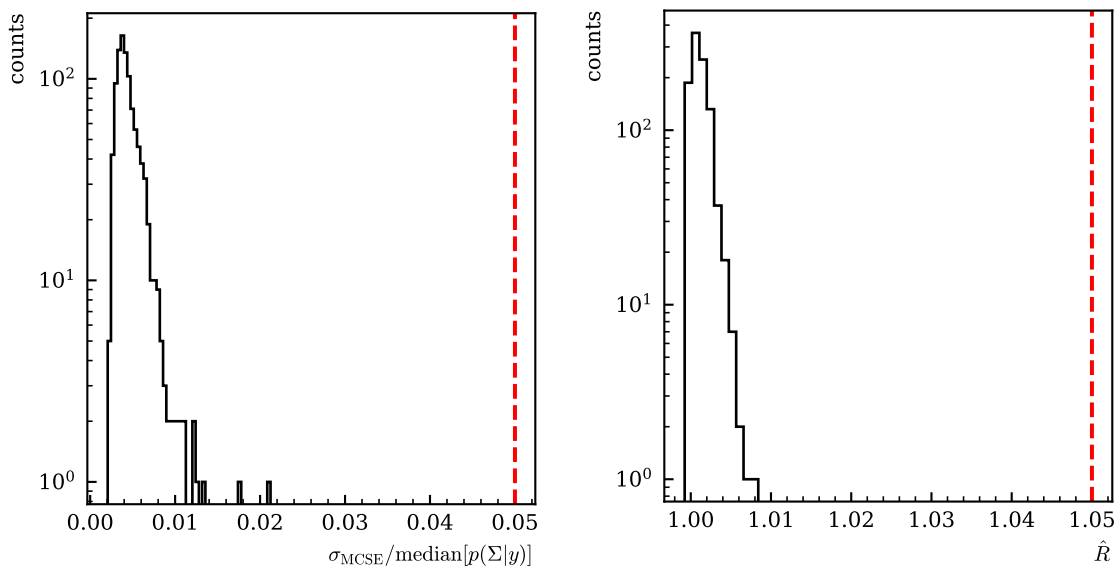


Figure 4.8: Left: relative error $\frac{\sigma_{\text{MCE}}}{\text{median}[p(\Sigma|y)]}$. Right: \hat{R} associated with the fit parameter Σ . Both are shown for all 1000 fits. The critical values that should not be exceeded are marked by dashed lines.

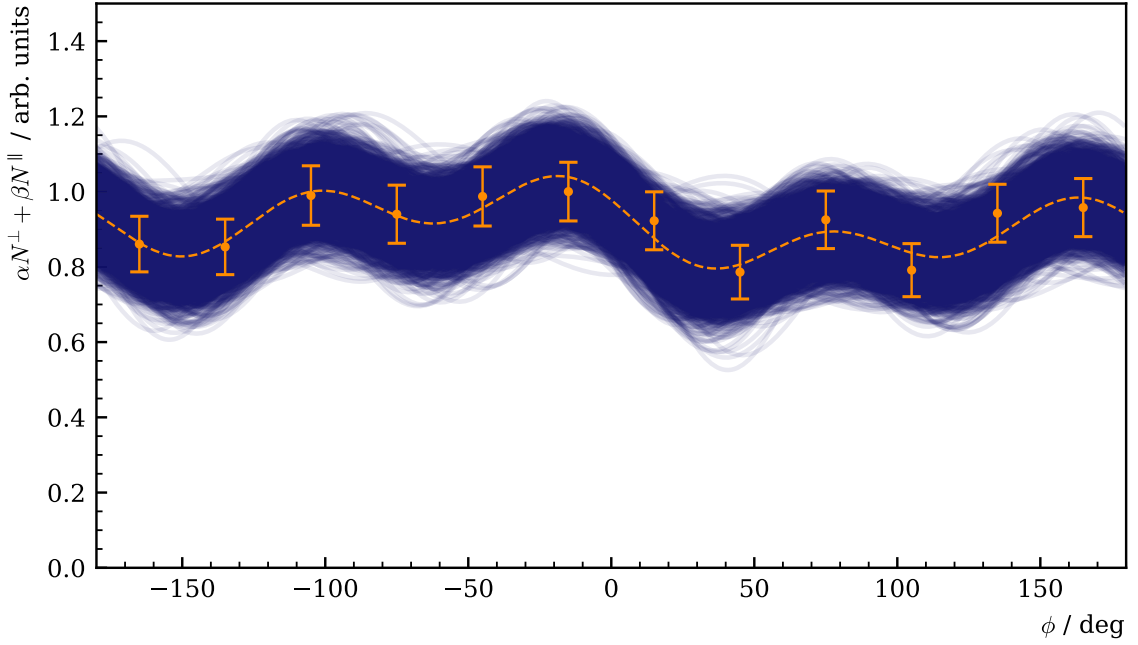


Figure 4.9: Posterior predictive check using the draws of the detector coefficients a and b . Points with error bars are the polarization weighted sum of event yields. The dashed line is the mean of the predictive values while the solid opaque lines are representative of one simulation draw $a^{(s)}, b^{(s)}$.

4.2.2 Application of methods to data

Since both methods were tested successfully using toy Monte Carlo data, both are subsequently applied to real data to extract the beam asymmetry. Since the number of fits is small compared to the amount of fits performed during testing, the amount of posterior draws was increased to 5000 per chain. All other hyperparameters were left the same

$$n_{\text{samples}} = 5000 \quad n_{\text{chain}} = 4 \quad n_{\text{warm up}} = 1000. \quad (4.37)$$

Event yield asymmetries

In all bins of beam energy and meson polar angle the binned fit was performed. Similar to the Monte Carlo samples, 12 bins in phi are built to comply with the binning in reference [Afz19], and guarantee comparability.

Figure 4.10 shows the resulting asymmetry $A(\phi)$ for all angular bins for the energy bin $1250 \text{ MeV} \leq E_\gamma < 1310 \text{ MeV}$ as orange data points with statistical error bars. Additionally shown is a χ^2 fit (orange line) to the asymmetry together with posterior predictive checks as obtained from a fully BAYESIAN fit according to the introduced model (blue distributions). The goodness of fit is checked via the introduced p -values $p = T(A_{\text{rep}} > A)$, and are shown as black points with propagated error bars on the bottom. The optimal value of $p = 0.5$ is marked by the dashed line and realizes the mean of the distribution of all p -values, so that one can assume good description of the data by the fits, see Figure 4.11. This replaces the investigation of the χ^2/NDF distribution in the case of a frequentist fit.

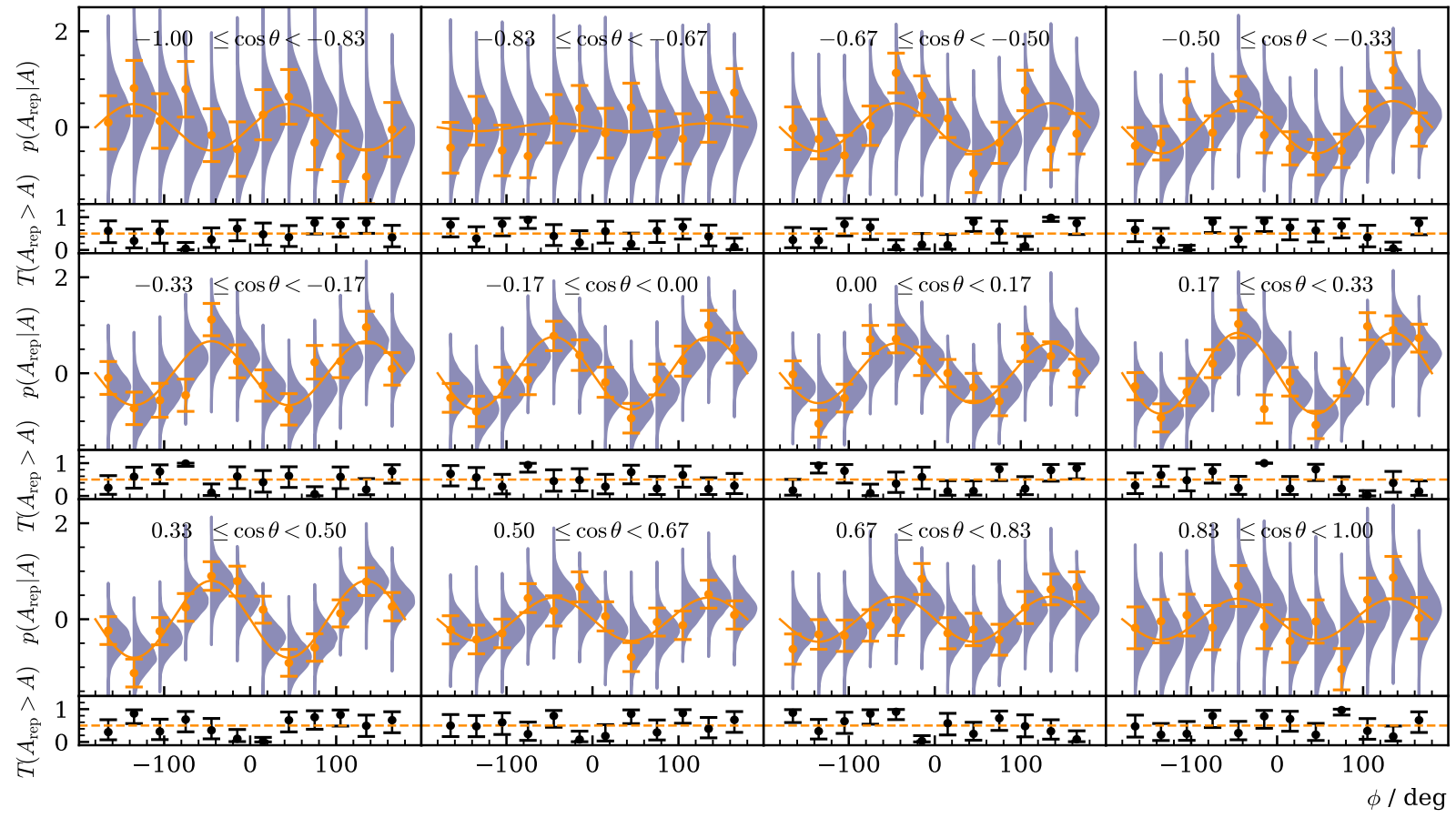


Figure 4.10: Posterior predictive checks $p(A_{\text{rep}}|A)$ from a BAYESIAN fit to the event yield asymmetries for all angular bins of the energy bin $1250 \text{ MeV} \leq E_\gamma < 1310 \text{ MeV}$. The data points in the upper plot are the asymmetry $A(\phi)$, which was additionally fitted using a χ^2 fit (solid line). The goodness of fit is shown using p -values, which give the fraction $T(A_{\text{rep}} > A)$ of replicated samples greater than the original measured value, with propagated statistical error bars on the bottom of each plot. The expected mean value of $T(A_{\text{rep}} > A) = 0.5$ is indicated by the dashed line.

4.2 Determination of Σ_η using Bayesian statistics

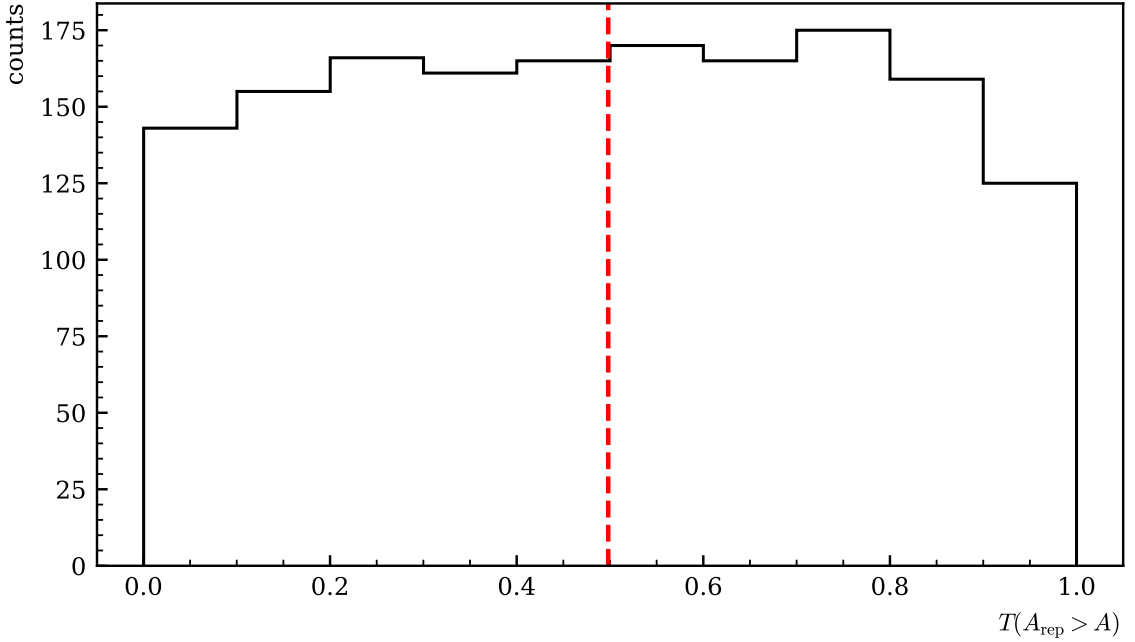


Figure 4.11: p values generated using all fits. They are centered around their mean at 0.5, which is indicated by the dashed line, and show no bias towards higher or lower values, thus confirming an adequate fit.

The MCMC diagnostics reveal that all MARKOV chains have converged and explored the available parameter space completely which is characterized by $\widehat{R} = 1.00$ for all fits. The increment of posterior draws removed any fluctuations in the \widehat{R} value that was present before. The relative MCSE is below the (self-)defined threshold of $\frac{\sigma_{\text{MCSE}}}{\text{median}[P(\Sigma|y)]} < 5\%$ for 95% of all fits. The remaining 5% are fits that estimated the beam asymmetry close to 0 such that further incrementing the number of posterior draws will not amend this. Both, relative MCSE and \widehat{R} associated with the fit parameter Σ of the binned fit, are shown in Figure 4.12. Thus, one can conclude the successful tuning of hyperparameters concerning the BAYESIAN fit.

Event based fit

The discussed BAYESIAN event based fit is also performed for all kinematic bins. The MCMC diagnostics reveal good choice of hyperparameters, as Figure 4.13 shows. As already observed during the toy Monte Carlo experiments, the unbinned fit produces more precise results; 98% of all fits exhibit an MCSE below threshold, those bins with error above threshold are again explained by values of the beam asymmetry $\Sigma \approx 0$. Good within and between chain convergence is reached, as $\widehat{R} = 1.00$ for all fits shows.

The only illustrative measure regarding the performance of the unbinned fit is the posterior predictive distribution of the detector coefficients a, b . Figure 4.14 shows the weighted sum of event yields with the same binning as used in the binned fit together with a posterior predictive check using the draws of all parameters distributions a, b for the kinematic bin $1250 \text{ MeV} \leq E_\gamma < 1310 \text{ MeV}, 0 \leq \cos \theta < 0.17$. As opposed to the binned fit it is not only performed at each data point but for significantly more points. This mimics a continuous function as is appropriate for an unbinned fit. However, for better

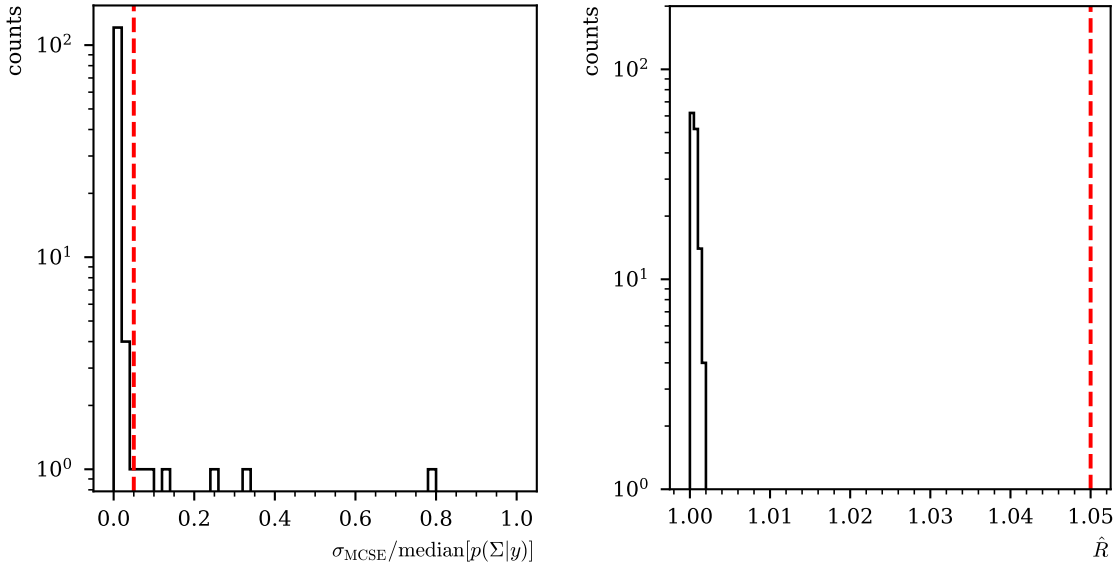


Figure 4.12: Left: relative error $\frac{\sigma_{\text{MCSE}}}{\text{median}[p(\Sigma|y)]}$ Right: \hat{R} associated with the fit parameter Σ . Both are shown for all $11 \cdot 12$ binned fits to the asymmetry $A(\phi)$. The critical values that should not be exceeded are marked by dashed lines.

visibility the posterior predictive distributions are not built at every point but the efficiency function is plotted for each set of draws $a^{(s)}, b^{(s)}, s = 1 \dots 20000$. No p values are estimated since they would not be representative of the whole fit. Note that the detector efficiency $\epsilon(\phi)$ is almost flat as opposed to the simulated efficiency in subsection 4.2.1. This is an overall observation and not specific to the shown kinematic bin and further confirmed by the fact that the sums of all fit coefficients a, b are distributed around zero. Regardless of the significance of detection inefficiencies the unbinned fit is nevertheless able to obtain good agreement between fit and data; the mean of all posterior predictive distributions (dashed line) agrees within statistical error bars with the data points.

4.2.3 Discussion

The final results for the beam asymmetry obtained with both methods are shown in Figure 4.15 for all bins in beam energy and meson polar angle. Along with the marginal posterior distributions obtained from both introduced methods point estimates from a χ^2 fit and an unbinned fit [Afz19] are shown. An important intermediate result is that all results agree with each other within statistical error bars or within the width of the marginal posterior distributions. Any effects that lead to slightly distinguishable point estimates from a binned or unbinned fit are propagated directly throughout the BAYESIAN fit; then each distribution is centered around the point estimate of the respective fitting method. The results from the binned and unbinned fit with error bars on average cover 68% of the respective marginal posterior distributions, corresponding to a 1σ interval. Thus, in general, the application of BAYESIAN methods has proven to give the same results and no systematic error is introduced by the BAYESIAN approach.

The effort of implementing the binned or unbinned fit in a BAYESIAN approach is comparable to

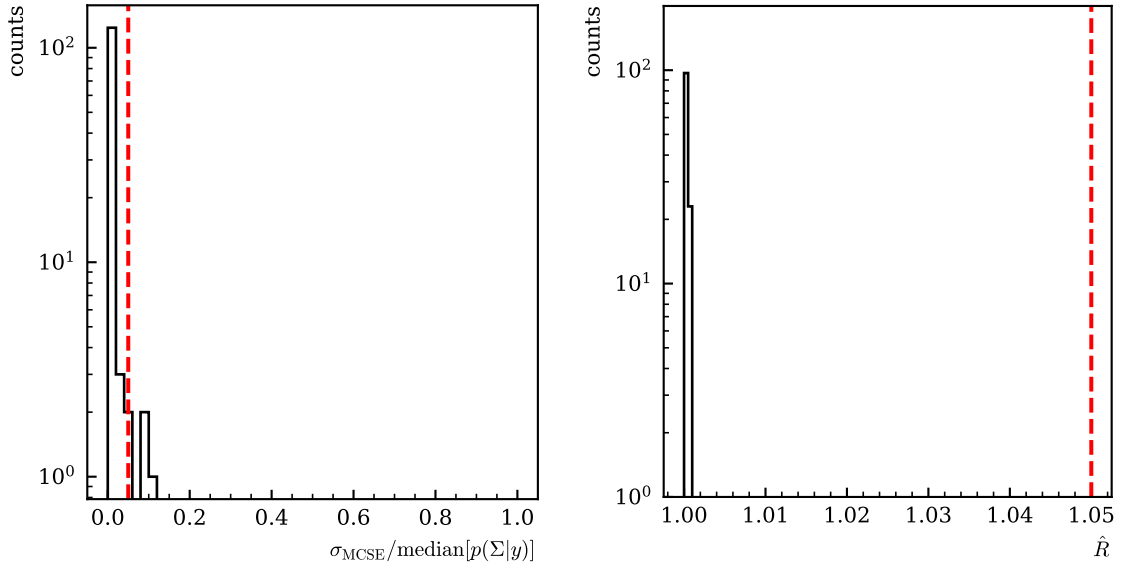


Figure 4.13: Left: relative error $\frac{\sigma_{\text{MCSE}}}{\text{median}[p(\Sigma|y)]}$. Right: \hat{R} associated with the fit parameter Σ . Both are shown for all $11 \cdot 12$ unbinned fits. The critical values that should not be exceeded are marked by dashed lines.

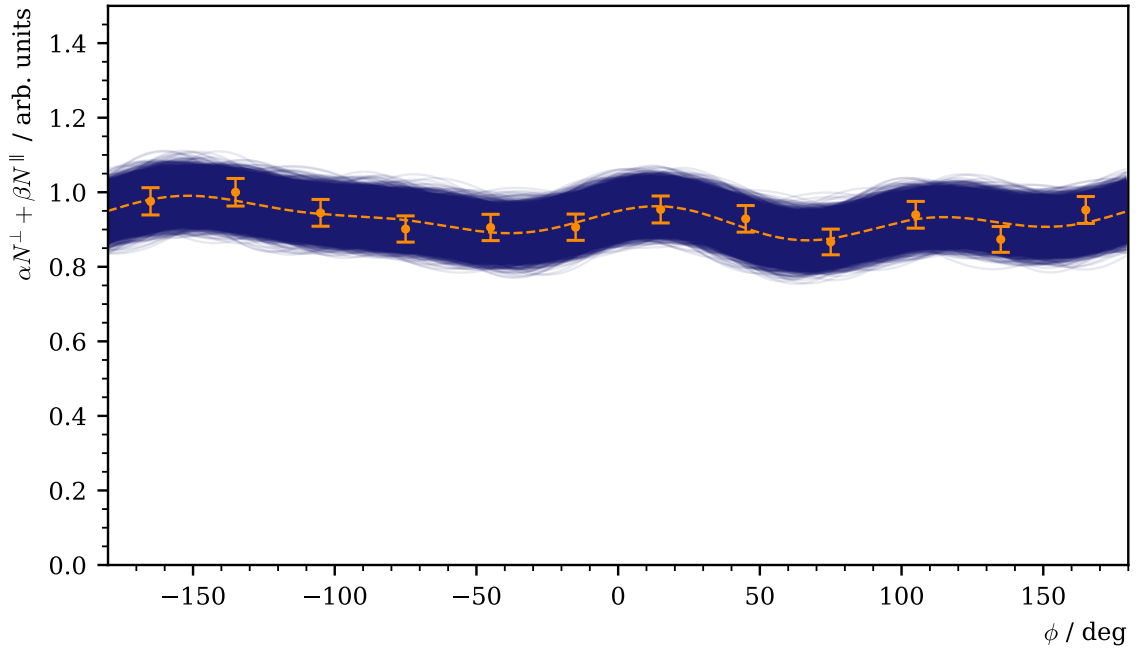


Figure 4.14: Posterior predictive check using the draws of the detector coefficients a and b for the kinematic bin $1250 \text{ MeV} \leq E_\gamma < 1310 \text{ MeV}, 0 \leq \cos \theta < 0.17$. Points with error bars are the polarization weighted sum of event yields. The dashed line is the mean of the predictive values while the solid opaque lines are representative of one simulation draw $a^{(s)}, b^{(s)}$.

using standard libraries provided by e.g. *python* [RP22] or *ROOT* [BR97]. Due to the probabilistic structure of the Stan language [Sta22] implementation of likelihood and prior models is straightforward and the sampling algorithms can be accessed or modified to ones needs intuitively. However, the BAYESIAN fit requires more careful preparation and also diagnostics. On one hand, the choice of priors has to be made. On the other hand, the fitting procedure is inherently different; not only the goodness of fit compared with data has to be checked but also the convergence of the MARKOV chains themselves.

The computational cost also increases greatly in comparison to the traditional frequentist approaches. Especially the unbinned BAYESIAN fit requires a lot of computation time, where the number of data points is of order $O(10^4)$ as opposed to 12 data points for the binned fit. This can be understood considering the underlying algorithms; the least squares fit and also the unbinned maximum likelihood fit both aim to minimize a given test statistic which is achievable by (numeric) differentiation. Determining marginal posterior distributions from BAYESIAN inference on the other hand requires (numeric) integration, making it the more complex task which is observable in the consumed computation time.

Yet, the additional effort is rewarded by the fact that the BAYESIAN fit will yield *distributions* for all parameters as opposed to point estimates with error bars. This is especially useful for polarization observables which may be used as input for PWA calculations. Here error estimates can be derived from the distributions e.g. as (multiple) standard deviations, the full width at half maximum or similar. If furthermore a BAYESIAN approach is pursued, also the whole distributions may be used. Another advantage of the BAYESIAN fit is the ability to truncate the posterior samples to the relevant or allowed parameter space. In the very first energy bin in Figure 4.15 this is visible clearly where several point estimates exceed the physical limit of $\Sigma = 1$ as opposed to the obtained marginal posteriors. Lastly, the BAYESIAN fit allows much more flexible changes to the fitted model, as will be discussed in the next section 4.3.

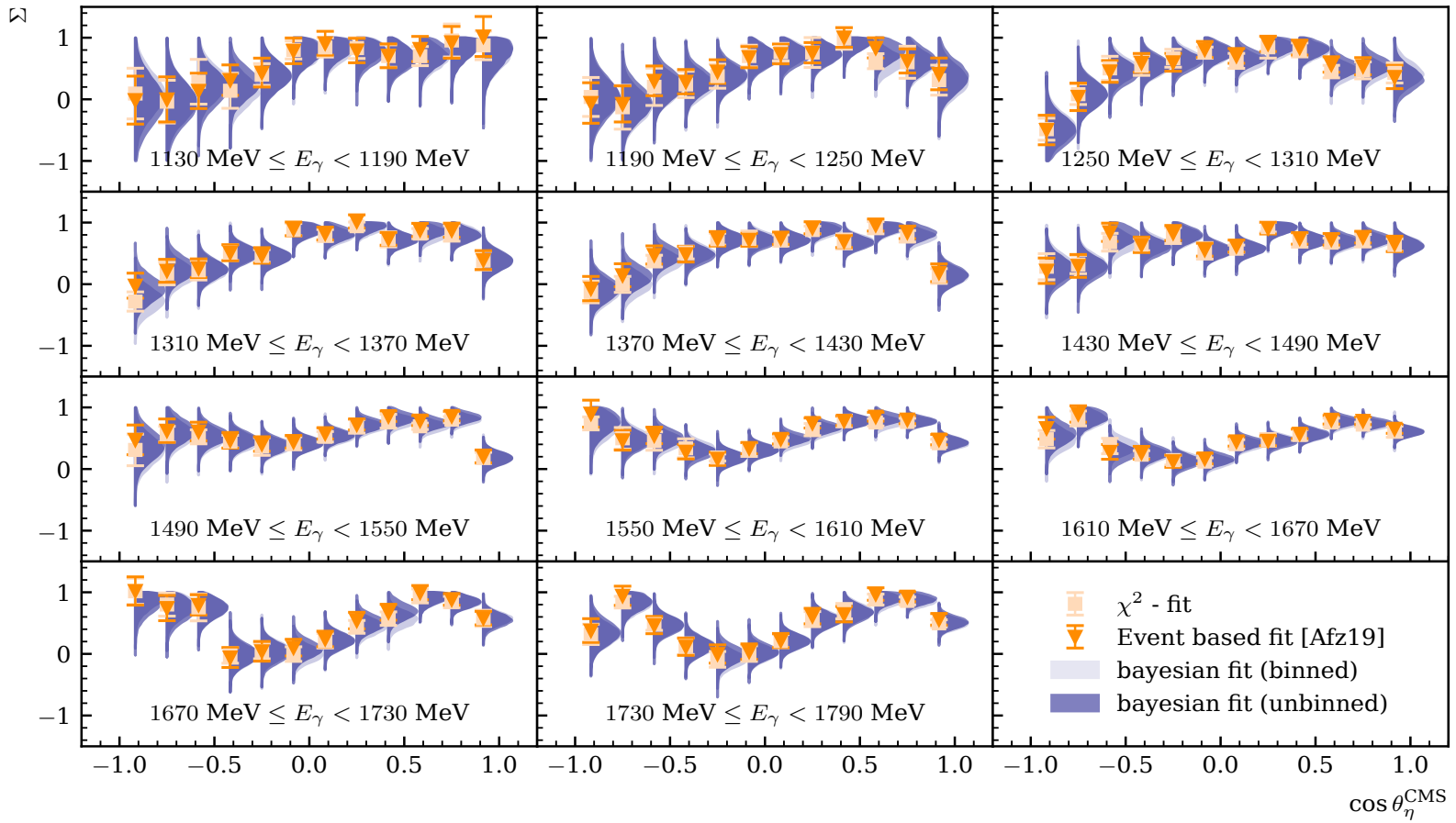


Figure 4.15: Final results for the beam asymmetry Σ in η photoproduction off the proton for all kinematic bins obtained with BAYESIAN methods. They are compared with the results of a least squares fit and an unbinned fit as given in reference [Afz19]. All results agree within statistical error bars or within the widths of marginal posterior distributions.

4.3 Determination of $\Sigma_{\eta'}$

After successfully testing the application of BAYESIAN methods this section will demonstrate the extraction of new results for the beam asymmetry in η' photoproduction off the proton obtained at the CBELSA/TAPS experiment. Only the event based fitting method is applied and the binned fitting of event yield asymmetries is discarded because on one hand the available statistics will on average give only few counts per bin $(E_\gamma, \cos \theta, \phi)$ of order $O(10^1)$, depending on the specific number of ϕ -bins. This will result in very large statistical errors per bin. On the other hand this could be compensated by choosing fewer bins in ϕ which would however amplify the systematic underestimation of the beam asymmetry which is discussed in appendix B.

The event based fits are performed as unbinned maximum likelihood fit and as BAYESIAN fit. New toy Monte Carlo experiments are thrown adapting to the significantly decreased statistics. Also, tests regarding the background contamination of Monte Carlo samples are made.

4.3.1 Application of event based fit to toy Monte Carlo data

After selecting all suitable event candidates for $\gamma p \rightarrow p\eta' \rightarrow p\gamma\gamma$ reactions there still remain significant background contributions which make up 18% of all events averaged over all kinematic bins. Investigation of Monte Carlo simulations of different mesonic final states revealed they are mainly realized by the false reconstruction of $2\pi^0$ photoproduction events (see chapter 3). It was thus investigated how the presence of two beam asymmetries Σ_1 and Σ_2 affects the fit. The combined differential cross section is then given by

$$\frac{d\sigma}{d\Omega_{\text{pol}}}(\phi) = \frac{d\sigma^{(1)}}{d\Omega_{\text{pol}}}(\phi) + \frac{d\sigma^{(2)}}{d\Omega_{\text{pol}}}(\phi) \quad (4.38)$$

$$= \frac{d\sigma^{(1)}}{d\Omega_0} \cdot (1 - p_\gamma \Sigma_1 \cos(2\phi)) + \frac{d\sigma^{(2)}}{d\Omega_0} \cdot (1 - p_\gamma \Sigma_2 \cos(2\phi)). \quad (4.39)$$

If now the fraction δ of events in the final state with beam asymmetry Σ_2 is known one can express the unpolarized cross sections via a common combined unpolarized cross section as

$$\frac{d\sigma^{(1)}}{d\Omega_0} = (1 - \delta) \cdot \frac{d\sigma}{d\Omega_0} \quad \frac{d\sigma^{(2)}}{d\Omega_0} = \delta \cdot \frac{d\sigma}{d\Omega_0}. \quad (4.40)$$

Plugging Equation (4.40) into Equation (4.39) then yields

$$\frac{d\sigma}{d\Omega_{\text{pol}}}(\phi) = \frac{d\sigma}{d\Omega_0} \cdot (1 - p_\gamma [(1 - \delta) \cdot \Sigma_1 + \delta \cdot \Sigma_2] \cos(2\phi)). \quad (4.41)$$

In the presence of background Σ^{bkg} ⁸ all measured values for the beam asymmetry Σ^{meas} are systematically shifted from their true value Σ^{true} , depending on the amount of background, if the methods described in section 4.1 are used without modification, i.e.

$$\Sigma^{\text{meas}} = (1 - \delta) \cdot \Sigma^{\text{true}} + \delta \cdot \Sigma^{\text{bkg}}. \quad (4.42)$$

⁸ For clarity, the beam asymmetry associated with random time background will in this section be denoted as Σ_t^{bkg} and the beam asymmetry associated with background reactions as Σ^{bkg}

Table 4.2 shows all characteristics of the investigated toy Monte Carlo experiments, the values for polarization and statistics per bin were chosen to match the respective average values in the selected data for the $\gamma p \rightarrow p\eta' \rightarrow p\gamma\gamma$ final state. Furthermore $\delta = 20\%$ of all events were simulated as background with beam asymmetry Σ_2 while the remainder of events is simulated with beam asymmetry Σ_1 . The amount of random time background in the prompt peak is set to $(1 - f) = 0.05$ while the sideband events are weighted by $w = \frac{13}{200}$ (see section 3.2). The same efficiency function and hyperparameters as previously are employed with the exception of the number of posterior draws which is raised to $n_{\text{samples}} = 5000$ from the beginning. Because of the smaller amount of data this does not increase the computational cost irrationally.

chosen parameters	$p_\gamma^{\parallel} = 0.3, p_\gamma^{\perp} = 0.3, \Sigma_1 = 0.5, \Sigma_2 = -0.3, \Sigma_t^{\text{bkg}} = -0.5, f = 0.95, \delta = 0.2$ $w = \frac{13}{200}$
simulation draws	$N_{\text{total}}^{\parallel} \sim \mathcal{P}(200), N_{\text{total}}^{\perp} \sim \mathcal{P}(200)$
	signal in prompt background in prompt sideband $N_{\text{total}}^{\parallel/\perp} \cdot f$ $N_{\text{total}}^{\parallel/\perp} \cdot (1 - f)$ $N_{\text{total}}^{\parallel/\perp} \cdot (1 - f) \cdot 1/w$
efficiency function	$\epsilon(\phi) = 1/10.5 \cdot (9.3 + 0.28 \cdot \cos \phi + 0.24 \cdot \sin 3\phi)$
hyperparameters	$n_{\text{samples}} = 5000, n_{\text{chain}} = 4, n_{\text{warm up}} = 1000$

Table 4.2: Summary of the complete setting of all toy Monte Carlo experiments for the event based fit. Table layout adapted from [Afz19].

Unbinned maximum likelihood fit

To test the unbinned maximum likelihood fit and its response to the presence of background, 10000 toy Monte Carlo bins are created according to table 4.2. The expected beam asymmetry is

$$\Sigma^{\text{meas}} = 0.8 \cdot 0.5 - 0.2 \cdot 0.3 = 0.34. \quad (4.43)$$

Building the normalized residuals with respect to Σ^{meas} and the random time background asymmetry Σ_t^{bkg} yields standard normal distributions, see Figures 4.16 and 4.17, thus fulfilling the expectations entirely. This allows Equation (4.42) to be applied on results obtained with this method provided the background beam asymmetry is known. Any errors on Σ^{bkg} may be propagated in a GAUSSIAN manner. The beam asymmetry is estimated without bias and the errors are correctly estimated as confirmed by $\mu = 0$ and $\sigma = 1$ for the normalized residuals within few widths of the statistical errors. Note that the unnormalized distributions are significantly broader than the ones examined in the previous section which is due to the decreased statistics in each bin which already indicates larger statistical errors. The decreased statistics also cause greater variation in the fitted efficiency function that is seen in Figure 4.18, which still describes the data very well.

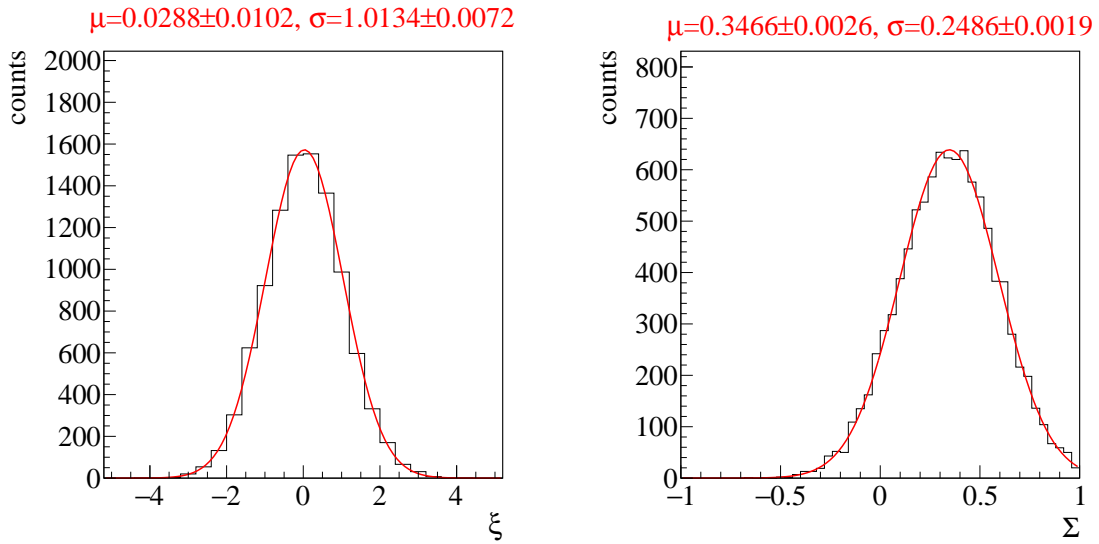


Figure 4.16: Normalized residuals (left) and unaltered distribution (right) of all 10000 fits for the beam asymmetry $\Sigma = (1 - \delta) \cdot \Sigma_1 + \delta \cdot \Sigma_2$. GAUSSIAN fits are performed with results given on top of each plot.

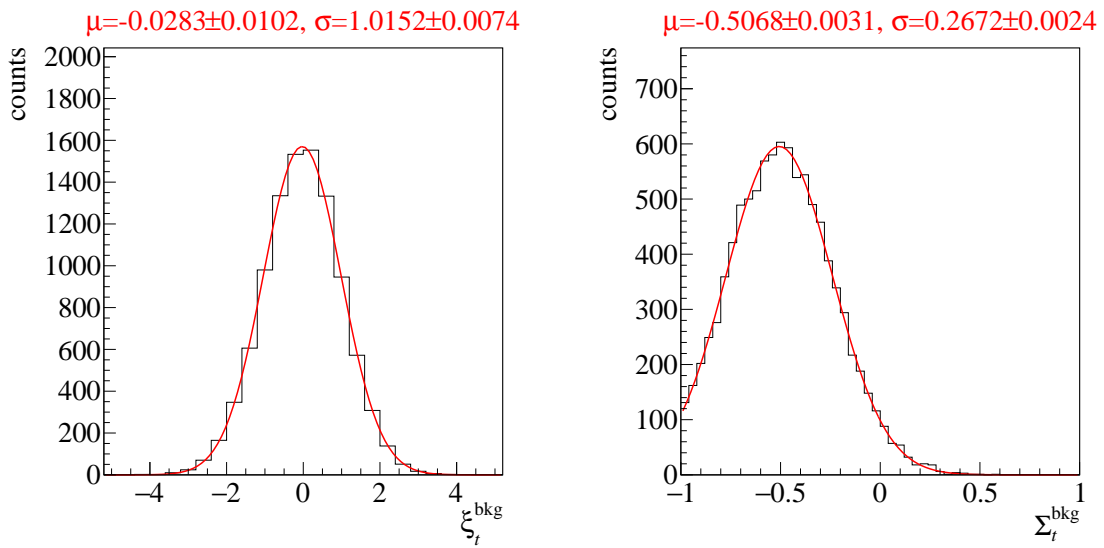


Figure 4.17: Normalized residuals (left) and unaltered distribution (right) of all 10000 fits for the background beam asymmetry Σ_t^{bkg} . GAUSSIAN fits are performed with results given on top of each plot.

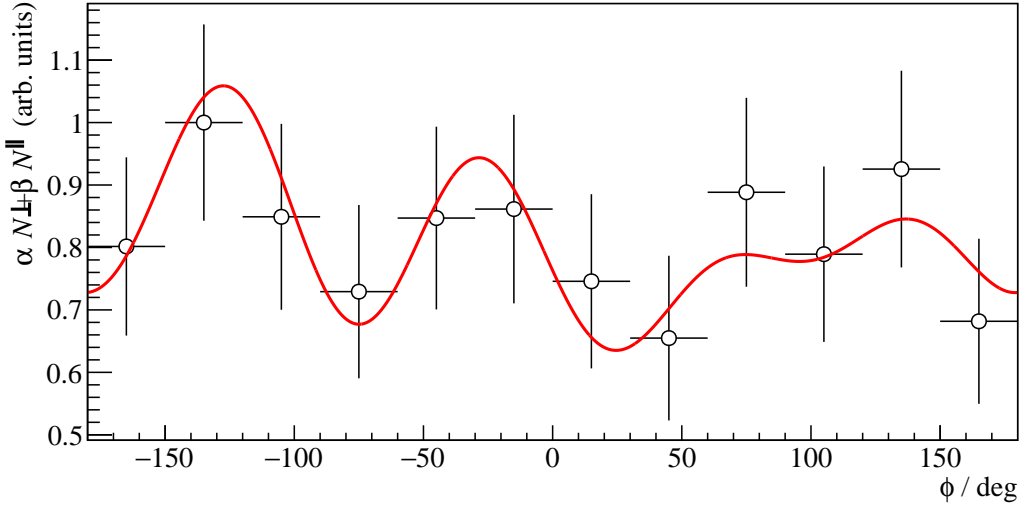


Figure 4.18: Fitted efficiency function (red line) applied to the polarization weighted sum of event yields (data points) for one toy Monte Carlo bin. 12 bins in ϕ are built for demonstration.

Unbinned BAYESIAN fit

When performing a BAYESIAN fit a systematic shift like Equation (4.42) as result of background contributions is not easily applicable. The posterior distributions may be shifted by a constant value but including statistical errors of the background beam asymmetry is not possible. To circumvent this, the background beam asymmetry can be included inherently in the likelihood function that is part of the model being fitted. In practice, δ and Σ_2 have to be part of the data that is fed into the probabilistic model. In general though Σ_2 will have a statistical error, which can be included in the fashion of modeling *missing data* [Sta22]. Doing so, the value for Σ_2 is regarded as an estimate for the true, unknown (or missing) value Σ_2^{true} . The statistical error τ of Σ_2 specifies the measurement model assuming GAUSSIAN errors

$$\Sigma_2^{\text{true}} \sim \mathcal{N}(\Sigma_2, \tau). \quad (4.44)$$

With this Σ_2^{true} is added as an additional fit parameter to the probabilistic model, so that the likelihood is modified as

$$\begin{aligned} \ln \mathcal{L} = & \sum_{i=1}^n \ln p_{\text{prompt}} \left(\phi_i, p_{\gamma,i} \mid (1 - \delta) \cdot \Sigma_1 + \delta \cdot \Sigma_2^{\text{true}}, a, b, \Sigma_t^{\text{bkg}}, a^{\text{bkg}}, b^{\text{bkg}} \right) \\ & + \sum_{j=1}^m \ln p_{\text{sideband}} \left(\phi_j, p_{\gamma,j} \mid \Sigma_t^{\text{bkg}}, a^{\text{bkg}}, b^{\text{bkg}} \right). \end{aligned} \quad (4.45)$$

For a complete inference Σ_2^{bkg} also needs to be assigned a prior, which is chosen to be uniform to keep the number of fit parameters minimal.

In total, 1000 bins in accordance with Table 4.2 are fitted with the adapted model that includes a background asymmetry Σ_2 with statistical error τ which are used to estimate the additional fit parameter Σ_2^{true} . For the sake of the toy Monte Carlo experiments the measurement error is arbitrarily chosen to be $\tau = 0.05$.

Figure 4.19 shows the combined posteriors for the fit parameters Σ_1 and Σ_t^{bkg} of the event based BAYESIAN fit for all generated toy Monte Carlo bins. The posteriors are added up since the truncation of the posteriors biases the results when combining them in a pooled likelihood model or normalized residuals Ξ . Although previous experiments already proved sensible error estimation, i.e. distribution widths, when using the unbinned BAYESIAN fit, this is further confirmed by removing the truncation and repeating the investigation of posteriors. This is discussed in appendix C. The input parameters are very well reproduced within the statistical error, which is given by the standard deviation of the GAUSSIAN. The posterior distribution of Σ_1 is wider than the posterior of the background beam asymmetry Σ_t^{bkg} because an additional measurement of Σ_2 with measurement error τ is used to estimate Σ_1 . This is in complete analogy to shifting the point estimates Σ^{meas} to their true values Σ^{true} , as described previously, which will also result in larger statistical error bars according to GAUSSIAN error propagation. Since the signal beam asymmetry Σ_1 was recognized correctly by the fit it is evident that

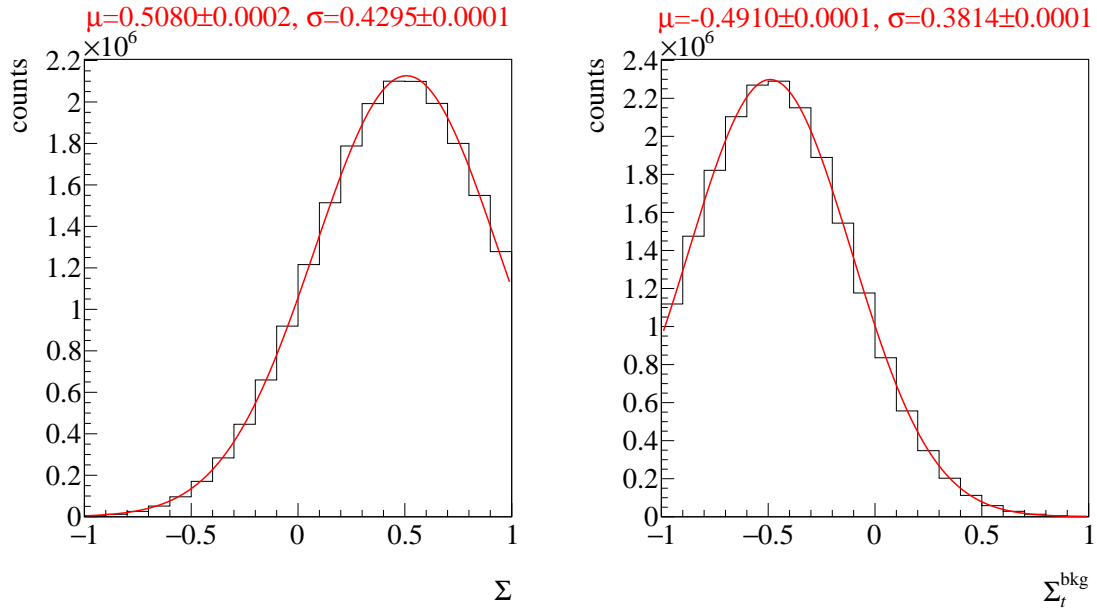


Figure 4.19: Combined (added) posteriors of all 1000 fits. Left: Signal beam asymmetry Σ_1 Right: Background beam asymmetry Σ_t^{bkg} . A GAUSSIAN fit is performed with results given on top.

the combined posterior distributions for Σ_2 are in full agreement with the expectations, see figure 4.20. Mean μ and standard deviation σ are reproduced exactly as they were modeled as a GAUSSIAN fit to the combined posteriors reveals.

It remains to investigate the properties of the employed MARKOV chains. First of all one observes that the accuracy of results, i.e. the relative MCSE, suffers from the available statistics which are significantly smaller in comparison with the previously investigated case for the $p\eta \rightarrow \gamma\gamma$ final state. Only 97% of all unbinned fits fulfill the self set criterion of $\sigma_{\text{MCSE}}/\text{median}(p(\Sigma|y)) \leq 0.05$ whereas

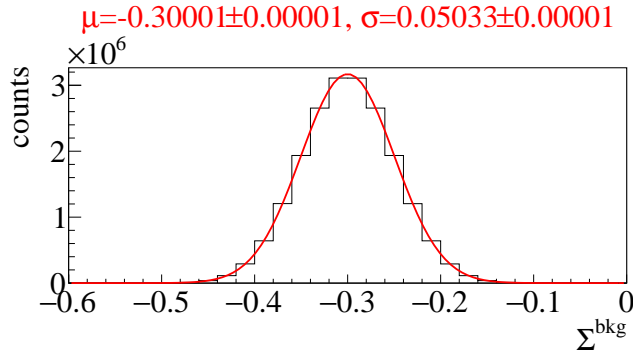


Figure 4.20: Combined (added) posteriors of all fits for the fit parameter Σ_2^{true} . A GAUSSIAN fit is performed which reproduces exactly the values that were used for the simulations.

for the toy Monte Carlo experiments in the previous section 4.2 this was the case for *all* unbinned fits. This observation however is not resembling a failing fit but rather the possibility for the data to mimic beam asymmetries close to zero because of the fewer available data points. In these cases the relative MCSE exceeds the threshold as has also been observed before. Convergence and full exploration of the available parameter space on the other hand is guaranteed for all fits because all \widehat{R} values for all parameters and fits are within the demanded thresholds.

Lastly, consistency of the fit results with the data that is fitted can be checked as before by a posterior predictive check of the detector coefficients a, b plugged into the efficiency function $\epsilon(\phi) = \frac{1}{c} \cdot (\alpha \tilde{N}^{\parallel} + \beta \tilde{N}^{\perp})$ as can be seen in Figure 4.22. Each draw $a^{(s)}, b^{(s)}, s = 1, \dots, 20000$ is plotted as an opaque blue line. The mean over the posterior draws is indicated by the dashed line and follows the polarization weighted sum of event yields which is shown as data points. The mean agrees within statistical error bars at each point indicating finally a successful fit in every respect.

It has been demonstrated that the chosen BAYESIAN model can describe data generated with two beam asymmetries very well. Note that expanding the existing model from before requires little effort since *Stan* [Sta22] allows modular implementations; only the new parameter Σ_2^{true} and the new data points (Σ_2, τ, δ) have to be added to give correctly centered posteriors that are not anymore systematically shifted.

4.3.2 Application of event based fit to data

Now both previously discussed methods are applied to the selected data.

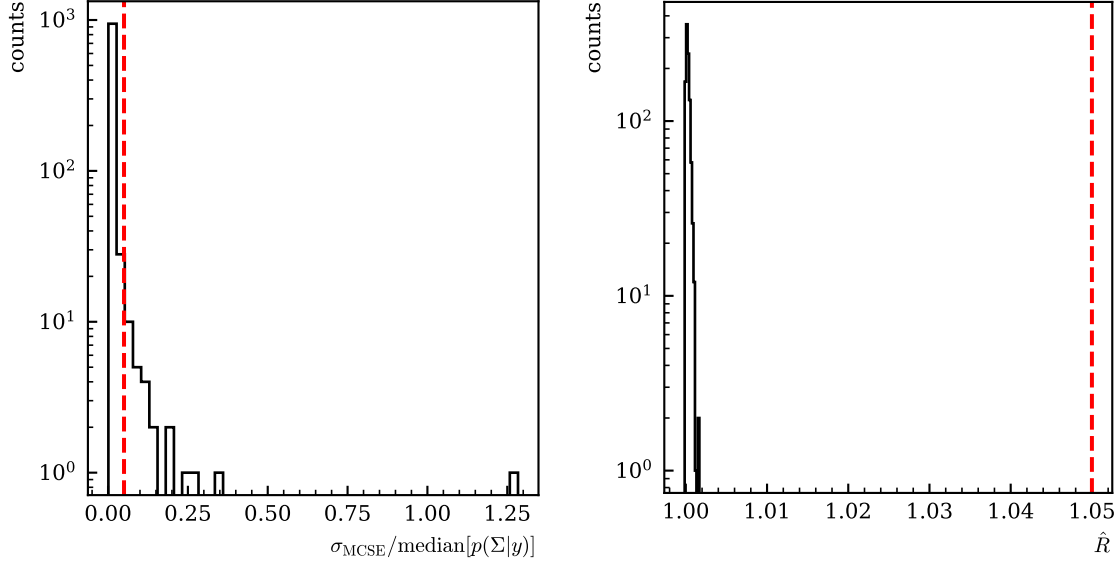


Figure 4.21: MCMC diagnostics for the event based BAYESIAN fit. Left: MCSE, Right: \hat{R} -value. The critical values not to be exceeded are marked by the dashed lines.

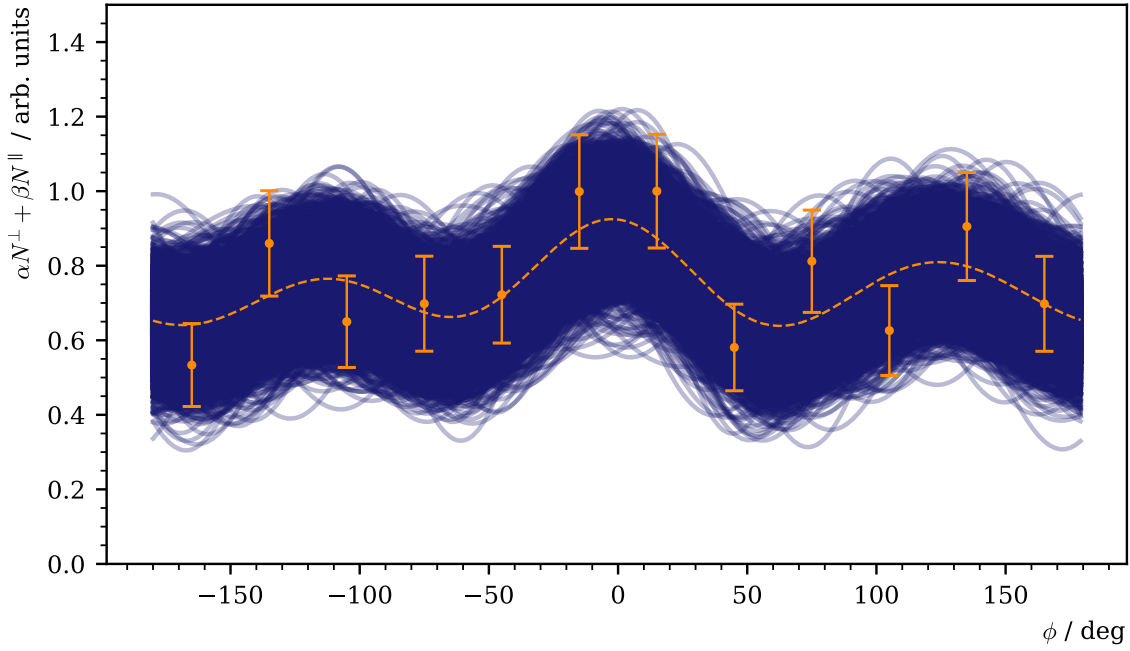


Figure 4.22: Posterior predictive checks of one toy Monte Carlo bin using the draws from the marginal posteriors of the detector coefficients a, b (opaque blue lines). The mean values are marked by the dashed line and follow the distribution of the data points which are the polarization weighted sum of event yields, using 12 ϕ bins.

CHAPTER 5

Summary and outlook

APPENDIX A

Additional calculations

A.1 Statistical error for the asymmetry $A(\phi)$

Let $\tilde{N}_i^{\parallel/\perp}$ be the normalized event yields at bin ϕ_i . As mentioned in section 4.1, the asymmetry A_i at bin i is then given by

$$A_i = \frac{\tilde{N}_i^\perp - \tilde{N}_i^\parallel}{p_\gamma^\parallel \tilde{N}_i^\perp + p_\gamma^\perp \tilde{N}_i^\parallel} = \Sigma \cos(2(\alpha^\parallel - \phi_i)), \quad (\text{A.1})$$

where the event yields are normalized over all M ϕ -bins

$$\tilde{N}_i^{\parallel/\perp} = \frac{N_i^{\parallel/\perp}}{\sum_{j=1}^M N_j^{\parallel/\perp}}.$$

To estimate statistical errors according to **GAUSSIAN** error propagation, the partial derivatives with respect to $\tilde{N}_i^{\parallel/\perp}$ have to be built:

$$(\Delta A_i)^2 = \left(\frac{\partial A_i}{\partial \tilde{N}_i^\parallel} \Delta \tilde{N}_i^\parallel \right)^2 + \left(\frac{\partial A_i}{\partial \tilde{N}_i^\perp} \Delta \tilde{N}_i^\perp \right)^2, \quad (\text{A.2})$$

Appendix A Additional calculations

where

$$\left(\frac{\partial A_i}{\partial \tilde{N}_i^{\parallel/\perp}} \right)^2 = \left[\frac{\tilde{N}_i^{\perp/\parallel} (p_\gamma^\perp + p_\gamma^\parallel)}{\left(p_\gamma^\parallel \tilde{N}_i^\perp + p_\gamma^\perp \tilde{N}_i^\parallel \right)^2} \right]^2, \quad (\text{A.3})$$

$$\text{and with } \tilde{N}_i^{\perp/\parallel} = \tilde{N}_i \quad (\text{A.4})$$

$$(\Delta \tilde{N}_i)^2 = \left[\frac{\partial}{\partial N_i} \left(\frac{N_i}{\sum_j N_j} \right) \cdot \Delta N_i \right]^2 + \sum_{j \neq i} \left[\frac{\partial}{\partial N_j} \left(\frac{N_i}{\sum_j N_j} \right) \cdot \Delta N_j \right]^2 \quad (\text{A.5})$$

$$= \left[\frac{\sum_{j \neq i} N_j}{\left(\sum_j N_j \right)^2} \cdot \Delta N_i \right]^2 + \sum_{j \neq i} \left[-1 \cdot \frac{N_i}{\left(\sum_j N_j \right)^2} \cdot \Delta N_j \right]^2 \quad (\text{A.6})$$

$$= \frac{1}{\left(\sum_j N_j \right)^4} \cdot \left[\left(\sum_{j \neq i} N_j \cdot \Delta N_i \right)^2 + \sum_{j \neq i} (N_i \cdot \Delta N_j)^2 \right]. \quad (\text{A.7})$$

One can then further use that $(\Delta N_i)^2 \approx N_i$. This holds only approximately, since the histograms are filled N times with weights w_n (see chapter 3.2), but since the weights are either $w = 1$ or $w \ll 1$

$$\Delta N_i = \sqrt{\sum_{n=1}^N w^2} \approx \sqrt{N_i}. \quad (\text{A.8})$$

APPENDIX B

Discussion of binned fits

APPENDIX C

Investigation of truncated posteriors

Bibliography

- [Zyl+20] P. Zyla et al., *Review of Particle Physics*, PTEP **2020** (2020) 083C01 (cit. on pp. 2, 3, 11, 15, 17).
- [LMP01] U. Löring, B. Metsch and H. Petry, *The light-baryon spectrum in a relativistic quark model with instanton-induced quark forces*, The European Physical Journal A **10** (2001) 395, ISSN: 1434-601X, URL: <http://dx.doi.org/10.1007/s100500170105> (cit. on pp. 2, 3).
- [KS03] B. Krusche and S. Schadmand, *Study of nonstrange baryon resonances with meson photoproduction*, Prog. Part. Nucl. Phys. **51** (2003) 399, arXiv: nucl-ex/0306023 (cit. on pp. 3, 4).
- [Afz19] F. N. Afzal, *Measurement of the beam and helicity asymmetries in the reactions $\gamma p \rightarrow p\pi^0$ and $\gamma p \rightarrow p\eta$* , PhD thesis: Rheinische Friedrich-Wilhelms-Universität Bonn, 2019, URL: <https://hdl.handle.net/20.500.11811/8064> (cit. on pp. 4, 11, 20, 21, 34, 35, 39, 40, 44, 45, 48, 51, 54, 56).
- [DT92] D. Drechsel and L. Tiator, *Threshold pion photoproduction on nucleons*, J. Phys. G **18** (1992) 449 (cit. on p. 4).
- [Bar+18] M. Bartelmann et al., *Theoretische Physik 3 — Quantenmechanik*, 2018, ISBN: 978-3-662-56071-6 (cit. on p. 4).
- [Bar89] R. J. Barlow, *Statistics, A Guide to the Use of Statistical Methods in the Physical Sciences*, Wiley, 1989 (cit. on pp. 5, 42).
- [Wal] D. Walther, *Crystal Barrel, A 4π photon spectrometer*, URL: <https://www.cb.uni-bonn.de> (visited on 27/09/2021) (cit. on pp. 7–10).
- [Urb17] M. Urban, *Design eines neuen Lichtpulsersystems sowie Aufbau und Inbetriebnahme der neuen APD Auslese für das Crystal-Barrel-Kalorimeter*, PhD thesis: Rheinische Friedrich-Wilhelms-Universität Bonn, 2017 (cit. on p. 9).
- [Afz22] F. Afzal, *Private communication*, 2022 (cit. on p. 11).
- [Ike+00] H. Ikeda et al., *A detailed test of the CsI(Tl) calorimeter for BELLE with photon beams of energy between 20-MeV and 5.4-GeV*, Nucl. Instrum. Meth. A **441** (2000) 401 (cit. on pp. 17, 19).
- [Har17] J. Hartmann, *Measurement of Double Polarization Observables in the Reactions $\gamma p \rightarrow p\pi^0$ and $\gamma p \rightarrow p\eta$ with the Crystal Barrel/TAPS Experiment at ELSA*, Rheinische Friedrich-Wilhelms-Universität Bonn, 2017, URL: <https://hdl.handle.net/20.500.11811/7258> (cit. on pp. 21, 37, 39).

Bibliography

- [Cre+09] V. Crede et al., *Photoproduction of eta and eta-prime mesons off protons*, Phys. Rev. C **80** (2009) 055202, arXiv: 0909.1248 [nucl-ex] (cit. on p. 23).
- [Die+20] M. Dieterle et al., *Helicity-Dependent Cross Sections for the Photoproduction of π^0 Pairs from Nucleons*, Physical Review Letters **125** (2020), URL: <https://doi.org/10.1103/PhysRevLett.125.062001> (cit. on p. 23).
- [Käs+18] A. Käser et al., *First measurement of helicity-dependent cross sections in $\pi^0\eta$ photoproduction from quasi-free nucleons*, Physics Letters B **786** (2018) 305, URL: <https://doi.org/10.1016/j.physletb.2018.10.006> (cit. on p. 23).
- [San+11] A. M. Sandorfi, S. Hoblit, H. Kamano and T.-S. H. Lee, *Determining pseudoscalar meson photoproduction amplitudes from complete experiments*, Journal of Physics G: Nuclear and Particle Physics **38** (2011) 053001, issn: 1361-6471, URL: <http://dx.doi.org/10.1088/0954-3899/38/5/053001> (cit. on p. 33).
- [Afz+20] F. Afzal et al., *Observation of the $p\eta'$ Cusp in the New Precise Beam Asymmetry Σ Data for $\gamma p \rightarrow p\eta'$* , Phys. Rev. Lett. **125** (15 2020) 152002, URL: <https://link.aps.org/doi/10.1103/PhysRevLett.125.152002> (cit. on p. 34).
- [RP22] G. van Rossum and the Python development team, *The Python Language Reference, Release 3.10.5*, 2022, URL: <https://docs.python.org/3.10/reference/index.html> (cit. on pp. 36, 53).
- [Vir+20] P. Virtanen et al., *SciPy 1.0: Fundamental Algorithms for Scientific Computing in Python*, Nature Methods **17** (2020) 261 (cit. on p. 36).
- [BR97] R. Brun and F. Rademakers, *ROOT — An object oriented data analysis framework*, Nucl. Instrum. Meth. A **389** (1997) 81, issn: 0168-9002, URL: <https://www.sciencedirect.com/science/article/pii/S016890029700048X> (cit. on pp. 36, 39, 40, 53).
- [sci] scipy, *scipy.optimize.curve_fit, Function Documentation*, URL: https://docs.scipy.org/doc/scipy/reference/generated/scipy.optimize.curve_fit.html (visited on 28/06/2022) (cit. on p. 36).
- [ROOa] ROOT, *TH1 Class reference*, URL: <https://root.cern.ch/doc/master/classTH1.html#a63eb028df86bc86c8e20c989eb23fb2a> (visited on 28/06/2022) (cit. on p. 36).
- [Sta22] Stan development team, *Stan Modeling Language Users Guide and Reference Manual*, vol. 2.29, 2022, URL: <https://mc-stan.org> (cit. on pp. 36, 39, 53, 58, 60).
- [HG14] M. D. Hoffman and A. Gelman, *The No-U-Turn Sampler: Adaptively Setting Path Lengths in Hamiltonian Monte Carlo*, Journal of Machine Learning Research **15** (2014) 1593, URL: <http://jmlr.org/papers/v15/hoffman14a.html> (cit. on pp. 36, 39).

-
- [ROOb] ROOT, *TTree Class reference*, URL: <https://root.cern.ch/doc/master/classTTree.html#a3e6bf252ab8653b47cc9116950f3ee7b> (visited on 28/06/2022) (cit. on p. 39).
 - [JR75] F. James and M. Roos, *Minuit - a system for function minimization and analysis of the parameter errors and correlations*, Computer Physics Communications **10** (1975) 343, ISSN: 0010-4655, URL: <https://www.sciencedirect.com/science/article/pii/0010465575900399> (cit. on p. 39).
 - [ROOc] ROOT, *TF1 Class reference*, URL: <https://root.cern.ch/doc/master/classTF1.html#a410b0219e18e80d3e305b4d97374c077> (visited on 28/06/2022) (cit. on p. 40).
 - [Veh+19] A. Vehtari, A. Gelman, D. Simpson, B. Carpenter and P.-C. Bürkner, *Rank-normalization, folding, and localization: An improved \hat{R} for assessing convergence of MCMC*, arXiv e-prints, arXiv:1903.08008 (2019) arXiv:1903.08008, arXiv: 1903.08008 [stat.CO] (cit. on p. 43).

List of Figures

1.1	Running coupling of QCD. The colored data points represent different methods to obtain a value for α_s . For more details it may be referred to [Zyl+20].	2
1.2	Calculated nucleon (isospin $I = 1/2$) resonances compared to measurements. Left in each column are the calculations [LMP01], the middle shows the measurements and PDG rating [Zyl+20]	3
1.3	FEYNMAN diagram for the s-channel photoproduction of pseudoscalar mesons, adapted from [Afz19]	4
2.1	[Wal]	7
2.2	[Wal]	8
2.3	[Wal]	8
2.4	D. WALTHER in [Urb17]	9
2.5	[Wal]	9
2.6	[Wal]	10
3.1	Distribution of event classes in $\eta' \rightarrow \gamma\gamma$ production	12
3.2	Time information of all final state particles and the beam photon for 3PED η' production	13
3.3	Reaction time t_r for 3PED η' production	14
3.4	Coplanarity of the $p\eta'$ final state with all other cuts applied for the energy bin $1\,500\,\text{MeV} \leq E_\gamma < 1\,600\,\text{MeV}$. The vertical dashed lines show the cut ranges obtained from a gaussian fit to the data (open circles). The solid black histograms represent fitted MC data of $\eta' \rightarrow \gamma\gamma$	18
3.5	Polar angle difference of the $p\eta'$ final state with all other cuts applied for the energy bin $1\,500\,\text{MeV} \leq E_\gamma < 1\,600\,\text{MeV}$. The vertical dashed lines show the cut ranges obtained from a gaussian fit to the data (open circles). The solid black histograms represent fitted MC data of $\eta' \rightarrow \gamma\gamma$	18
3.6	Missing mass of the $p\eta'$ final state with all other cuts applied for the energy bin $1\,500\,\text{MeV} \leq E_\gamma < 1\,600\,\text{MeV}$. The vertical dashed lines show the cut ranges obtained from a fit to data (open circles) employing a Novosibirsk function. The solid colored histograms represent fitted MC data from relevant photoproduction reactions: in black η' , in green π^0 , in red η , in blue ω , in yellow $2\pi^0$, magenta $\pi^0\eta$. The turquoise histogram is the sum of all MC histograms.	19

3.7	Invariant mass of the $p\eta'$ final state with all other cuts applied for all energy and angular bins. The open circles represent the measured data, the solid colored histograms fitted MC data from relevant photoproduction reactions: in black η' , in green π^0 , in red η , in blue ω , in yellow $2\pi^0$ and in magenta $\pi^0\eta$. The turquoise histogram is the sum of all MC histograms.	20
3.8	Invariant mass of the $p\eta'$ final state with all other cuts applied for the energy bin $1500 \text{ MeV} \leq E_\gamma < 1600 \text{ MeV}$. The vertical dashed lines show the cut ranges obtained from a gaussian fit to the η' MC data (solid black histogram). The open circles represent the measured data, the solid colored histograms fitted MC data from relevant photoproduction reactions: in black η' , in green π^0 , in red η , in blue ω , in yellow $2\pi^0$ and in magenta $\pi^0\eta$. The turquoise histogram is the sum of all MC histograms.	21
3.9	Acceptance for the reaction $\gamma p \rightarrow p\eta'$ after all cuts that have been discussed so far for 2.5PED and 3PED events	22
3.10	Fraction of background events in the analyzed beam energy and angular bins.	23
3.11	Acceptance for possible background contributions	24
3.12	Generated energies of the two lowest energy photons in $2\pi^0$ photoproduction MC data. The threshold of 20 MeV is marked by a vertical red line. Lowest energy photon is shown on the top, second lowest energy photon is shown on the bottom.	25
3.13	Generated energies of the two lowest energy photons in $2\pi^0$ and $\pi^0\eta$ photoproduction MC data. The threshold of 20 MeV is marked by a vertical red line. Lowest energy photon is shown on the top, second lowest energy photon is shown on the bottom.	26
3.14	Polar angle difference $\Delta\theta$ between the photon with second highest energy and second lowest energy of the $\pi^0\eta$ final state.	26
3.15	Illustration of the misidentification process during reconstruction	27
3.16	Generated CMS angle $\cos\theta_{\text{gen.}}$ vs. reconstructed CMS angle $\cos\theta_{\text{rec.}}$ for both background reactions. The slope $\cos\theta_{\text{gen.}} = \cos\theta_{\text{rec.}}$ is indicated by the solid line.	28
3.17	Detector hits of the recoil proton, as obtained from MC data for the production of η' , $2\pi^0$ and $\pi^0\eta$. CB: Crystal Barrel, FW: forward detector, MT: MiniTAPS	30
3.18	Difference in measured and calculated beam energy. Data points are shown as open circles, MC data as solid histograms: in black η' , in green π^0 , in red η , in blue ω , in yellow $2\pi^0$ and in magenta $\pi^0\eta$. The turquoise histogram is the sum of all MC histograms.	31
3.19	Invariant mass spectrum passing different stages in the event selection process. In the end clear peaks for all possibly produced mesons are visible. The vertical lines indicate the mean cut ranges over all energy and angle bins.	32
4.1	Left: Definition of angles α, ϕ, φ . Right: Photon momentum \vec{k} and polarization $\vec{\epsilon}$ define the beam polarization plane while the reaction plane is defined by the recoil proton p and produced meson M	33

4.2 Posterior predictive checks $p(A_{\text{rep}} A)$ from a BAYESIAN fit to the event yield asymmetries for six toy Monte Carlo bins are shown as distributions. The data points in the upper plot are the asymmetry $A(\phi)$, which was additionally fitted using a χ^2 fit (solid line). The goodness of fit is shown using p -values, which give the fraction $T(A_{\text{rep}} > A)$ of replicated samples greater than the original measured value, with propagated statistical error bars on the bottom of each plot. The expected mean value of $T(A_{\text{rep}} > A) = 0.5$ is indicated by the dashed line.	41
4.3 p values of all toy Monte Carlo bins. They are centered around their mean at 0.5, which is indicated by the dashed line, and show no bias towards higher or lower values, thus confirming an adequate fit.	42
4.4 Left: Combined posterior distributions of all 10000 fits normalized by their respective standard deviation. Right: Unaltered combined posterior distributions of all 10000 fits. A GAUSSIAN fit was performed to determine mean μ and standard deviation σ of the distributions with results given on top.	43
4.5 Left: relative error $\frac{\sigma_{\text{MCSE}}}{\text{median}[p(\Sigma y)]}$ Right: \widehat{R} associated with the fit parameter Σ . Both are shown for all 10000 fits. The critical values that should not be exceeded are marked by dashed lines.	44
4.6 Combined posteriors for the beam asymmetries Σ and Σ^{bkg} from all 1000 event based fits. Left: Residuals Ξ Right: Unnormalized posterior distributions. A GAUSSIAN fit is performed on the distributions with results for mean μ and standard deviation σ on top.	46
4.7 Combined posterior probabilities using the <i>pooled likelihood</i> approach. Left: Signal beam asymmetry, Right: background beam asymmetry. Mean and standard deviation as obtained from a Gaussian fit are shown on top	47
4.8 Left: relative error $\frac{\sigma_{\text{MCSE}}}{\text{median}[p(\Sigma y)]}$ Right: \widehat{R} associated with the fit parameter Σ . Both are shown for all 1000 fits. The critical values that should not be exceeded are marked by dashed lines.	47
4.9 Posterior predictive check using the draws of the detector coefficients a and b . Points with error bars are the polarization weighted sum of event yields. The dashed line is the mean of the predictive values while the solid opaque lines are representative of one simulation draw $a^{(s)}, b^{(s)}$.	48
4.10 Posterior predictive checks $p(A_{\text{rep}} A)$ from a BAYESIAN fit to the event yield asymmetries for all angular bins of the energy bin $1\,250\,\text{MeV} \leq E_\gamma < 1\,310\,\text{MeV}$. The data points in the upper plot are the asymmetry $A(\phi)$, which was additionally fitted using a χ^2 fit (solid line). The goodness of fit is shown using p -values, which give the fraction $T(A_{\text{rep}} > A)$ of replicated samples greater than the original measured value, with propagated statistical error bars on the bottom of each plot. The expected mean value of $T(A_{\text{rep}} > A) = 0.5$ is indicated by the dashed line.	49
4.11 p values generated using all fits. They are centered around their mean at 0.5, which is indicated by the dashed line, and show no bias towards higher or lower values, thus confirming an adequate fit.	50
4.12 Left: relative error $\frac{\sigma_{\text{MCSE}}}{\text{median}[p(\Sigma y)]}$ Right: \widehat{R} associated with the fit parameter Σ . Both are shown for all $11 \cdot 12$ binned fits to the asymmetry $A(\phi)$. The critical values that should not be exceeded are marked by dashed lines.	51

4.13 Left: relative error $\frac{\sigma_{\text{MCSE}}}{\text{median}[p(\Sigma y)]}$ Right: \widehat{R} associated with the fit parameter Σ . Both are shown for all $11 \cdot 12$ unbinned fits. The critical values that should not be exceeded are marked by dashed lines.	52
4.14 Posterior predictive check using the draws of the detector coefficients a and b for the kinematic bin $1250 \text{ MeV} \leq E_\gamma < 1310 \text{ MeV}, 0 \leq \cos \theta < 0.17$. Points with error bars are the polarization weighted sum of event yields. The dashed line is the mean of the predictive values while the solid opaque lines are representative of one simulation draw $a^{(s)}, b^{(s)}$	52
4.15 Final results for the beam asymmetry Σ in η photoproduction off the proton for all kinematic bins obtained with BAYESIAN methods. They are compared with the results of a least squares fit and an unbinned fit as given in reference [Afz19]. All results agree within statistical error bars or within the widths of marginal posterior distributions.	54
4.16 Normalized residuals (left) and unaltered distribution (right) of all 10000 fits for the beam asymmetry $\Sigma = (1 - \delta) \cdot \Sigma_1 + \delta \cdot \Sigma_2$. GAUSSIAN fits are performed with results given on top of each plot.	57
4.17 Normalized residuals (left) and unaltered distribution (right) of all 10000 fits for the background beam asymmetry Σ_t^{bkg} . GAUSSIAN fits are performed with results given on top of each plot.	57
4.18 Fitted efficiency function (red line) applied to the polarization weighted sum of event yields (data points) for one toy Monte Carlo bin. 12 bins in ϕ are built for demonstration.	58
4.19 Combined (added) posteriors of all 1000 fits. Left: Signal beam asymmetry Σ_1 Right: Background beam asymmetry Σ_t^{bkg} . A GAUSSIAN fit is performed with results given on top.	59
4.20 Combined (added) posteriors of all fits for the fit parameter Σ_2^{true} . A GAUSSIAN fit is performed which reproduces exactly the values that were used for the simulations.	60
4.21 MCMC diagnostics for the event based BAYESIAN fit. Left: MCSE, Right: \widehat{R} -value. The critical values not to be exceeded are marked by the dashed lines.	61
4.22 Posterior predictive checks of one toy Monte Carlo bin using the draws from the marginal posteriors of the detector coefficients a, b (opaque blue lines). The mean values are marked by the dashed line and follow the distribution of the data points which are the polarization weighted sum of event yields, using 12 ϕ bins.	61

List of Tables

1.1	Summary of the particles of the SM	1
1.2	Allowed quantum numbers for the intermediate resonance state N^*/Δ^*	4
3.1	The five most probable decay modes of the η' meson. The most probable further decay with according branching ratio is shown in brackets.[Zyl+20]	11
3.2	Examined MC reactions that were used in sum for the fit	16
3.3	Fit functions and cut ranges for each variable	17
3.4	Total cross sections σ in the energy range 1 500 to 1 800 MeV, branching ratios (BR) to $n\gamma$ final states and maximum acceptance \hat{A} for signal and possible background contributions	23
3.5	Relative loss in signal and background events if a cut on ΔE is applied.	29
4.1	Summary of the complete setting of all toy Monte Carlo experiments for the event based fit. Values and table layout adapted from [Afz19].	45
4.2	Summary of the complete setting of all toy Monte Carlo experiments for the event based fit. Table layout adapted from [Afz19].	56